UNIVERSITY OF TURKU

Multidimensional Embedded MEMS Motion Detectors for Wearable Mechanocardiography and 4D Medical Imaging

Mojtaba Jafari Tadi

UNIVERSITY OF TURKU

MULTIDIMENSIONAL EMBEDDED MEMS MOTION DETECTORS FOR WEARABLE MECHANOCARDIOGRAPHY AND 4D MEDICAL IMAGING

Mojtaba Jafari Tadi

University of Turku

Faculty of Medicine
Medical Physics and Engineering
Doctoral Program in Clinical Research
Turku PET Center, Turku University Hospital
Faculty of Science and Engineering
Department of Future Technologies

Supervised by

Professor Mika Teräs, Ph.D.
Department of Medical Physics
Department of Biomedicine
University of Turku
Turku University Hospital
Turku, Finland

Dr. Eero Lehtonen, D.Sc. (Tech)
Department of Future Technologies
University of Turku
Turku, Finland

Associate Professor. Antti Saraste, MD, Ph.D.
Department of Cardiology,
Turku Heart Center
Turku PET Center
University of Turku
Turku University Hospital
Turku, Finland

Reviewed by

Professor Omer T. Inan
School of Electrical and Computer
Engineering
Georgia Institute of Technology
Atlanta, United States of America

Professor Simo Särkkä
Department of Electrical Engineering
and Automation
Aalto University
Helsinki, Finland

Opponent

Professor Kouhyar Tavakolian
Department of Electrical Engineering
University of North Dakota
North Dakota, United States of America

Abstract

Mojtaba Jafari Tadi, M.Sc.
University of Turku, Faculty of Medicine, Medical Physics and Engineering,
Doctoral Program in Clinical Research,
Turku PET Center, Turku University Hospital,
Faculty of Science and Engineering, Department of Future Technologies

Multidimensional Embedded MEMS Motion Detectors for Wearable Mechanocardiography and 4D Medical Imaging

Background: Cardiovascular diseases are the number one cause of death. Of these deaths, almost 80% are due to coronary artery disease (CAD) and cerebrovascular disease. Multidimensional microelectromechanical systems (MEMS) sensors allow measuring the mechanical movement of the heart muscle offering an entirely new and innovative solution to evaluate cardiac rhythm and function. Recent advances in miniaturized motion sensors present an exciting opportunity to study novel device-driven and functional motion detection systems in the areas of both cardiac monitoring and biomedical imaging, for example, in computed tomography (CT) and positron emission tomography (PET).

Methods: This Ph.D. work describes a new cardiac motion detection paradigm and measurement technology based on multimodal measuring tools — by tracking the heart's kinetic activity using micro-sized MEMS sensors — and novel computational approaches — by deploying signal processing and machine learning techniques — for detecting cardiac pathological disorders. In particular, this study focuses on the capability of joint gyrocardiography (GCG) and seismocardiography (SCG) techniques that constitute the mechanocardiography (MCG) concept representing the mechanical characteristics of the cardiac precordial surface vibrations.

Results: Experimental analyses showed that integrating multisource sensory data resulted in precise estimation of heart rate with an accuracy of 99% (healthy, n=29), detection of heart arrhythmia (n=435) with an accuracy of 95-97%, ischemic disease indication with approximately 75% accuracy (n=22), as well as significantly improved quality of four-dimensional (4D) cardiac PET images by eliminating motion related inaccuracies using MEMS dual gating approach. Tissue Doppler imaging (TDI) analysis of GCG (healthy, n=9) showed promising results for measuring the cardiac timing intervals and myocardial deformation changes.

Conclusion: The findings of this study demonstrate clinical potential of MEMS motion sensors in cardiology that may facilitate in time diagnosis of cardiac abnormalities. Multidimensional MCG can effectively contribute to detecting atrial fibrillation (AFib), myocardial infarction (MI), and CAD. Additionally, MEMS motion sensing improves the reliability and quality of cardiac PET imaging.

Keywords: MEMS motion sensors, seismocardiography, gyrocardiography, dual cardiac and respiratory gating, cardiovascular disease, cardiac PET/CT imaging

Tiivistelmä

Mojtaba Jafari Tadi
Turun yliopisto, lääketieteellinen tiedekunta, Lääketieteellisen fysiikan ja tekniikan oppiaine,
Kliinisen tutkimuksen tohtoriohjelma,
PET-keskus, Turun yliopistollinen keskussairaala,
Luonnontieteiden ja tekniikan tiedekunta, Tulevaisuuden teknologioiden laitos

Moniulotteisten sulautettujen MEMS-liiketunnistimien käyttö sydänkardiografiassa sekä lääketieteellisessä 4D-kuvantamisessa

Tausta: Sydän- ja verisuonitaudit ovat yleisin kuolinsyy. Näistä kuolemantapauksista lähes 80% johtuu sepelvaltimotaudista (CAD) ja aivoverenkierron häiriöistä. Moniulotteiset mikroelektromekaaniset järjestelmät (MEMS) mahdollistavat sydänlihaksen mekaanisen liikkeen mittaamisen, mikä puolestaan tarjoaa täysin uudenlaisen ja innovatiivisen ratkaisun sydämen rytmin ja toiminnan arvioimiseksi. Viimeaikaiset teknologiset edistysaskeleet mahdollistavat uusien pienikokoisten liiketunnistusjärjestelmien käyttämisen sydämen toiminnan tutkimuksessa sekä lääketieteellisen kuvantamisen, kuten esimerkiksi tietokonetomografian (CT) ja positroniemissiotomografian (PET), tarkkuuden parantamisessa.

Menetelmät: Tämä väitöskirjatyö esittelee uuden sydämen kineettisen toiminnan mittaustekniikan, joka pohjautuu MEMS-anturien käyttöön. Uudet laskennalliset lähestymistavat, jotka perustuvat signaalinkäsittelyyn ja koneoppimiseen, mahdollistavat sydämen patologisten häiriöiden havaitsemisen MEMS-antureista saatavista signaaleista. Tässä tutkimuksessa keskitytään erityisesti mekanokardiografiaan (MCG), joihin kuuluvat gyrokardiografia (GCG) ja seismokardiografia (SCG). Näiden tekniikoiden avulla voidaan mitata kardiorespiratorisen järjestelmän mekaanisia ominaisuuksia.

Tulokset: Kokeelliset analyysit osoittivat, että integroimalla usean sensorin dataa voidaan mitata syketiheyttä 99% (terveillä n=29) tarkkuudella, havaita sydämen rytmihäiriöt (n=435) 95-97%, tarkkuudella, sekä havaita iskeeminen sairaus noin 75% tarkkuudella (n=22). Lisäksi MEMS-kaksoistahdistuksen avulla voidaan parantaa sydämen 4D PET-kuvan laatua, kun liikeepätarkkuudet voidaan eliminoida paremmin. Doppler-kuvantamisessa (TDI, Tissue Doppler Imaging) GCG-analyysi (terveillä, n=9) osoitti lupaavia tuloksia sydänsykkeen ajoituksen ja intervallien sekä sydänlihasmuutosten mittaamisessa.

Päätelmä: Tämän tutkimuksen tulokset osoittavat, että kardiologisilla MEMS-liikeantureilla on kliinistä potentiaalia sydämen toiminnallisten poikkeavuuksien diagnostisoinnissa. Moniuloitteinen MCG voi edistää eteisvärinän (AFib), sydäninfarktin (MI) ja CAD:n havaitsemista. Lisäksi MEMS-liiketunnistus parantaa sydämen PET-kuvantamisen luotettavuutta ja laatua.

Avainsanat: MEMS liiketunnistimet, seismokardiografia, gyrokardiografia, sydän- ja hengitystahdistus, sydän- ja verisuonitauti, kaksoistahdistus, sydämen PET / CT-kuvantaminen

Contents

Symbols and Abbreviations

$1D$	One Dimensional
$2D$	Two Dimensional
$3D$	Three Dimensional
$4D$	Four Dimensional
AC	Attenuation Correction
ACS	Acute Coronary Syndrome
$AFib$	Atrial Fibrillation
AMI	Acute Myocardial Infarction
AS	Atrial Systole
AVC	Aortic Valve Closure
AVO	Aortic Valve Opening
CAD	Coronary Artery Disease
CC	Cardiac Cycle
cps	Crystal Probe Sensitivity
CT	Computed Tomography
CTI	Cardiac Time Intervals
CVD	Cardiovascular Disease
DoF	Degree of Freedom
DPS	Degree Per Second
DTI	Diastolic Time Intervals
ECG	Electrocardiography
ED	End Diastole
ES	End Systole
F_s	Sampling Frequency
FDG	F-fluorodeoxyglucose
FoV	Field of View
g	Gravity
GCG	Gyrocardiography
HF	Heart Failure
HRV	Heart Rate Variability

Hz	Hertz
IM	Isovolumetric Movements
IMU	Inertial Measurement Unit
$IVCT$	Isovolumetric Contraction Time
$IVRT$	Isovolumetric Relaxation Time
keV	Kilo Electron-Volts
LV	Left Ventricle
$LVET$	Left Ventricular Ejection Time
MBq	Mega Becquerel
MCG	Mechanocardiography
$MEMS$	Microelectromechanical Systems
MRI	Magnetic Resonance Imaging
MVC	Mitral Valve Closure
MVO	Mitrol Valve Opening
$NSTEMI$	Non-ST Elevated Myocardial Infarction
PCG	Phonocardiography
PEP	Pre Ejection Period
PET	Positron Emission Tomography
PMT	Photomultiplier Tube
PPG	Photoplethysmography
PW	Pulse Wave
RE	Systolic Rapid Ejection
RF	Early Rapid Filling
RMS	Root Mean Square
RPM	Real-time Position Management
RV	Right Ventricle
$S1$	First Heart Sound
$S2$	Second Heart Sound
SCG	Seismocardiography
SR	Strain Rate
$STEMI$	ST Elevated Myocardial Infarction
STI	Systolic Time Intervals
SUV	Standardized Uptake Value
TDI	Tissue Doppler Imaging

List of Original Publications

Study I | **Jafari Tadi M**, Koivisto T, Pänkäälä M, Paasio A. "Accelerometer Based Method for Extracting Respiratory and Cardiac Gating Information for Dual Gating during Nuclear Medicine Imaging". Journal of Biomedical Imaging. 2014; 690124:1-12.

Study II | **Jafari Tadi M**, Lehtonen E, Hurnanen T, Koskinen J, Eriksson J, Pänkäälä M, Teräs M, Koivisto T. "A Real-time Approach for Heart Rate Monitoring using a Hilbert Transform in Seismocardiograms". Physiological Measurements. IOP publications. 2016 July; 37(11): 1885-1909.

Study III | **Jafari Tadi M**, Lehtonen E, Saraste A, Tuominen J, Koskinen J, Teräs M, Airaksinen J, Pänkäälä M, Koivisto T. "Gyrocardiography: A New Non-invasive Monitoring Method for the Assessment of Cardiac Mechanics and the Estimation of Hemodynamic Variables". Scientific Reports, Nature. 2017 July 28; 7(1): 6823.

Study IV | **Jafari Tadi M**, Teuho J, Lehtonen E, Saraste A, Pänkäälä M, Koivisto T, Teräs M. "A Novel Dual Gating Approach Using Joint Inertial Sensors: Implications for Cardiac PET Imaging". Physics in Medicine & Biology. IOP publications. 2017 Oct 4; 62(20): 8080-8101.

Study V | **Jafari Tadi M**, Mehrang S, Kaisti M, Lahdenoja O, Hurnanen T, Jaakkola J, Jaakkola S, Vasankari T, Lehtonen E, Airaksinen J, Koivisto T, and Pänkäälä M. "Comprehensive Analysis of Cardiogenic Vibrations for Automated Detection of Atrial Fibrillation Using Smartphone Mechanocardiograms". IEEE Sensors Journal. 2018.

Study VI | Iftikhar Z, Lahdenoja O, **Jafari Tadi M**, Hurnanen T, Vasankari T, Kiviniemi T, Airaksinen J, Koivisto T, Pänkäälä M. "Multiclass Classifier based Cardiovascular Condition Detection Using Smartphone-Mechanocardiography". Scientific Reports, Nature. 2018 Jun 19; 8(1): 9344.

Study VII | Kaisti M, **Jafari Tadi M**, Lahdenoja O, Hurnanen T, Saraste A, Pänkäälä M, Koivisto T. "Stand-alone Heartbeat Detection in Multidimensional Mechanocardiograms". IEEE Sensors Journal. 2018 .

This thesis book is based on the original journal publications which will be referred to by Roman numerals. All original articles included in this thesis have been reproduced with permissions of the copyright holders.

Part I

Research Summary

Chapter 1

INTRODUCTION

Heart diseases are the number one cause of death in the world [1]. Cardiovascular disease (CVD) — also known as heart disease — includes disorders of the heart and vessels and is considered as the leading cause of health problems claiming nearly one third of total deaths globally [2]. The prevalence of heart diseases is predicted to continuously rise by 2030 as a result of the rapidly growing population of the elderly people and progressive outbreak of cardiovascular risk factors. This is associated with a further mismatch between the number of patients and physicians, as well as increasing healthcare costs [3].

The ability to detect cardiac disorders via low-cost and smart personalized monitoring systems can potentially improve global healthcare services. Via widespread pre-emptive screening, the focus will shift from expensive and heavy treatment solutions towards low-cost and easy prevention of diseases, enabling good health during a greater portion of one's lifetime. This will lead to enhanced quality of life, and savings for the healthcare sector and the entire global society. With the new detection and prevention strategies, nations worldwide could save lives, but also lessen the burden these diseases cause to the economy, personal lives and prosperity. In addition to preventing monitoring, new monitoring strategies may contribute to the improved care of existing diseased patients.

To this end, it is imperative to seek for innovative solutions and new technologies to improve the quality of patient care and minimize the cost of care through early detection/intervention and more effective disease or patient management [4]. Accordingly, a huge amount of investments has been made on research and development of new scalable wearable/mobile devices as they can leverage the recent advances in miniaturized sensor developments, embedded or pervasive health computing, and physiological data analytics. Therefore, by developing easy-to-access non-invasive and/or unobtrusive sensing systems for continuous recording of underlying physiological data, it may be feasible to diagnose at-risk patients for early intervention.

1.1 Emerging Technologies for Health Monitoring

Emerging interdisciplinary technologies represent a great opportunity for the realization of a preventive, predictive, pre-emptive, personalized, and wellness- and patient-centered healthcare system [4]. Smart wearables are today considered as the potential solution for tackling societal challenges caused by health problems. Market prospects for wearables are increasing as wearables shipments are expected to increase to $150 billion by 2026 from the estimated level of $30 billion in 2016. Moreover, wearable technology is expected to reduce healthcare costs by as much as 16% over the next 5 years, and remote patient monitoring technologies could save healthcare systems up to $200 billion over the next 25 years. Mobile health, multidisciplinary health data processing algorithms, smart fusion of multimodal systems, and the existence of hugely accessible health databases will enhance the healthcare systems and biomedical industries [5, 6].

The state-of-art wearable electronics such as headbands, motion tracking badges, optical sensors, smart watches, glasses, jewellery, virtual reality headsets, and many other measuring modalities incorpo-

rated into small-sized patches/clothes can potentially yield to an improved health monitoring. In simple terms, new smart wearables offer unprecedented opportunities for unobtrusive sensing through continuous monitoring of physical activities, physiological and biochemical parameters, and vital signs.

Current wearable/mobile health monitoring solutions mainly deal with data acquisition, transmission, processing, storage, and the use of health informatics for the early detection and prediction of many diseases. New embedded sensing machinery provides a real possibility for long-term ubiquitous and intermittent sensing/diagnosing. For example, state-of-art wearable/implantable instruments comprising microelectromechanical (MEMS) pressure, accelerometer, gyroscope, and microphone sensors have pivotal clinical implications for long-term ubiquitous, unobtrusive, and intermittent sensing [7–11]. Such sensory solutions can be considered as a natural extension of the current sophisticated bio-electrical techniques (e.g. electrocardiogram) enabling a comprehensive point-of-care diagnosis. Figure 1.1 shows an envisioned portfolio of personalized medical and fitness monitoring integrated into smart devices.

With the advancing technology in the field, the new generation wearable/implantable devices will move towards unobtrusive sensing methods such as smart textile technology, flexible stretchable printable electronics, and sensor fusion coupled with advances in the Internet of Things (IoT), machine learning, and deep learning to the implementation of high-performance and pervasive health informatics. New solutions benefit from energy harvesting, efficient power consumption, and very low-power high-performance.
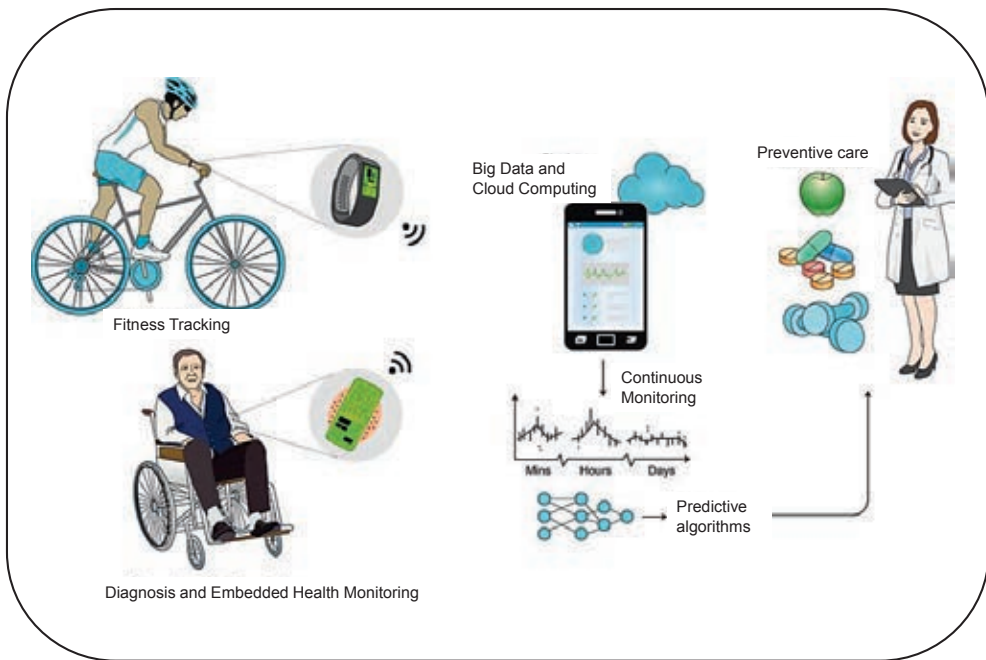
Figure 1.1: Future portfolio of consumer wearable medical devices for personalized health monitoring (From: [12] © Reprint with permission).

1.2 Problem Statement and Motivation of the Thesis

Today, cardiovascular system is monitored by several ways, of which the most common is electrocardiography (ECG), that records the electrical activity of the heart and is considered the gold standard of non-invasive diagnosis of arrhythmias and ischemic heart diseases. ECG monitoring can be performed

remotely using either a portable device or a wearable/implantable monitor. Traditional ECG recording requires optimal positioning and attachment of electrodes (including hair removal and skin degreasing) for the clean recording of electrical signals [13]. To detect acute or chronic cardiac disorders such as heart arrhythmia and ischemic heart diseases, long-term measurements and real-time alerts are necessary to enable reliable and accurate diagnostics, as symptoms sensed by the patient may be non-specific and occur entirely unnoticed [14, 15]. New clinically approved devices such as handheld and wireless single-lead ECG monitors — for example, AliveCore Kardia, ECG Check, Medtronic loop recorders, and Zio Patch — constitute a paradigm shift in modern cardiac health monitoring, while there are still open issues regarding cost-effectiveness, the patient populations that could benefit from them, and data transmission to be interpreted and acted upon by the clinical professionals [16]. Apart from that, most of the current existing mobile/wearable devices lack the capabilities to comprehensively measure physiological parameters essential for the assessment of respiratory and cardiac function. For instance, although ECG yields valuable information on instantaneous electrical states of the heart, it gives no information concerning the instantaneous mechanical status of the heart. The reason is that the complex movements of the heart muscle do not necessarily correlate with the electrical performance of the heart and therefore ECG fails to show the mechanical characteristics of the cardiac function [13].

In the past decades, more attention has focused on the resurgence of non-invasive and unobtrusive vital sign monitoring via sophisticated methods for measuring and interpreting mechanocardiograms (MCG), specifically ballistocardiography (BCG) and seismocardiography (SCG) signals. A considerable amount of work has been carried out on non-invasive and contactless sensors, mainly BCG and SCG, for cardiomechanical monitoring and measuring important parameters of the heart motion [17]. The existing research has addressed that the SCG/BCG signals have a great potential in allowing a proactive cardiac performance evaluation that might be useful in the detection of heart arrhythmia, coronary diseases and ischemia, cardiac dyssynchrony, valvular disorders, and heart failure [17]. However, there are still undiscovered potentials, for example, via new modalities for hybrid study of the heart motions, for detecting aforementioned diseases, as well as unsolved challenges, for example, analytical and technical complications, that obstacle robust and reliable continuous monitoring of cardiovascular status via MCG technology.

The main motivation of this Ph.D. work was to explore new strategies to comprehensively assess cardiovascular mechanical function via low-cost and efficient wearable/mobile MEMS sensors. The focus of research in DIGITAL HEALTH TECHNOLOGY LAB was to not only explore existing modalities, but also investigate new solutions for measuring physiological parameters for cardiorespiratory monitoring, as well as cardiac imaging. In this context, we sought to develop biosignal processing algorithms for estimating cardiac motions solely based on multidimensional MEMS motion detectors. We consider multidisciplinary approaches including signal processing and artificial intelligent techniques to characterize and analyse physiological signals derived from wearable and mobile sensors. These approaches are extensively used in the detection of cardiovascular disorders such as atrial fibrillation (AFib), acute myocardial infarction (AMI), and coronary artery diseases (CAD), as well as prediction of cardiorespiratory quiescence phases for motion correction in medical imaging. In a nutshell, this thesis shows the capability of a new multidimensional MCG for measuring the heart's mechanical performance in a three dimensional space. The presented dual-sensory solution is fully non-invasive as tri-axial MEMS gyroscope and accelerometers are attached either directly via wearable patches or indirectly via already available built-in inertial measurement units (IMU) of the smart phones to the chest of the individuals. Multidimensional sensing allows obtaining 6 degree-of-freedom (DoF) motion signals originated from the precordial vibrations coupled with the myocardial wall movements. This work closely focuses on algorithm development for processing and analysis of the currently available MCG signals to overcome existing challenges. The ultimate goal of this study was to improve obtained parameters estimated by mechanical cardiovascular monitoring while introducing a new modality, so-called gyrocardiography, based on other characteristics of the heart motion.

1.3   Organization of the Dissertation

Chapter 2 covers cardiovascular function including anatomy and physiology of the heart and describes major characteristics of three most important cardiac diseases considered in this work. Chapter 3 describes various modalities used in this work including different measurement techniques and physiological signals, cardiac imaging techniques and corresponding processing methods. Chapter 4 describes PET imaging and methodologies for motion correction. Chapter 5 specifies the aims of this Ph.D. work and Chapter 6 describes materials and methodologies used in this study including data acquisitions system developments, biosignal processing techniques, and machine learning frameworks. Chapter 7 presents major outcomes obtained in this work, and Chapter 8 discusses the potential applications of multidimensional cardiorespiratory motion processing systems for personal wearable/mobile heart monitoring and medical imaging. Finally, Chapter 9 concludes this Ph.D. work and addresses future direction of research in this field.

Chapter 2

Background Physiology and Underlying Cardiovascular Diseases

2.1 Cardiovascular System

2.1.1 Anatomy and Mechanical Physiology of the Heart

The human heart, located in the mediastinum, is a muscular organ that is responsible for blood circulation in the body. The heart muscle is comprised of four distinct chambers, namely two atria responsible for gathering blood and two ventricles for pumping blood throughout the body. The four chambers are divided into the left and right sides, each containing an atrium and a ventricle. In addition to these chambers, the heart includes two atrioventricular valves, the bicuspid or mitral valve and tricuspid valve, and two semilunar valves, aortic valve and pulmonary valve, in the left and right chambers. During single cardiac cycle, two major phases, that is, systole and diastole, occur allowing blood outflow and inflow to the vascular tree and ventricles, respectively. During the systole, left and right ventricles contract in parallel, atriaventricular valves close – preventing blood return from the ventricles – and the aortic valve opens to deliver the oxygenated blood cells through the aortic artery. Conversely, during the diastolic phase ventricles relax and atrioventricular valves open allowing blood inflow (passive filling) from atria to the ventricles. In simple terms, the right ventricle task is to deliver deoxygenated blood to the lungs while the left ventricle serves to pump oxygenated blood throughout the circulatory system [18]. Each contraction and relaxation sequence is associated with changes in pressures, volumes, and flows underlying mechanical aspects of cardiac performance.

2.1.2 Cardiac Wall Motion

The heart is an electromechanical pump and its continuous mechanical pumping action is essential for the adequate blood supply throughout the body. The ventricular pumping action occurs as a result of cyclical changes of the intraventricular chamber volume caused by periodic and the synchronized contraction and relaxation of the individual cardiac muscle cells within the ventricular wall. The myocardium wall, a highly complex muscular structure, is the thickest muscle of the heart that encompasses left and right chambers, and undergoes repeating changes in different dimensions and orientations. Coordinated contraction-relaxation cycles in the myocardium are formed by continuously varying orientations and vectors of force in three-dimensions (3D) across the chamber wall [19]. In cellular structure, the contraction of helically oriented muscle fibres of myocardium act as an integrated force causing a coordinated wringing motion to the myocardium within each cardiac cycle [20–22]. Wringing motion due to twisting rotation plays an important role in systolic and diastolic myocardial deformation [21].

The mechanical activity of the heart involves contraction of myocardial cells, closing and opening of heart valves, and flow of blood into and from the heart chambers. This activity is modulated by changes

in the contractility of the heart, the compliance of the chamber walls, arteries, and the developed pressure gradient. In other words, mechanical function of the myocardium is characterized by shortening and lengthening of myocardial fibers/papillary muscle resulting in increased chamber pressure and a decrease in chamber volume, which allows blood ejection into the vascular tree. A single steady-state cardiac cycle is one complete sequence of myocardial contraction and relaxation which leads to clockwise and counterclockwise rotation of the left ventricle (LV). This twisting and untwisting action is associated with the storage and release of potential forces, contributing to LV systolic contraction and diastolic relaxation [23]. The movement of LV is the major contributor in the long axis of the heart and is considered as an indicator of ventricular systolic and diastolic function or dysfunction [24, 25].

Over the past years, several sophisticated techniques have been presented to quantitatively investigate cardiac mechanical function using diverse techniques in both animals and humans. The primary approach to evaluate cardiac motion, or myocardial deformation, was carried out by attaching multiple implanted radiopaque markers to the body of heart and subsequently undergoing biplane cine angiography analysis in dogs [26]. Following that study, various other invasive and non-invasive approaches were carried out including optical devices [27, 28], tagging magnetic resonance imaging (tagged MRI) [29], Doppler tissue imaging (DTI) [30, 31], and speckle tracking imaging [32]. These methods have been introduced to thoroughly evaluate the dynamics of cardiac motion and myocardial tissue function. Currently, echocardiography (TDI), together with supplementary imaging techniques such as speckle tracking, is the most common and standard technique to study strain rate — a measure of tissue deformation rate, and its integral, strain yields the total deformation of the heart muscle. Strain rate and strain are respectively related to the shortening velocity and shortening fraction of the myocardial wall [33]. In a new-fashioned way, implantable inertial sensors were used to continuously track left ventricular function/myocardium deformation and assess cardiac rotation in animals [34–37]. Figure 2.1 shows cardiac wall motion analysis using implantable/ultrasonic/contactless techniques.

2.1.3   Cardiac Electromechanical Conduction

The electrical and mechanical activity of the heart can be determined by specific physiological operations by which the performance of the heart functionality is assessed. During a cardiac cycle, several major electromechanical activities occur in parallel that yield to certain important cardiac events.

The heart's conduction system controls the generation and propagation of electrical signals or action potential that cause the heart's muscles to contract and thereby pump blood through the whole body. Each beat begins in the right atrium with an action potential signal from sinoatrial (SA) node. This triggering or activation pulse from SA note depolarizes atrial myocardial cells which leads to contraction of atria. This atrial contraction or atrial systole, represented by P-wave in electrocardiograms, raise forces/pressure to push blood into the ventricles. This period of conduction follows atrial systole and proceeds to ventricular contraction or depolarization of ventricular cells (depicted by PR segment following the P wave). When the signal leaves the atria it enters the ventricles via the atrioventricular or AV node located in the interatrial septum. It enters the bundle of His and spreads through the bundle branches and the large diameter Purkinje fibers along the ventricular walls. As the signal spreads through the ventricles, the contractile fibers depolarize and contract very rapidly inducing ventricular systole (depicted as QRS complex in ECG signal) leading to the closure of mitral (MVC) and Tricuspid valves, contributing to the first cardiac sound or S1, followed by a rapid blood ejection through the aortic valve opening (AVO). As the signal passes out of the ventricles the ventricular walls start to relax and recover, a state described as ventricular diastole marked by dome-shaped T-wave on ECG (ventricular repolarization). On the ECG, the ST segment depicts the period when the ventricles are depolarized. This is followed by gradual closure of the aortic valve (AVC) and the opening of the mitral valve (MVO). The second heart sound, S2, happens at the closing time of aortic and pulmonary valves. Figure 2.2 represents electrophysiological events and coinciding mechanical activities.
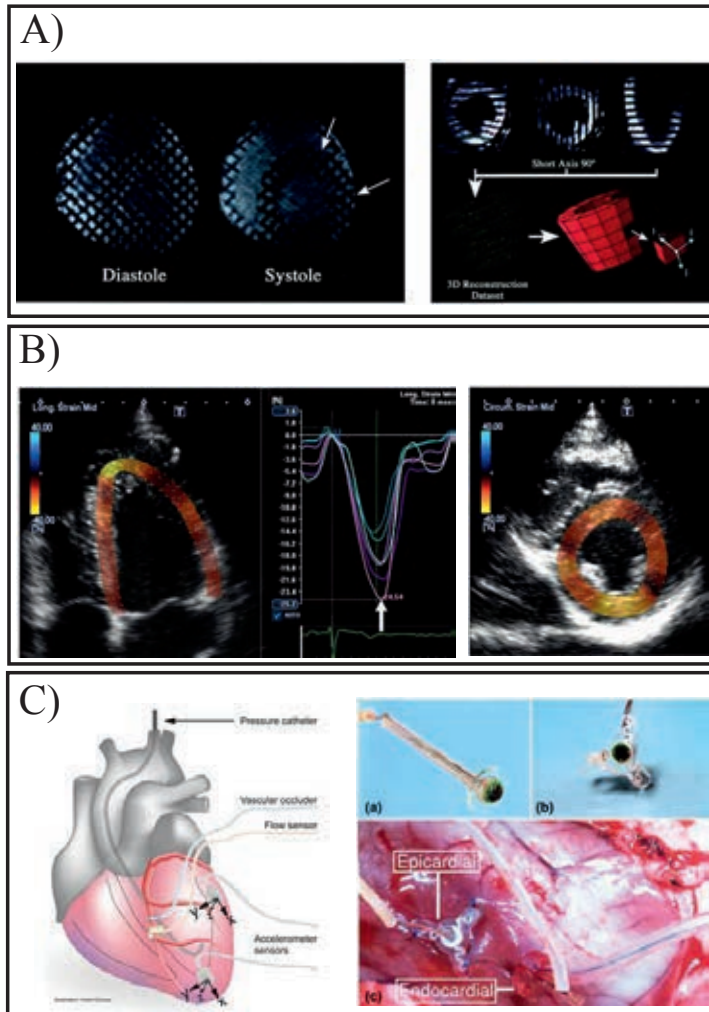
Figure 2.1: **Figure A** shows cardiac wall motion tracking using tagged MRI, **Figure B** indicates Speckle tracking for longitudinal wall motion tracing in echocardiography/TDI, **Figure C** shows implanted MEMS accelerometer and gyroscope sensors for measuring myocardial linear and angular movements (From: [37–40] © Reprint with permission).

2.1.4 Cardiac Time Intervals

Cardiac time intervals (CTI) refer to the timing period of physiological incidents that happen during a single stationary cardiac cycle. In practice, CTIs are divided into two sub-segments, systolic time intervals (STI) and diastolic time intervals (DTI). With distinguishing of the points where mitral and aortic valve opening and closure occure, several CTI can be defined as follows: The isovolumetric contraction time (IVCT) and the isovolumetric relaxation time (IVRT) which refer respectively to the time between the onset of MVC and AVO, and AVC and MVO moments. Additionally, three other systolic time intervals (STI) are defined as the total electromechanical systole (QS2), the left ventricular ejection time (LVET), and the pre-ejection period (PEP). In our considerations, the QS2 is measured from the ECG Q-wave to the moment of AVO, while the LVET is measured as the time interval between the moments of AVO and
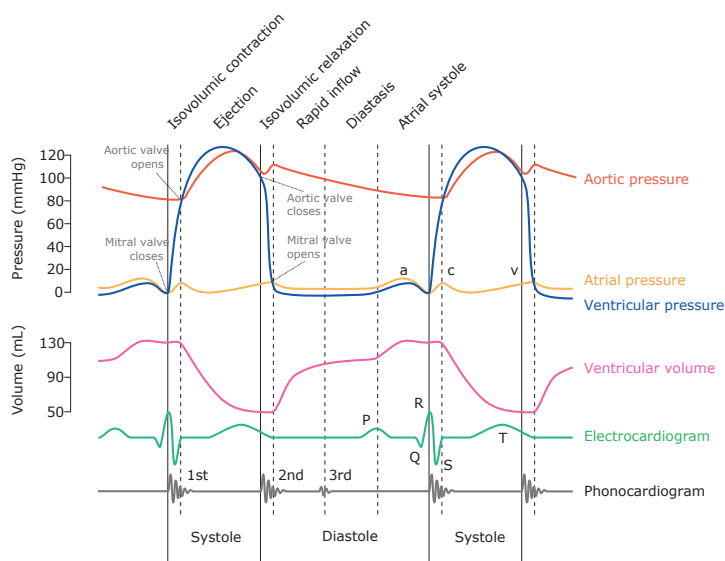
Figure 2.2: Wigger's diagram representing electromechanical cardiac events (From: [41] Reprint under creative commons license and attribution right ⓒⓘ).

AVC in the cardiac cycle. The PEP index is measured from the point of ECG Q-wave to the onset of the AVO. PEP and LVET are both important clinical parameters on myocardial contractility [42–44].

2.2   Cardiovascular Diseases

According to the American Heart Association's latest reports, heart diseases are the main cause of death globally. Cardiovascular diseases are the number one cause of death worldwide, leading to at least 17 million deaths in 2008, representing 30% of all global deaths. Of these deaths, almost 80% are due to coronary artery disease, or CAD, and cerebrovascular disease [2, 45]. In the contexts of this Ph.D. work, three major and high risk groups of CVDs were considered as described below.

2.2.1   Atherosclerotic Cardiovascular Disease

Cardiovascular disorders such as inflammatory diseases, ischemia, cardiac arrhythmia, and heart failure are the most known causes of death and their prevalence is increasing [2]. With atherosclerotic cardiovascular disease, the blood flow to the heart's muscle is decreased as the coronary arteries are gradually narrowed due to plaque formation within the walls. Atherosclerosis, or stiffening of arteries, is a progressive disease that refers to as obstruction and hardening of the arteries as a result of plaque accumulation surrounding the coronary arteries [46]. Sudden rupture of atherosclerotic plaques may lead to myocardial infarctions (MI) and ischemic strokes [47,48]. Current diagnostic techniques for coronary artery diseases are based on anatomical demonstration of vessel lumen narrowing, for example using X-ray contrast angiography that is insufficient for the quantitative assessment of plaque vulnerability to rupture [49]. Other approaches have been recently introduced to utilize smartphones/wearables for the detection of CVD conditions in a variety of ways [50–57].

The state-of-the-art for non-invasive detection of atherosclerotic plaque inflammation is PET imaging and 18F-fluorodeoxyglucose (FDG) as a radiotracer [49, 58–60]. Cardiac PET scan is new imaging modality suitable for metabolical assessment of coronary diseases and damaged heart muscles due to the
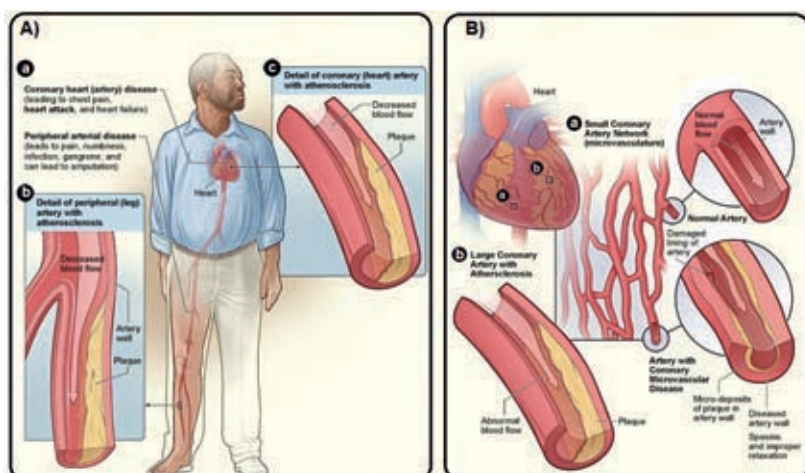
Figure 2.3: **Figure A** is an overview of coronary (heart) disease leading to chest pain, heart attack, and heart failure. **Figure B** is cross-section of the coronary artery network showing microvasculature with (abnormal) and without (normal) plaque formation in the arteries (From: National Heart, Lung, and Blood Institute (NHLBI) [65, 66] ©①).

heart attack [61]. Given the important role of inflammation in atherosclerosis, a cardiac PET scan can be used to measure the severity of inflammation in humans [59]. However, radiographic methods including PET suffer from major limitations such as tracer uptake quantification errors and image blurring due to respiration and cardiac motions [62, 63]. Motion artifacts reduce the image quality and quantitative accuracy of the PET imaging. To eliminate motion-related inaccuracies, cardiac and respiratory gating methods are the most common approaches applied in clinical PET imaging [64]. Figure 2.3 shows an overview of CAD progress due to atherosclerotic plaque formation in the walls of the coronary arteries.

2.2.2 Myocardial Infarction

Myocardial infarction (MI) is defined as myocyte/myocardial cell necrosis due to a prolonged episode of ischemia [67]. MI results from progress of CAD and refers to the severe reduction of blood flow and oxygen to the heart muscle and is generally categorized as non-ST-segment elevation myocardial infarction (NSTEMI), when a coronary artery is partially blocked so that myocardial cells demand more oxygen, or ST-segment elevation myocardial infarction (STEMI), when the artery is completely occluded and consequently myocardial cells die [47, 48]. Figure 2.4 shows death of the heart muscle area as a result of blocked arteries. Although, many invasive and non-invasive interventions such as ECG, stress testing, biochemical testing, and coronary imaging are often performed for ischemia diagnosis and assessment, still point-of-care assays for bedside detection of acute coronary syndromes (ACS) pose several limitations [68]. For example, resting 12-lead ECG is a standard clinical routine in cardiology which, although can determine the likelihood of the presence of acute coronary disease, it has relatively low sensitivity and specificity [69–71]. Ambulatory ECG monitoring may to some extent show signs of myocardial ischemia during normal daily activities but, in suspected cases, rarely provides important diagnostic evidence. In general, ECG fails in proper diagnostic of ischemic disease due to two reasons: i) it does not sufficiently contribute in representation and evaluation of cardiac wall motions or mechanical characteristics of the heart motion, and ii) normal examinations and observations do not exclude the possibility of ischemic disease or ACS [72]. Other tests such as echocardiography, chest X-ray, cardiac magnetic resonance imaging (MRI), biomarkers, and cardiac PET imaging may also be used, but are more expensive and require advanced logistics and sophisticated medical interpretations [68].
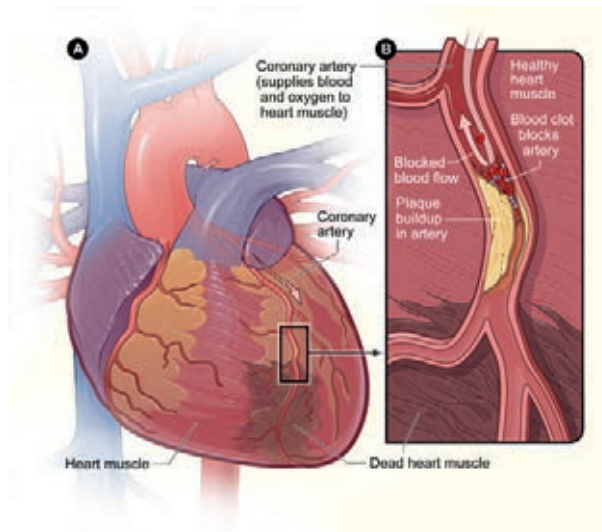
Figure 2.4: **Figure A** is an overview of the heart and coronary arteries showing damaged my-ocardial cells caused by acute infaction. **Figure B** is cross-section of the coronary artery with accumulated plaque and a resulting blood clot (From: NHLBI [73] ⓒⓘ).

The editorial letter by Pueyo (2013) [74] addressed numerous approaches to ischemic heart disease diagnosis by analysis of ECG depolarization. For example, Abboud et al. [75] proposed high-frequency (within a bandwidth of 150-250 Hz) analysis of electrocardiogram to assess electrophysiological changes due to CAD. As such, high-frequency changes in ECG QRS complex components, also known as Hyper-QRS, has been considered a sensitive indicator of acute coronary artery occlusion [76, 77]. Many other techniques have been also developed to detect acute ischemia using ECG [50, 51, 53, 54, 78]. ECG QT-wave dispersion was investigated as a measure of variability in ventricular recovery time and a possible measure for identifying patients at risk of arrhythmias and sudden death after infarction [78]. Mechanical dispersion, also known as strain rate variations, is measured by echocardiography and reflects the heterogeneity of myocardial systolic contraction. Myocardial mechanical dispersion is recently acknowledged as an indicator for susceptibility to arrhythmias in different heart disease groups such as heart failure and ischemia [79–81]. In recent years, machine learning algorithms based on wavelet transform feature engineering and pattern recognition have also been suggested to diagnose CAD conditions [57, 82].

2.2.3   Atrial Fibrillation

Atrial fibrillation (AFib) is a prevalent heart arrhythmia which is characterized by irregular atrial acti-vation (supraventricular tachyarrhythmia) leading to failure of atrial mechanical function [83]. During normal sinus rhythm of the heart, atrial activation is followed by fast contraction of the chambers at a similar pace [84]. Conversely, during AFib the atria contract randomly in an uncoordinated manner and vibrate approximately 400 to 600 times per minute resulting in mechanical failure in ventricular re-sponse. Prevalence of AFib increases with aging and approximately occurs in 3% of the adults aged 20 years or older [85]. AFib accounts for up to 40% of all strokes suffered in the world and in Europe alone for more than 200,000 deaths per year and costs up to 17.1 billion euros each year [86]. The condition becomes even more complicated from the age of 65 — approximately five percent of all 70 year-old persons and more than twenty percent of all persons 85 years or older suffer from AFib [84, 87].

Despite the clinical significance of this cardiac disorder, AFib detection remains still challenging, because it can appear infrequent and asymptomatic. Silent atrial AFib occurs in many situations before it manifests itself with hemodynamic impairment and thromboembolic events [88]. Undiagnosed AFib can

potentially lead to the formation of blood clot(s), heart failure (HF), acute strokes, and other heart-related complications [83]. Untreated AFib is associated with considerable morbidity, mortality, and financial costs [83]. Furthermore, although 30% of ischemic strokes occur without a discernible causative factor, recent studies have uncovered AFib in 16-30% of such patients during long-term rhythm monitoring [89, 90]. To effectively prevent cardioembolic strokes, AFib must be diagnosed as early as possible in its course. Figure 2.5 illustrates the process of ischemic stroke where a blood clot is formed in the heart (due to disorganized electrical activity resulting in quivering of atria) and arises blood flow blockage in the brain vessels affecting a portion of the brain.
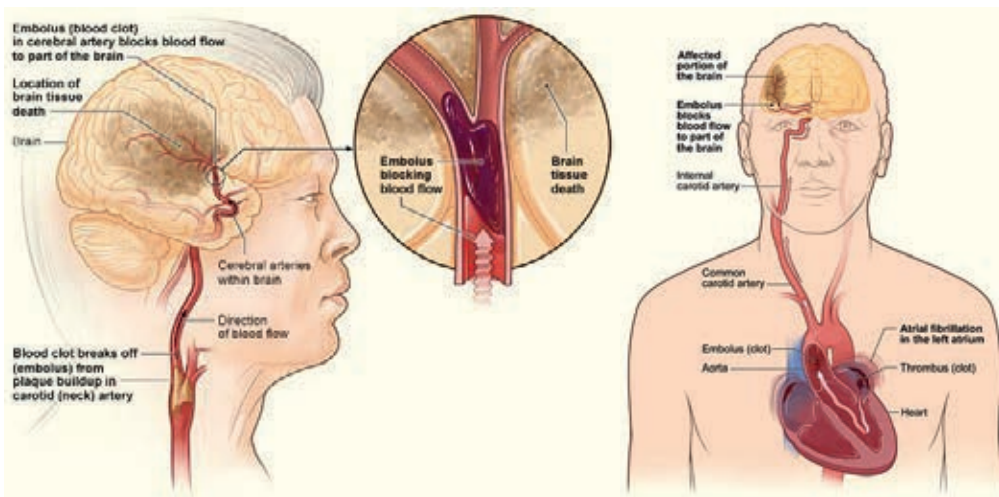

Figure 2.5: Disorganized electrical activity in the upper chambers of the heart causes fast quivering leading to clot formation and eventually brain stroke as the clot travels through carotid arteries (From: NHLBI [91] ©⒤).

Current standard diagnostic tools for arrhythmia detection include ECG [83, 92], echocardiography [93], and pulse oximeter/photoplethysmography (PPG) [94] which have been widely used in clinical environments. Handheld ECG devices, mobile phones [94], smart watches [95], and weighing scales [96] are recently exploited which aim to simplify and ameliorate personal medicine by enabling individuals to track their cardiovascular status themselves. AFib is, however, known to remain sporadic and indistinguishable in some of the medical examinations requiring long-term continuous monitoring for an in time precise diagnosis [92]. In order to detect symptoms appearing at periodic or random intervals, an effective strategy for longer-term monitoring, up to several days or weeks at a time, is needed [83, 92]. Despite vigorous research, efficient and cost-effective approaches to detect and screen for asymptomatic AFib are yet to be introduced.

Many new portable/wearable modalities such as AliveCore Kardia [97], Zenicor [98], Mydiagnostick [99], Zio Patch [100], Medtronic implantable loop recorders [89] and wearable SEEQ^{TM} mobile cardiac telemetry [16], iPhone optical sensor [94], Apple Watches [101], and Samsung Simband smartwatch [102] have been recently validated for AFib detection as they offer feasibility of long term monitoring. However, these methods pose two major limitations. Such modalities are first of all costly as currently available technologies for manufacturing miniaturized wearable/portable/implantable devices are expensive and the second problem is that they always require additional hardware which makes it impractical for large-scale screening purposes.

Mobile PPG-based recorders can be considered as a potentially suitable substitute to detect AFib owing to the fact that smartphone camera can simply trace changes in light absorption (by placing a fingertip on the camera), while no additional hardware is needed. However, PPG sensor measures only

Table 2.1: Summary of cross sectional observational studies for AFib detection using ECG and non-ECG devices.

Study	Device Name	Modality	Size	Sensitivity	Specificity
Nemati et al. [102]	Samsung Simband	8-channel PPG	46	97%	94%
Chan et al. [121]	Cardiio Rhythm	1-channel PPG	1013	92.9%	97.7%
Chan et al. [121]	AliveCor	1-channel ECG	1013	71.4%	97.7%
Lau et al. [122]	AliveCor	1-channel ECG	204	98%	97%
Lowers et al. [123]	AliveCor	1-channel ECG	1000	98.5%	91.4%
Desteghe et al. [124]	AliveCor	1-channel ECG	113	78.9%	97.9%
Barrett et al. [125]	Zenicor	1-channel ECG	3209	97.8%	88.2%
Chan et al. [126]	Microlife WatchBP Home	Pressure sensor	5969	80.6%	98.7%
Desteghe et al. [124]	MyDiagnostic	1-channel ECG	113	89.5%	95.7%
Brüser et al. [127]	EMFi ballistocardiogram	Force sensor	10	93.8%	98.2%
Jaakkola et al. [128]	Smartphone Mechanocardiograph	6-axis MEMS	300	95.3%	96%
Bumgarner et al. [128]	Kardia Band	1-channel ECG	100	93 %	84%

optical pulse-wave signal and considers inter-beat variability as the only basis for AFib detection. Smartphone PPG recorders sense the rate of blood flow over time and give no immediate feedback due to the heart's muscular activities as bio-potential/biomechanical generated signals provide [103–105]. Table 2.1 presents a brief review on new technologies developed in recent years for detection of AFib. A recent review on new and emerging approaches to detection of AFib is given in [106].

Current ECG-based methods for discriminating AFib can be determined by two principles: i) absence of P-wave or presence of fibrillatory F-waves in the TQ interval in ECG (atrial activity analysis) [107–109], and ii) heart rate variability due to inter-beat timing and amplitude variations of the QRS complexes (ventricular response as a result of the atrial activity) [110]. In addition to these criteria, and regardless of the measuring modality, further dominant characteristics of AFib signal pattern can be captured by, for example, Poincaré and Lorenz plot analysis [104, 111, 112], root mean square (RMS) and median absolute deviation (MAD) of successive intervals [105], distribution of the first and second difference of cardiac cycle intervals [113], spectral entropy [114], sample entropy [115], and Shannon entropy measures [105, 116–118]. A large number of studies, most of which based on the above techniques, has been conducted on automatic classification of AFib. Classic approaches include signal processing and knowledge-based techniques, while modern algorithms consider both signal processing and machine learning solutions to achieve reliable classification on AFib. Zabihi et al. (2017) recently presented a novel hybrid approach including multi-domain feature extraction, and a random forest classifier for AFib detection [119]. This method achieved the first place in PhysioNet/Computing in Cardiology (CinC) Challenge 2017 with an overall score of 82.6% on previously unseen testing data. Several other state-of-art ECG classification techniques based on extreme gradient boosting (XGBoost), convolutional (deep) neural networks(CNNs), and recurrent neural networks (RNNs) also revealed encouraging results in this challenge [120].

In this study the main focus was mobile phone detection of AFib as smartphone devices are fast becoming ubiquitous, and they offer unprecedented possibilities for various medical applications. MCG monitoring considers the translational and rotational precordial vibrations induced by myocardial wall movements. Almost all modern smartphones contain low-cost built-in accelerometers and gyroscopes enabling health data collection without any additional hardware. This study aims at indicating clinical potentials of mobile phone AFib and MI detection versus the gold standard of visual interpretation of continuous telemetry ECG recordings in hospitalized patients. The state-of-the-art algorithms for intensive processing of the heart's mechanical activity may open a new door on a more accurate diagnosis of CVDs.

Chapter 3

Background of Modalities Used in This Work

A brief overview on background of the modalities that are used in this work for the physiological signals recording as well as cardiac imaging techniques is provided in this chapter.

3.1   Microsensors

Developments in semiconductor fabrication processes have resulted in new and innovative solutions that allow designing sensitive microsensors with integrated signal processing circuits, wider exploitation of miniaturization technology, and lower manufacturing costs [129]. Microelectromechanical systems or MEMS include mechanical and electrical micro-sized components which can be fabricated using integrated circuit batch-processing techniques. MEMS devices have small size, low weight, low power consumption, high sensitivity, and high resolution [129]. New smart sensors including MEMS offer a great opportunity to combine sensing, signal processing and actuation on a micro-scale to be used in many fields of industry, control systems, and biomedical applications.

Current smart wearable technology constitutes miniaturized and multidimensional motion detectors for recording cardiovascular mechanical activity. User-friendly and cost-effective wearable MEMS sensors together with advanced signal processing and artificial intelligence may improve prediction and prevention of cardiovascular diseases through early stage detection and rapid determination of the characteristics of an acute cardiac event, for example, heart attack, with greater certainty.

Measuring cardiac muscle motion has been known since the 19th century as a technique for assessing the condition of the heart [17]. Six degrees of freedom (6DoF) cardiac motion sensing via miniature sensors refers to the motion of the heart in the three-dimensional space. The generic motion of the heart consists of the translation of the center of mass in three orthogonal directions and rotation about the center of mass around three orthogonal axes. Approximately 40% of the mechanical movement of a healthy heart is linear and 60% is rotational [131]. Figure 3.1 shows an experimental model of heart kinetics resulting from sequential twisting of the myocardial wall. As addressed by previous in vivo studies [34–37, 40], the translational quantities such as linear velocity and acceleration that describe linear motion of the heart can be measured by for example an accelerometer sensor, while the rotational quantities such as angular displacement, angular velocity, and angular acceleration may be measured by a gyroscope sensor. Therefore, in considerations of this Ph.D. work, these two sensors are used to non-invasively measure cardiac vibrations as the accelerometer sensor is sensitive to translational vibrations and the gyroscope sensor is sensitive to the rotational precordial movements. However, the engagement mechanism and the transfer function from the motion of the heart to the motion of the chest are still unclear, and should be investigated more thoroughly in the future. The general working principles of these two sensors are first described in the following and the new modalities used in cardiological discussions will be introduced afterwards.
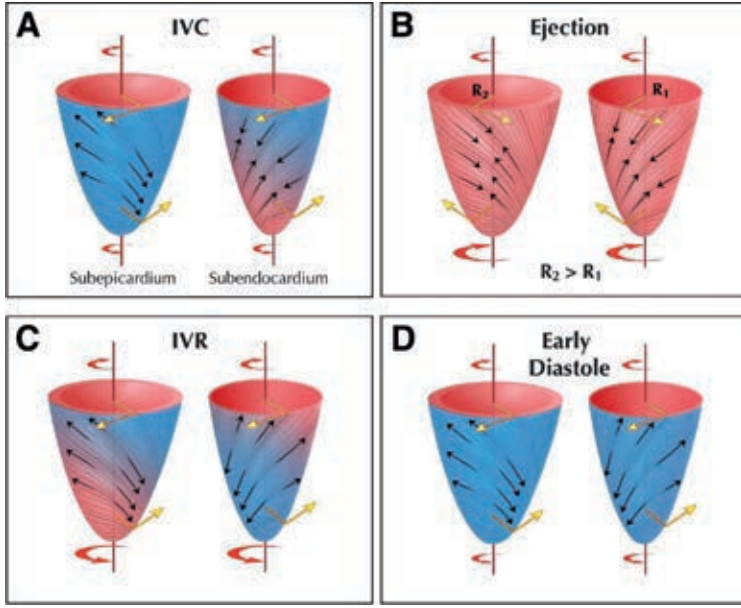
Figure 3.1: **Figure A** is a sequence of twist mechanics of the heart over clockwise and counterclockwise helical motions while electric and mechanical activation are initiated. **Figure B** shows shortening of the heart muscle during systolic activation. **Figure C** describes lengthening of the myocardial wall over untwisting in the beginning of diastole. **Figure D** shows minimum untwisting of the muscle as it is characterized by relaxation of both layers (From: [130] © Reprint with permission).

3.1.1 MEMS Accelerometers

The main components of a MEMS sensor are mechanical elements, sensing mechanism, and a microcontroller/processor. A tri-axial capacitive linear accelerometer with an integrated interface chip includes programmable components such as integrated circuits (ICs) and sensor on one single chip [129,132,133]. General MEMS accelerometer sensors are sensitive to the displacement of a spring mass with a position-measuring interface circuit. The displacement of spring mass is then converted into an electrical signal and subsequently digitalized through an analog-to-digital converter (ADC) for further processing.

Any rigid object follows Newton's second law of motion as:

$$a = \frac{F}{m},$$
(3.1)

where a is acceleration (m/s^2), F is force (N), and m is mass (kilograms). In principle, accelerometers measure a force applied to the micro-fabricated components, for example, moving springs, by detecting the displacement of a moving mass relative to the fixed electrodes (see Figure 3.2). The sensing mechanism in most of the accelerometers is capacitance change related to the movement of that spring mass possibly in multiple orientations or axis. This sensing approach is used for high accuracy, stable, and low power measurements. Passive accelerometers are prone to electrical noise and temperature variations. However, bandwidth of such accelerometer is limited to a few hundred Hertz due to the physical geometry of the incorporated components as well as air trapped inside the IC. The capacitance can be measured as:

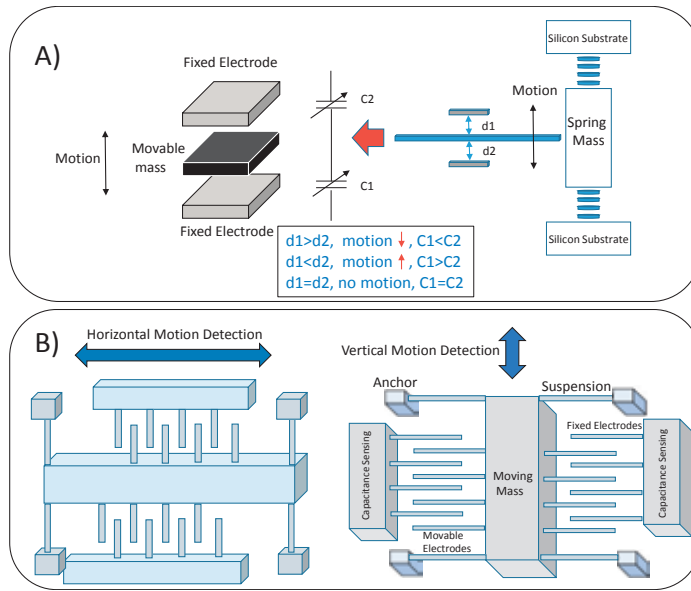$$C = \frac{\epsilon_0 \times \epsilon_r \times A}{D},$$
(3.2)

Figure 3.2: **Figure A** is an overview of capacitance accelerometer associated with a single moving mass. **Figure B** is a mechanical model of an actual accelerometer with components movable in two different axis.

where, C is capacitance (Farad), ϵ_0 and ϵ_r are respectively the free space and relative permittivities between the plates, and A is the area of overlap between the electrodes, and D is the separation distance between the electrodes. As Figure 3.2 A shows the motion of the mass is relative to the fixed electrodes ($d1$ and $d2$) leading to variation in capacitance ($C1$ and $C2$). By measuring the difference between the capacitors, $C2$ and $C1$, it is possible to derive the displacement of the mass and its orientation. In order to measure capacitance changes in different directions, the mechanical structures of an accelerometer can be tilted differently, for example, 90 degrees (see Figure 3.2 B).

Selecting a suitable accelerometer for a given application is of high importance. In order to find the most appropriate accelerometer, several main electromechanical characteristics need to be considered as described below:

Bandwidth (Hz): this parameter describes the range of vibration frequencies to which accelerometer responds. A bandwidth of 40-60 Hz is suitable for biomedical applications, e.g. for chest-acclerometery [134].

Sensitivity (mV/g or LSB/g): indicates the minimum detectable change in the output electrical signal within the determined range of mechanical change. The g is a unit of acceleration equal to the earth's gravity at sea level.

Voltage noise density (μg/$\sqrt{Hz}$): determines the noise level by measuring voltage noise changes with the inverse square root of the bandwidth. This means that the higher the sampling frequency the lower the accuracy.

Frequency response (Hz): specifies the frequency range (with a tolerance $\pm$ 5%) to calculate how much the device's sensitivity deviates from the reference sensitivity.

Dynamic range: specifies the range from the smallest to the largest detectable amplitude that accelerometer can measure before distorting the output signal, for instance $\pm 2g$, $4g$, and $8g$.

3.1.2 MEMS Gyroscopes

Unlike accelerometers that measure linear movements/accelerations along one or multiple axis, gyroscopes or angular rate sensors measure rotational movements (angular velocity) about a specific orientation with respect to inertial space. The main difference between the two sensors is that MEMS accelerometers do not respond to change in angular velocity caused by an imposed rotation (for instance a roll). The reason is that the inter-plate distances, $d1$ and $d2$ as shown in Figure 3.3 A, will not change in the course of rotation and therefore the accelerometer output will not respond to this change. Hence, the gyroscope structure is constructed differently by deploying an inner frame containing a resonating mass coupled to the substrate by springs (at 90 degrees) relative to the resonating motion (see Figure 3.3 B).
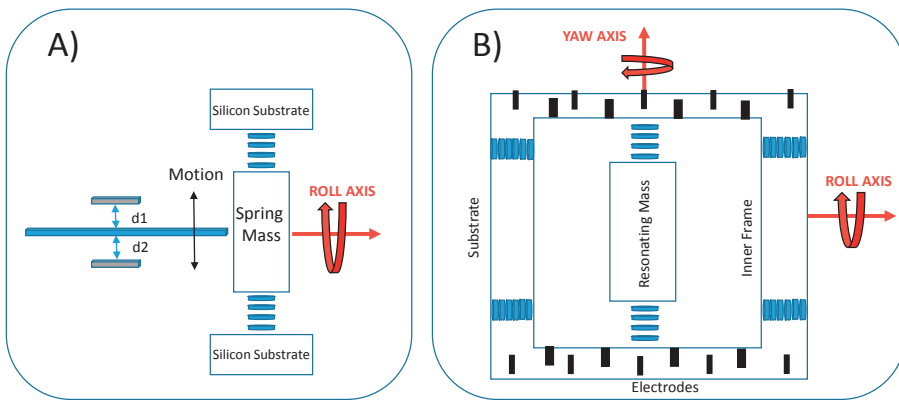

Figure 3.3: **Figure A** shows an overview of acceleration immunity to rotation. **Figure B** describes the inner and substrate representation relative to a moving mass in two different axis.

Mechanical oscillation between drive frames which are linked together by a spring is typically used to measure rotation by extracting the Coriolis force. In other words, the sensor angular velocity is derived by detecting, on the sensor frame, the motion deflections originated from a resonating structure. The deflections can be conceived when Coriolis force arises from the relative motion of the vibrating structure.

During driving mode, the two frames which oscillate in phase opposition generate Coriolis force. When a vibrating gyroscope is subjected to an angular motion, the Coriolis force deflects parts of the comb-like driving structure which move the deflection frame (Coriolis effect) and subsequently the capacitance between the comb structure is changed in proportion to the speed of rotation. The amplitude of this coupled oscillation can be used as the measure of the angular motion. A gyroscope operating based on this working principle is called Coriolis Vibrating Gyroscope (CVG). A CVG includes a mechanical structure with at least two modes of vibrations, namely *driving* mode and *sense of pickoff*, that are dynamically connected with Coriolis force [132, 133]. Several mechanical designs for micro-machined gyroscopes have been suggested, of which the most used designs reported in the literature and industrial products are *vibrating beams*, *vibrating forks*, *vibrating plates*, *vibrating shells*, and *surface acoustic wave (SAW)* structures. The interested reader may refer to [132] for more details regarding MEMS gyroscopes.

3.2 Cardiac Monitoring Systems

3.2.1 Electrocardiography

The electrical activity of the heart can be measured using electrocardiography with electrodes attached to the surface of the skin of the monitored subject [135]. Depolarization and repolarization of the myocardial cells create electrical current (and an electrical field) which can be measured between a pair of electrodes placed on the body's surface in specific positions on the skin. As such, an ECG measures voltage changes, amplifies micro-voltages, and visually displays a series of waves originated from heart's overall electrical activity. An ECG signal may look different in each measuring orientation, or namely lead, as the recorded angle of electrical activity alternates between the leads. Each lead measures voltage or electrical potential difference between two electrodes.

A typical ECG signal describes various electrical patterns derived from electrical impulses that spread throughout the heart. The main electrical components seen in an ECG signal — within a single cycle — are respectively P-wave (indicating atrial contraction), QRS-complex (depicting ventricular depolarization), and T-wave (representing ventricular repolarization). A single cardiac cycle (CC) or beat-to-beat interval in ECG is measured from the onset of R-wave to the following R-wave.

Electrocardiography (ECG) is the gold standard and yet the most widely used monitoring modality for diagnosis of heart arrhythmias and other abnormalities. ECG allows ambulatory or long-term monitoring of the cardiac operation along with manual or computerized interpretations made by experts (e.g. clinicians). However, despite the undeniable capability of ECG for representing the electrical performance of the heart, it gives no information how well the heart is functioning mechanically [13].

3.2.2 Ballistocardiography and Seismocardiography

The most frequently studied method for unobtrusive measurement of ballistics forces of the body is ballistocardiography (BCG) which relies on detecting the changes in the body center of mass [136, 137]. BCG measures infrasonic cardiac signals originating from body reactionary forces in response to the blood ejection into the vascular tree [17, 138]. First BCG measurement was made (using a spring weighing scale) by Gordon in 1877 [136] and its instrumentation was later improved by Star and Dock [137, 139] in 1939, Elliott et al. [140] in 1954, and Mounsey [141] in 1957. Modern BCG measurement methods include smart weighting scales, bed/chair piezoelectric sensors, inclinometers, and wearable sensors [17].

Seismocardiography (SCG) is a non-invasive heart monitoring technique which measures precordial accelerations caused by myocardial wall motions, ballistic forces due to blood flow, and respiration in the upper chest area. The concept of SCG technology was originally developed along with BCG investigations where Mounsey [141] and Elliott et al [140] considered the use of single axis accelerometer sensors to measure chest accelerations, namely precordial ballistic forces due to the palpation of the heart beat. The term seismocardiography was first denominated by Bozhenko in 1961 [142], and its clinical applications were later introduced by Zanetti and Salerno [143–145]. SCG contains useful information about the translational heart motions originating from the contraction and relaxation of the left ventricle [146]. By means of SCG and BCG, it has been possible to record and study cardiac mechanics and hemodynamic variables.

Today, multidimensional SCG can easily be obtained by mounting a tri-axial accelerometer sensor on the upper chest area so that the x-axis corresponds to the right-to-left lateral accelerations, y-axis to the head-to-foot aligned accelerations, and z-axis to the dorso-ventral accelerations caused by precordial movements. The SCG signal is constituted from high frequency components ($>$70Hz) representing cardiac sounds, S1 and S2, and low frequency components (4-40 Hz) reflecting cardiac physiological events such as MVC, AVO, AVC, and MVO [17]. Salerno and Zanetti studied SCG waveforms along with ECG and cardiac ultrasound and labeled coinciding phenomena corresponding to specific cardiac events [143] as shown in Figure 3.4.
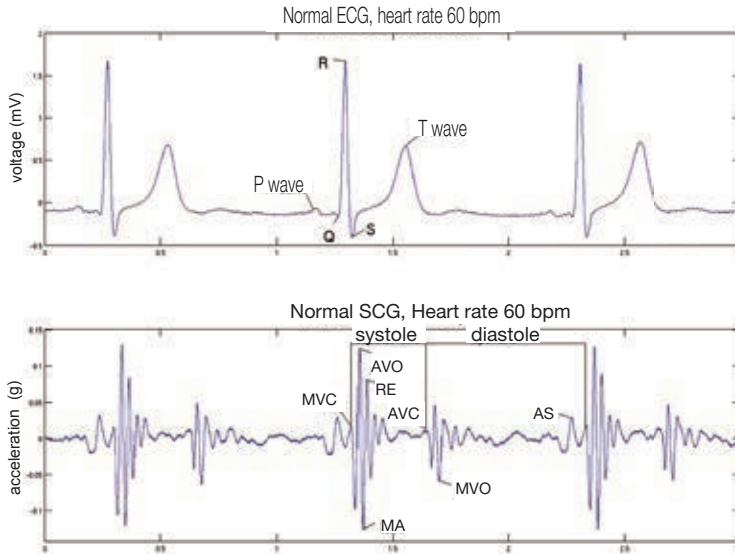
18

Figure 3.4: SCG time intervals and waveform annotation based on ECG, Doppler, and M-mode echocardiography. Systlic and diastolic events are respectively: MVC, AVO, rapid ejection (RE), maximum acceleration (MA), AVC, MVO, and atrial systol (AS).

SCG and BCG can be used for unobtrusive long term monitoring of LV to estimate hemodynamic variables, cardiac abnormalities, and breathing disorders via low-cost wearable or portable devices [127, 147–150]. Several clinical applications have been proposed for the BCG/SCG based monitoring approaches such as detection of CAD [144, 151], AFib [127], HF [152, 153], MI [149], hemodynamic parameters estimation [154, 155], sleep disorders [156], blood pressure monitoring [157], and for the treatment of acute coronary ischemia [158]. Generally, findings in SCG/BCG studies indicate that mechanical signals have great potential clinical applications in cardiac performance assessment [17]. Recently, SCG has been proposed for medical imaging applications in which the quiescent phases of cardiac cycle can be estimated by SCG for motion correction in computed tomography (CT) [159–162].

3.2.3   Gyrocardiography

Gyrocardiography (GCG) refers to a measuring modality where precordial rotational movements are sensed using a sensor of angular motion, for instance, a gyroscope, attached to the skin of the chest. The gyroscope sensor is configured to measure chest motion signal, an angular ballistocardiograph signal, that is representative of rotational recoil micro-movements in response to the myocardium motion within the chest wall [9].

GCG technique is solely based on tracing the precordial microvibrations using a MEMS gyroscope sensor placed on the skin anterior to the sternum. The gyroscope measures rotational velocities correspond to physiological events such as the moments of LV valves openings and closings. A benefit of the GCG is that a gyroscope measures angular motions induced by the heart pulsation [163] and the sensor is more tolerant to noise [164] and linear body micro-movements [165]. Compared to the linear acceleration/velocity signals, the gyroscope waveforms remain more monomorphic and stationary. GCG can accurately detect very small rotational displacements with high temporal resolution, and thereby can provide information on cardiac time intervals, hemodynamic variables and myocardial contractility [163]. This technique can be easily incorporated to other modalities such as ECG, BCG and SCG for better detection of cardiac diseases, such as arrhythmia [113], acute myocardial ischemia [166], and

other heart diseases [167]. Figure 3.5 shows BCG, SCG, and GCG signals with labels representing a rough estimation of the physiological events in cardiac function.
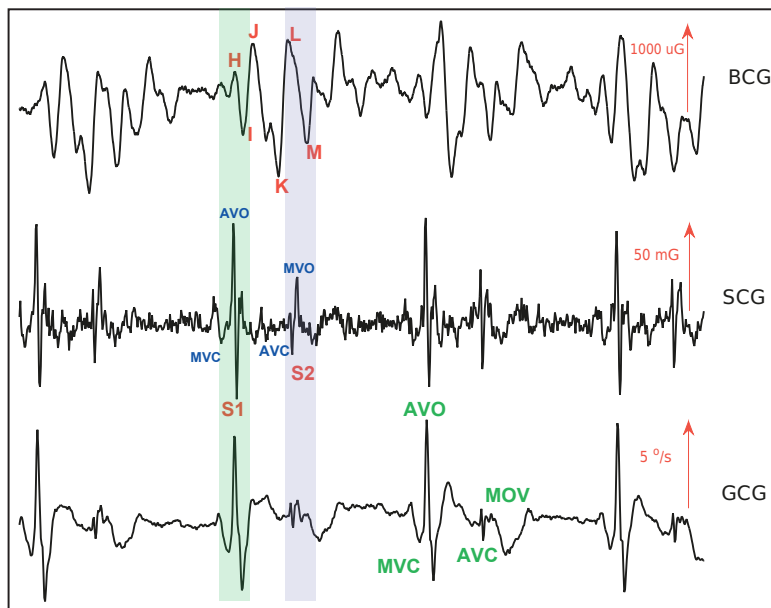

Figure 3.5: Illustration of typical BCG, SCG, and GCG signals with corresponding waveform annotations obtained respectively by a contact-less bed sensor (highly sensitive inclinometer) [168], chest accelerometer, and gyroscope sensor.

Recently published research has described the feasibility of the heart monitoring using miniaturized accelerometer and gyroscope sensors in Google glasses, wrist worn devices, smart phones, and chest worn patches [169–171]. Additionally, the body kinetic energy analysis, also known as the multidimensional kineticardiography (MKCG), has been recently introduced which is based on placing inertial sensors on the center of mass of the body, for example, on the skin of the human back, and thereby on measuring the kinetic energies and powers of the body. This method, which resembles angular ballistocardiogram, has potential in evaluating kinetic energy transferred from the heart in patients suffering valvulopathy and heart failure [167]. Other investigators such as Marcelli et al. [34,36], Hyler et al. [172], and Grymyr et al. [37], on the other hand, presented in vivo techniques based upon implantable gyroscope and accelerometer sensors in order to trace left ventricular motion changes and assess cardiac function. These studies, although very preliminary, indicate a promising approach which may yield to a prospective strategy suitable for implantable devices for the continuous monitoring of cardiac function.

3.2.4 Background of Heart Rate Estimation with MCG

A great deal of previous research into MCG signal processing has focused on heartbeat detection for various applications, such as heart rate monitoring and arrhythmia detection. To date, several different approaches have been suggested for estimating beat-to-beat intervals in mechanical cardiac signals, for example, see [173–177]. As there are many different sophisticated algorithms for heartbeat detection in ECG, there are also various methods to detect cardiac impulses in MCG signals. However, detecting heartbeats from SCG/BCG/GCG signals is much more complicated than in ECG, because the mechanical signals are often variable and inconsistent due to the inter- and intrasubject morphological variations.

Mechanical signals in general pose a wider variability in time, amplitude height, chronology of peaks and overall shape. In this section, a number of techniques for heartbeat identification in MCGs will be briefly reviewed.

Currently established algorithms in the field of cardiac signal processing (including only ECG and MCG) are dedicated to measure either instantaneous heart rate or averaged cardiac cycles taken over several consecutive heartbeats.

Instantaneous heartbeat detection approaches can be divided into two categories: 1) ECG-dependent, and 2) ECG-independent methods. Algorithms that rely on the ECG fiducial points ultimately need ECG R-peaks for accurate detection of heartbeats. These methods typically consist of a band-pass filter to remove the respiratory and noise effect, and a complementary stage to localize MCG heartbeats through a rule-based process [150, 178–182]. Khosrow-Khavar et al. (2015) presented a primary method for automatic annotation of high frequency components in the SCG signals by detecting local maxima in several SCG derived envelopes [150]. This approach extracts different envelopes of the SCG signal, and using ECG R-waves (as the fiducial points) as well as a searching window operation detects cardiac impulses in the SCG signal. In a follow-up study, they developed a state-of-art algorithm for robust and standalone delineation of SCG signal which could detect heartbeats as well as moments of cardiac events using manual annotation of cardiac cycles and a complementary classification model [183]. However, the standalone delineation of cardiac cycles, that is identifying major cardiac activities without using ECG, typically suffers from strong assumptions on the mechanical waveforms, which may result in false annotation of SCG signals. Rienzo et al. (2017) also developed an envelope-based detection algorithm based on deterministic windowing for accurate heartbeat detection in SCG [184]. The method, although yielded promising results, it still seems to be ECG-dependent. In a recent study, Hurnanen et al. (2017) presented a new approach based on sensor fusion, narrow-band filtering, and successive mean quantization transform [185] to estimate beat-to-beat cardiac cycles in a large dataset obtained by smartphone mechanoacrdiography. Detection performance of this ECG-independent approach, validated by PPG sensing, yielded a promising direction for ubiquitous heart rate monitoring.

In general, methods relying on hard rules or fixed thresholds settings are very susceptible to amplitude fluctuation in SCG/BCG signals. Additionally, due to huge inter-subject variations in the signal morphology, setting proper thresholds is laborious and may not always reveal successful estimation of beat-to-beat intervals [148, 186]. In 2013, Garcia-Gonzalez et al. compared four previously developed heartbeat detectors based upon continuous wavelet transform, cross-correlation, and bandpass filtering in SCGs, and concluded that narrow or brick-wall band-pass filtering outperforms the other types of heartbeat detectors [176]. However, band-pass filtering causes additional distortion on the SCG signals, specifically in the presence of motion artifact, which may result in quantitative inaccuracy in heart rate estimation. Hernandez and colleagues detected heart beats with an adaptive multi-parameter function for feature extraction from mechanical heart signals [170]. Parameter optimization in such a framework is a very cumbersome process due to the interpersonal variations and inconsistency between the cardiac signals' morphology. In 2008, Shin et al. developed a classification approach based upon template-matching and cross-correlation in order to automatically detect heart beats in BCG signals [187]. Later in 2011, Brüser et al. developed an unsupervised learning approach based on k-means clustering for beat-to-beat estimation in BCG recordings [173]. In a follow-up study, Brüser et al. (2013) presented a flexible algorithm in which a pitch tracking approach was used to estimate fundamental frequency of the BCG signal [174]. Later in 2014, Paalasmaa et al. presented a pioneering approach to model the heartbeat complex in BCG signal in which can adaptively find positions of heartbeat using hierarchical clustering. However, algorithms solely based on clustering techniques typically suffer from miss-detection of heartbeats [175]. Recently, Ashouri et al. (2017) presented a promising technique based on regression modelling and unsupervised learning to obtain an accurate solution for PEP estimation from the best performing regression model as well as the best accelerometer sensor location on the body surface [188]. A new approach based on unsupervised learning and envelope detection is presented in this Ph.D. work (as described in Sec 6.2.3) where joint accelerometer and gyroscope derived signals are used for fully automated and standalone estimation of heartbeats.

Other group of heart rate estimator methods are based on computing the median heart rate over a period of time such as fundamental frequency [174], fuzzy neural networks [189], auto-correlation [174, 190–192], hidden Markov model [193], power spectral density [169, 171], and wavelet decomposition [194]. These methods although are less prone to the morphological characteristics of the signals, they are unable to provide information about either irregular heartbeat or rhythm variation in the inter-beat intervals specifically for heart rate variability (HRV) analysis. Moreover, these methods may fail to represent the correct heart rate when the signal is non-periodic, e.g. due to cardiac arrhythmia, or strong frequency components exist in the signal. Despite various advanced signal processing methods employed for heart rate estimations, merging sensor data by using either multiple identical sensors or multiple particular sensors (e.g. optical, force, accelerometer, and gyroscope) are recently established that can be advantageous for further analysing of heart's performance [163, 164, 195]. Moreover, it is shown that multi-modal techniques may improve the heart rate estimation in unobtrusive monitoring of heart activity.

In recent years, there has been an increasing interest towards emerging techniques based on multi-channel data fusion, sensor fusion, and sensor array structures to enhance the accuracy and robustness of cardiac cycle delineations [171, 195–200]. Deconvolution, pitch-tracking, Kalman filter, and Bayesian fusion have been recently suggested for multimodal or multi-source data fusion [160, 195, 201, 202]. The use of multiple sensors — either measuring the same or different physical quantities — has been recognized as an advantageous technique because this approach offers diversity in the signal acquisition and processing.

3.3 Respiration Monitoring

3.3.1 Background of Respiratory Monitoring Techniques

Respiration monitoring can be performed by various techniques, for which the most widely used methods include spirometry or airflow sensing [203], transthorasic impedance [204, 205], magnetometer [206], elastic belts (consisting of pressure, strain-gauge transducer, capacitance, load-cell sensors) [207–209], optical techniques and photoplethysmography [210], camera and laser beam [211], and various MEMS motion detectors [212] for tracking variations in thorax volume and pressure that give rise to chest wall and abdomen. Table 3.1 represents different methods for respiration monitoring reported in the literature [213]. Sensing principles for respiratory monitoring devices in this table fall into three categories as: (1) observing movement, volume, and tissue composition changes, (2) measuring airflow, and (3) blood gas concentration measurement. Measuring the volume or circumference of the ribcage and abdomen is commonly obtained by transthorasic and abdominal impedance, strain, pressure, fibre-optic sensors integrated in chest/abdomen straps fasten around the body [213]. Other systems based on magnetic field strength [206] and microwave radiation [214] have been introduced which require infrastructures around the measuring subject. An indirect measuring of respiration is based on plethysmography where blood concentration of oxygen and its changes over time is measured.

Among these techniques, several different respiration monitoring systems have been to date investigated (or routinely used) for gated PET, 4-dimensional (4D) CT, and gated radiotherapy. Such motion tracking systems include pressure sensing (stress change measurement with a load-cell sensor), spirometry (measuring air flow to and from lungs), temperature sensing (airflow temperature changes to and from lungs), and real-time position management (RPM) system for respiratory gating [215]. Bio-impedance based respiratory gating has been also introduced for intrathoracic respiratory motion tracking [216]. However, employing these respiratory gating devices is laborious due to the need for complex logistics, possibly long data processing, and lack of enough precision which may result in false outcome with increased patient discomfort and subsequent difficulties for the clinicians [217, 218]. Accelerometeric and gyroscopic respiration monitoring have been recently emerged as alternative methods of the intrafraction motion sensing [212]. MEMS motion detectors are micro-sized and sensitive devices to organs' intrafraction variation and can offer simultaneous cardiac and respiratory signals. In the context of this

Table 3.1: Methods and devices for respiratory monitoring using detection of changes in tissue size, volume, and air flow [213].

Sensing Modality	Measurement Quantity	Typical Sensor Type, Position, and category
Transthoracic Impedance	Thoracic Impedance	Skin electrode on the chest (1)
Inductance Plethysmography	Abdomen and Thoracic Circumference	Embedded coils around abdomen and chest (1)
Fibre-Optic Plethysmography	Abdomen and Thoracic Circumference	Fibre-optic strain gauge around abdomen and chest (1)
Strain Gauge Transducer	Abdomen and Thoracic Circumference	Resistive strain gauge around abdomen and chest (1)
Mutual Inductance	Thorax Volume	Magnets on chest (1)
Spirometry	Lungs Volume	Gas flow sensor (2)
Magnetometer	Thorax Volume	Magnetometer sensor (1)
Microwave Radiation	Thorax Volume	Waveguide termination (1)
Piezoelectric Sensors	Thorax Volume	Pressure and Piezoelectric sensors in mattress (1)
EMG	Muscle Activity	Skin electrodes (1)
Capacitance on Distance	Thorax Volume	Capacitance measurement (1)
Photoplethysmography	Blood Gas Change	Fibre-optic sensor (3)
Video Camera	Thorax or Abdomen Motion	Camera and Marker (1)
Chest-Accelerometry	Thorax Translational Motion	Accelerometer or inclinometer sensor (1)
Rotational Sensing	Thorax Rotational Motion	Angular rate or gyroscope sensor (1)

work, respiration monitoring modalities are considered for PET/CT imaging applications as they are meant to streamline respiratory gating in PET/CT imaging. A recent review in PET instrumentation was given in [219]. Figure 3.6 shows diverse commercial respiration monitoring systems implemented for PET/CT imaging techniques. In this study, we considered only methods illustrated in (A) and (B) insets for verification tasks as described in the following.
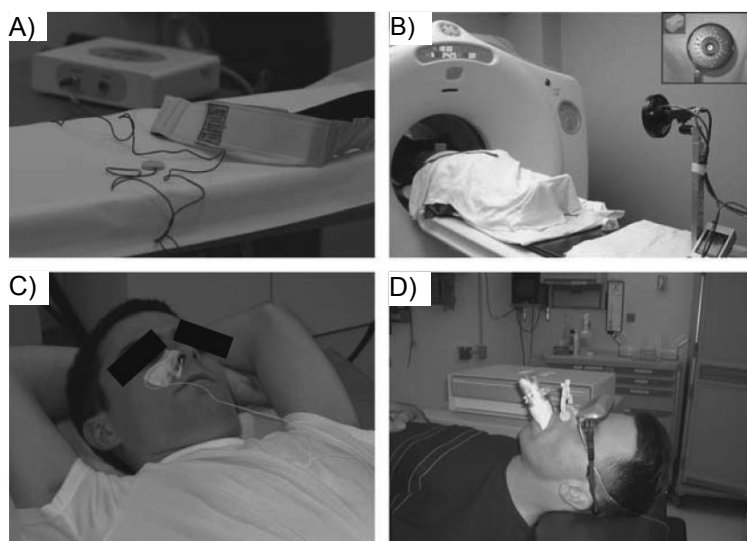

Figure 3.6: **Figure A** shows AZ-733V (Anzai Medical Corp., Tokyo, Japan) pressure sensor embedded into an elastic chest belt. **Figure B** shows RPM system with an infrared reflective marker placed on a plastic box positioned on the patient's thorax. **Figure C** shows air temperature monitoring (BioVet CT1 System; Spin Systems, Brisbane, Australia) placed close to the patient's nostrils. **Figure D** shows air flow measurement by placing spirometer close to the patient's nostrils (PMM Spirometer; Siemens Medical Systems, Erlangen, Germany [220]) or mouth (CPX Spirometer; Medgraphics, St Paul, Minnesota, USA [221]) (From: [217, 220–222] © Reprints with permission).

3.3.2 Piezo-electric Respiration Belts

Respiration belt sensors contain a piezo-electric transducer attached to an elastic belt dedicated to measure the variations in the thoracic circumference. The belt is usually fastened around the middle part of the ribcage of the subjects to obtain thoracic or abdominal circumference during respiration. The sensing module is interfaced to a dedicated data acquisition system where the change in the pressure, and thus breathing amplitude, is converted to an electrical signal. The respiration signals derived from the belt inhalation, expiration and breathing strength are used to derive breathing rate. For the imaging applications, the transducer is used to characterize breathing pattern changes and adapt a respiratory gating system accordingly while imaging data are streaming.

3.3.3 Optical Motion Tracking

A real-time position management (RPM) system (Varian Medical Systems, Palo Alto, CA, USA) is commonly used to remotely monitor longitudinal chest motions. The RPM system is a video-based system (infrared tracking camera) that consists an array of LEDs that emit infrared light toward a marker block which is made from a plastic box with two or more reflecting dots. The marker is usually placed on the patient chest or abdomen within view of the tracking camera. The reflected light returning back (from the dots on a plastic marker) to the camera are captured as a signal which corresponds to the motion of chest or abdomen. A predictive filter is also deployed along with this configuration which predicts the patient breathing pattern and continuously checks that this pattern is normal. Currently available RPM systems rely on an infrared tracking camera and a plastic marker block which inaccurate placement of the marker block on the targeted location as well as very low breathing amplitude are the major limitations of this system that cause additional inaccuracies in quantitative PET/CT imaging [223].

3.3.4 MEMS-Based Respiration Tracking

The robustness and functionality of the MEMS accelerometer-derived respiration signals (ADR) for dual cardiac-respiratory gating was validated against a respiration belt [224]. With respiration belt, respiratory phases (normal, slow, and fast-paced) were analysed and tested against ADR signal. In continuation of this investigation, longitudinal chest motions induced by breathing act were measured using a dual-sensor patch to trace breathing curves. Accordingly, ADR and gyroscopic-derived respiratory (GDR) tracking signals are considered for potential respiratory gating applications. Figure 3.7 shows PET/CT imaging set up including MEMS gating configuration, as well as golden standard validation modalities to evaluate MEMS derived respiration signals versus RPM (Figure A) and respiration belt (Figure B) measurements.

The ADR and GDR signals were evaluated versus reference RPM signals in terms of amplitude and phase [226]. Respiratory phases were determined using a peak detection algorithm which was sensitized to the minimum peak height and the minimum separation distance between the peaks of both ADR/GDR signal and the reference respiration modalities. The result of ADR/GDR respiratory signals validation versus the reference respiratory cycle duration (peak-to-peak) using Pearson correlation and Bland Altman plot [227] are reported in the Study III.

3.4 Medical Imaging Modalities

3.4.1 Echocardiography and Strain Rate Imaging

Cardiac ultrasound scan is a non-invasive imaging technique based on sound (pressure) waves of frequencies exceeding the range of human auditory. Sound waves originated from a vibrating object (e.g. crystal elements in ultrasound's transducer) are transmitted through a medium (e.g. chest wall, the pericardium, and the heart) generate waves of alternating density. The resulting velocity due to the wave propaga-
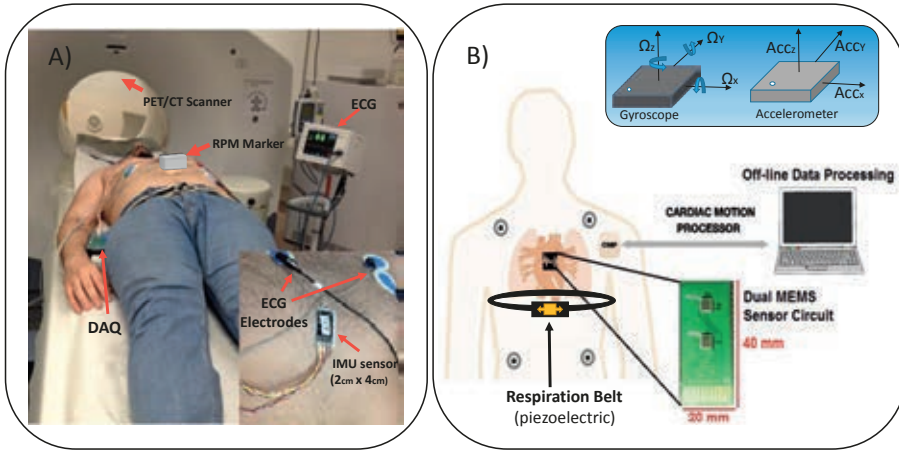
Figure 3.7: **Figure A** represents PET imaging and corresponding data acquisition set ups including ECG, RPM, and MEMS accelerometer and gyroscope sensors. **Figure B** shows general schematics for validation of accelerometer and gyroscopic derived respirations against respiration belt (From: [225] © Reprint with permission).

tion from the medium builds the basis principles for imaging of the heart's structure and studying blood flow [228].

Ultrasound images are formed from transmitting ultrasonic pulse streams into the body and measuring reflections return to the transducer as an echo. Ultrasound imaging requires a transducer/probe containing an array of piezoelectric crystals directing and receiving sound waves and convert the echo amplitudes into electrical signals. This *Pulse-Echo* process is the basic principle to synthesize a grayscale two-dimensional tomographic ('slice') view of a tissue. Almost all ultrasound systems use *phased array* technology to scan ultrasound beam by which echo ultrasonic waves are transmitted and returning pulse echoes are received (see Figure 3.8 A). The echo signals converted to a single ultrasound pulse represent the intensities of the echo reflections as shown in Figure 3.8 B [228].
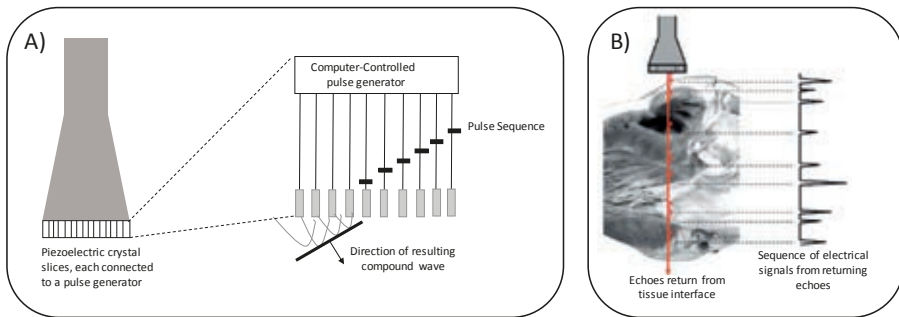

Figure 3.8: **Figure A** shows ultrasound beam direction controlled by pulsing the crystal elements in sequence. **Figure B** illustrates conversion of echoes returning from tissue interfaces into electrical impulses (from [228]).

The basic image data comprises a series of digitized numbers — representing echo amplitudes — which are processed to show reflected ultrasonic waves from surfaces of two materials with different ultrasonic reflecting properties. In practice, these reflected echoes are reconstructed to images with

different techniques, of which the most commons are B-mode (B for brightness), which converts pulse echo signals into brightness-modulated dots on a display screen, and M-mode (M for motion), which uses B-Mode to display echoes from a moving organ, such as the valve leaflets and myocardium wall. M-Mode provides fairly high quality temporal resolution of motion patterns, allowing deeper evaluation of the heart functioning. However, with advances in real-time 2D imaging, Doppler, and color coded flow imaging, these modes of visualization are of much less importance today [229]. Three dimensional images are also obtainable by employing 3D imaging transducers (transesophageal) as well as advanced computer-generated texturing techniques that create a solid 3D image of the tissue.

Echocardiography is a point-of-care cardiac ultrasound (US) imaging which is routinely used for diagnostic cardiac motion visualization. This method similarly follows echo-pulse generation and detection process through the heart's chambers, valves, walls and the blood vessels. Echocardiography provides anatomic distance and volume measurements, intra-fraction motion studies, blood velocity measurements or Doppler ultrasound, 3D imaging, and tissue strain measurements.

Tissue Doppler imaging (TDI) technology is mainly used in echocardiography that measures the velocity of the heart muscle or myocardium by Doppler effect — as for moving object like heart, the frequency or wavelength of the backscattered echoes is changed by the Doppler effect [228]. TDI evaluates the heart's functionality both quantitatively and qualitatively. TDI is often used to assess the causes of abnormal heart sounds, the size of the heart, myocardial wall motion abnormality and deformation, systolic and diastolic dysfunction, heart valve problems, congenital heart defects, coronary reserve flow, and other diagnostic purposes [229].

In the course of this Ph.D. work, representative echocardiographic images are created as two- or three-dimensional images of the heart using TDI technique for quantitative assessment of the cardiac mechanical activity. By placing a region of interest (ROI) around the heart's tissue or valves, measurements of systolic and diastolic time intervals, as well as myocardium velocity and strain rate (myocardial wall deformation) information can be obtained. Strain analysis can help in quantifying mechanical dyssynchrony and contribute in predicting response to cardiac resynchronization therapy (CRT) [230]. In clinical considerations, the strain rate and the strain are used to detect ischemia and infarction as well [33]. Furthermore, myocardial dispersion, an electromechanical delay between ECG Q-wave to the maximal TDI strain, can reflect the heterogeneity of myocardial systolic contraction and has been suggested as an indicator for susceptibility to arrhythmias in different heart disease groups such as heart failure, CAD, and MI [79].

In a post-processing stage, using for example speckle tracking echocardiography (STE) technique — natural acoustic markers resulting from the interaction of ultrasound energy with tissue — it is possible to assess three myocardial deformation components: longitudinal, radial, and circumferential. STE is commonly used for measuring twisting mechanics as well as deformation rates of the heart muscle. Here, a brief introduction on principles of deformation rate, or more precisely strain rate, calculations using this image processing technique is presented.

In conventional echocardiography considerations, velocity and displacement characterize wall motion, while wall deformation can be described with strain and strain rate terms. The concept of strain for three dimensional object deformation is complex but for the sake of simplicity it can be explained for a one-dimensional (1D) object as described in [231]. In principle, the only feasible deformation for a 1D object is shortening or lengthening and the amount of deformation can be estimated as follows:

$$\epsilon = \frac{L - L_0}{L_0}, \tag{3.3}$$

where ϵ is *strain*, L_0 is baseline length, and L is the length change at the time of measurement. As the length changes over time, the instantaneous strain can be defined as:

$$\epsilon(t) = \frac{L(t) - L(t_0)}{L(t_0)}, \tag{3.4}$$

where $\epsilon(t)$ is instantaneous strain. The amount of strain or deformation is shown in % and positive and negative strain values describe the thickening and shortening of myocardial, respectively. Strain rate (SR)

is another deformation parameter which describes the rate by which deformation occurs and is expressed by s^{-1}. The strain rate or local rate of deformation then equals velocity difference per unit length:

$$SR = \frac{\Delta \epsilon}{\Delta t} = \frac{\Delta L/L_0}{\Delta t} = \frac{\Delta L/\Delta t}{L_0} = \frac{\Delta V}{L_0}, \qquad (3.5)$$

where ΔV is the velocity gradient of the myocardium [231]. Figure 3.9 shows mathematical and schematic relation for myocardial deformation/strain rate as explained previously.
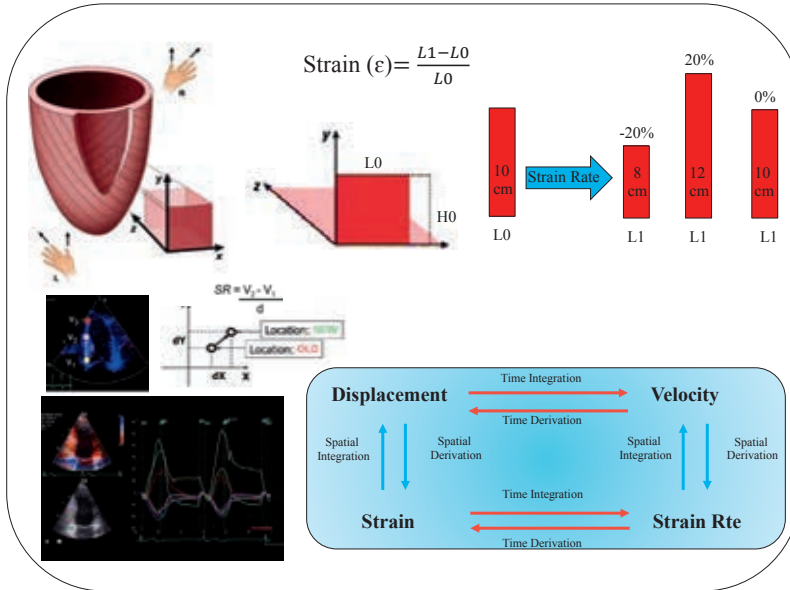

Figure 3.9: Tissue deformation or strain is defined as the change in dimension or length (L1-L0) over the initial length (L0) of the region of interest. Strain rate is calculated with tissue velocity changes as the difference between tissue velocity samples (V2-V1) normalized to the travelling distance between the velocities (d) (partially from [33, 230] © All reprints are with permission).

In considerations of this dissertation, reference echocardiography examination mainly was conducted mainly for two purposes: 1) validating cardiac time interval and 2) assessing strain rate prospectively calculated through SCG/GCG signals as described in Study III and IV.

3.4.2 Cardiac Nuclear Imaging

Conventional nuclear medicine is still the major player in cardiac nuclear imaging. Nuclear cardiology includes myocardial perfusion imaging (MPI), single photon emission computed tomography (SPECT), and positron emission tomography to detect indications of CAD and for diagnosis and risk stratification of patients with ischemic heart diseases [232]. These nuclear imaging modalities rely on different radio-tracers for optimal clinical cardiac imaging with high resolution and enhanced signal-to-noise ratio. Cardiac PET scan is an alternative imaging technology to conventional SPECT which is commonly configured with joint computed tomography (CT) or magnetic resonance imaging (MRI) to evaluate the heart for coronary artery disease and cardiomyopathy (diseases of the heart muscle due to, for example, heart attack) [61].

Non-invasive detection of atherosclerotic plaque inflammation is usually performed by state-of-art 18F-fluorodeoxyglucose (FDG) and PET imaging [49,58–60]. Other diagnostic technique for atherosclerotic plaque inflammation includes anatomical demonstration of vessel lumen narrowing, for example,

X-ray contrast angiography (CA). However, CA is insufficient and impractical for the quantitative assessment of plaque vulnerability to rupture [49]. Plaque imaging can be also performed with cardiac perfusion scan using ^{15}O-water (radio-water), ^{13}N-ammonia, and ^{82}Rb-Rubidium as radio-tracers and conventional SPECT with ^{99m}Tc-technetium labelled perfusion tracers [232]. A fundamental limitation of the cardiac PET is that myocardial wall movements and respiratory motions reduce the quality of the obtained images [217, 233]. Currently used approaches for tackling intrafraction-based motion artefacts involve gating the PET data based on the timing of quiescent periods of cardiac and respiratory cycles [215, 217]. To deal with this challenge, this dissertation doctoral dissertation concentrates on a novel gating concept, named *MEMS Dual Gating*, which is based on inertial motion detectors to eliminate motion-related inaccuracies in cardiac PET by tracking intrafraction motions induced by cardiorespiratory mechanical activities. More details on the working principles of PET imaging, description of methods for motion correction in cardiac PET imaging, as well as clinical objectives for quantitative improvements of dual-gate PET are given in Chapter 4.

Chapter 4

Positron Emission Tomography

4.1 Physical Principles of PET

Positron emission tomography (PET) is a non-invasive functional imaging technique which may be considered as the gold standard for clinical examinations of coronary arteries inflammation due to atherosclerosis and oncological investigations. Today, PET imaging is a widely used tool to observe metabolic processes in the body for diagnosis, staging, therapy monitoring, and assessment of recurrence in cancer and cardiovascular diseases [234]. Principles of PET imaging was introduced in 1950s, but its clinical applications emerged in 1990s when the intensive development of scanners enabled both high image quality and intelligent quantitation. Modern PET scanners are multislice devices allowing acquisition of 3D images with a sensitivity up to 22 cps/kBq and a large axial field-of-view (up to 26 cm). New PET scans can take as short as 5 minutes and deliver the acquired image in 30 seconds [235].

The physical basis of PET imaging is described in Figure 4.1. In principle, PET imaging relies on a radioactive transformation by which annihilation photons are generated. Annihilation is a process where a positron — which has lost its kinetic energy — interacts with an electron and results in two 511-keV photons each emitting in nearly opposite directions. Scintillation crystals coupled to photomultiplier tubes (PMTs) are generally used to detect incident of annihilation photon that creates tens of thousands visible wavelength photons (about 1 eV energy each). These crystals measure the two annihilation photons that are generated back-to-back after positron emission from a radiotracer molecule, for example, 18F-fluorodeoxyglucose (FDG), to mark a specific function in the body [234].

Annihilation photons are susceptible to interact with tissue (scatter event). Attenuated photons that interact with the tissue before arriving at the surface of the detectors are called scatter photons that are assigned incorrectly to the line-of-response (LOR). These scatter photons are removed from the correct LORs, either by Compton scattering or photoelectric absorption, through a process called attenuation correction (AC).

4.2 Reconstruction of PET images

Two dimensional PET image reconstruction is based on LORs which lie within a defined imaging plane. PET data streams are collected along LORs through a 2D object $f(x, y)$. As shown in Figure 4.2 the LORs are formed into sets of projections, line integrals for all s for a fixed orientation ϕ. Collection of all projects for $0 \leq \phi \leq 2\pi$ creates a 2D function of s and ϕ that is named *sinogram* [236]. Sinograms are obtained prior to image reconstruction as they are 2D representation of image data in a matrix form. The rows of the sinogram matrix describe the radionuclide accumulations of the object, $f(x, y)$, in all projections and columns represent its radial distance from the image centre [236].

There are two general ways to reconstruct nuclear images, *analytic* reconstruction methods, of which the most common approach is filtered back projection (FBP), and *iterative* image reconstruction, of which the most commonly used iterative method is ordered subsets expectation maximization
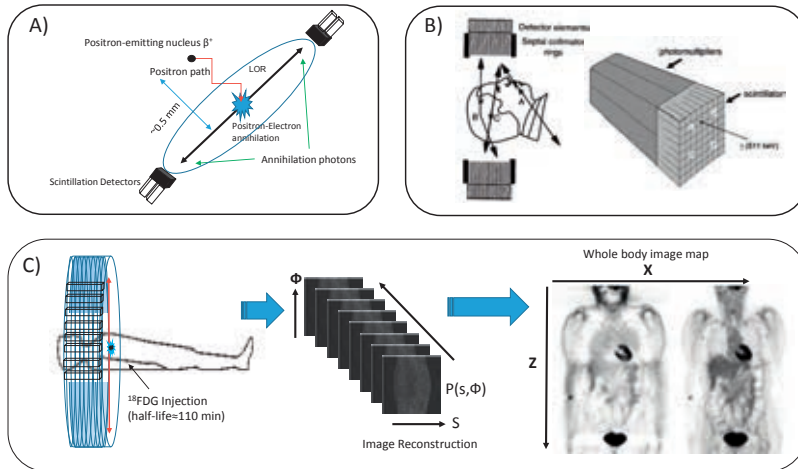
Figure 4.1: The principles of PET imaging shown schematically. **Figure A** shows the detection in coincidence of the annihilation photons. **Figure B** indicates detector elements and collimator rings preventing photons from scatter events. **Figure C** describes 18FDG injection and the detection of a pair of annihilation photons in coincidence by a multiring PET camera and further steps to reconstruct the image (sketched from [229]).

(OSEM) algorithm that aims at higher spatial resolution and signal-to-noise ratio than back projection images [236].

Four-dimensional image reconstruction methods — based on either linear or non-linear parameter estimation — can reduce the impact of noisy PET using spatio-temporal functions chosen to approximately represent the radiotracer distribution [237]. Other techniques will be also able to incorporate information on subject anatomy and motion, along with cardiac and respiratory motion, yielding noise/motion artifact free PET images by 5-dimensional or 6-dimensional image reconstructions [237]. In the context of this thesis, these mathematical modellings, as well as anatomical and motion characteristics, constitute the concept of fully 4D imaging.

Mathematical principles of above-mentioned image reconstruction methods in emission and transmission tomography seem to be generally very advanced topics and are beyond the scope of this research.

4.3 Motion Artifact Problem

In today's medical imaging and radiation oncology, intrafraction variation — intentional or unintentional organ movement — in respiratory, cardiac, and gastrointestinal systems is the leading cause of inaccuracy and uncertainty [238]. Displacement of organs due to respiratory and cardiac motion results in spatial blurring and motion artifacts that cause quantitative inaccuracies and misguided interpretation in PET and CT imaging [239]. Misguided evaluation of PET and CT images lead to incorrect diagnosis and treatment decisions; for example, insufficient or unnecessary treatment may occur, if motion affected PET and CT images are used for treatment planning in radiotherapy [240]. In oncological imaging, motion artifacts result in difficulties in delineating organ or tumor boundaries, and failure in recognizing small mobile volumes that are potentially cancerous. For example, respiratory and heart motions may cause underestimation of standardized uptake value (SUV) and variation of lesion volume [241]. Moreover, radiation delivery in the presence of intrafraction organ movement results in a deviation between the intended and delivered dose distributions, which might result in increased organ-at-risk dose and reduced dose in the planned target volume [242]. Therefore, the degradation of image quality due to intrafrac-
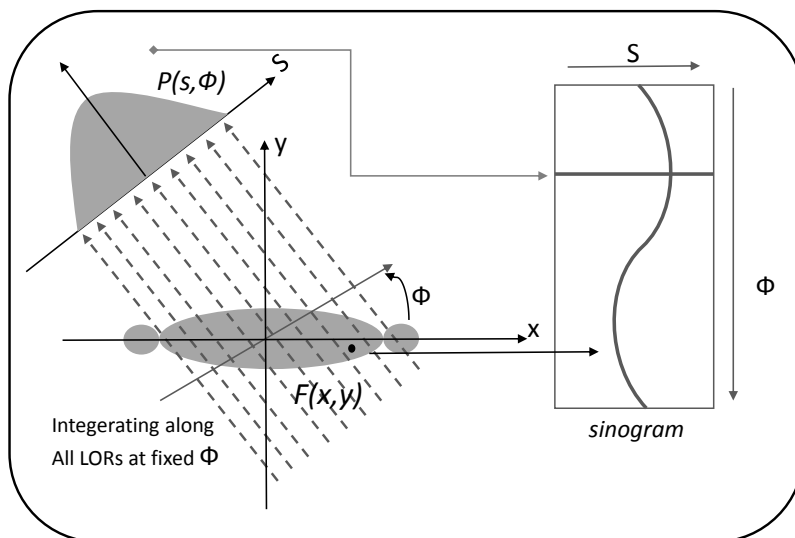
Figure 4.2: Sinogram formation process based on projection P(s,ϕ) created from line integration along all parallel LORs at an angle ϕ. Each projection is organized into a sinogram (sketched from [236]).

tion motion and subsequent effects on radiotherapy dose planning and delivery reduce the reliability and accuracy of the clinical interventions, leading to incorrect diagnosis, unnecessary treatment, and insufficient therapy. During normal breathing, the diaphragm moves several centimeters (cm) and chest wall several millimeters (mm). Cardiac wall movement (myocardium longitudinal and radial deformation) results in displacements over 1 cm and consecutive beat-to-beat variation in blood flow (ballistic changes) can cause artifact specifically for brain imaging. Brain pulsations due to ballistic recoil forces can cause non-rigid displacement of up to 0.1 mm, even healthy and cooperative subjects show spontaneous head motions up to 1 mm [243].

4.4 Methods for Motion Compensation in PET

To deal with motion-related inaccuracies in PET/CT imaging, respiratory and cardiac gating methods are the most common approaches used for motion correction in nuclear medicine imaging. Gating in a simple definition means dividing the PET data into individual bins that correlate to phases of respiratory and/or cardiac motion by overlaying corresponding time-stamped data [241]. In practice, gating enhances the effective spatial resolution of reconstructed images by reduction of partial volume effects (PVE) due to motion blurring [64].

4.4.1 Cardiac gating

Cardiac gating is a well-known and widely used approach in conventional nuclear medicine imaging. Cardiac gating aims at eliminating artifacts induced by heart muscle (myocardium) which is a moving object undergoing repeating linear and rotational movements. It principle, motion-related inaccuracies can be compensated when the motion of the moving organ is periodic during the imaging. In general theory of the cardiac-gating, PET data stream, also known as list-mode (LM), acquired during the imaging session are sorted with respect to the certain time or phase of the cardiac cycle. Afterwards, all sorted list-mode data are gathered according to the time phase of the heart motion (end diastole (ED) and end systole

(ES) phases) and finally PET data are reconstructed with advanced computational techniques [244, 245].

There are two ways for triggering the imaging machine: retrospective gating and prospective gating. Retrospective gating is a method where the data being acquired using the constant rotation of X-ray beam (in CT) or detector (in PET) across the whole cardiac cycle and maximal tube current is at 65-85% of the R-R interval [246, 247]. Accordingly, the reconstruction of the multiple cardiac phases being prepared retrospectively. There are, however, two ways to reconstruct the data on retrospective gating scheme. The first technique constructs the acquired PET image data that are stored from a specific point (defined as the percentage of the cardiac cycle). The percentage of the cardiac cycle is defined as an absolute fixed time window in millisecond (ms) before or after the R-R interval [248]. The second technique which is better for the irregular heart rhythm is the reconstruction of the image data on different phases of the cardiac cycle. Therefore, the least motion phases of the heart are detected by choosing the best phase(s) of the cardiac cycle for each of the coronary arteries and their segments [248].

In practice, retrospective gating offers faster coverage than the prospective triggering for image reconstruction at every heartbeat. Additionally, for investigation of cardiac functionality and valve pathology, retrospective triggering has been advised more [246, 248]. On the other hand, the prospective gating is a technique that utilizes the forward-looking estimation of R-wave timing by the ECG signal in the diastole phase of the cardiac cycle [248]. With prospective gating, the X-ray beam is on for about 20% of the R-R interval (only a short portion of diastole phase) which is always after the QRS complex and it is turned off during the rest of the cardiac cycle. However, Qin and et al. (2011) reported that prospective ECG gating in comparison with retrospective ECG gating has identical image quality scores, while the patient radiation dose reduced by 76.50% during 320-detector CT coronary angiography [249]. FigureÂÍ4.3 shows visual concepts of retrospective and prospective cardiac gating.
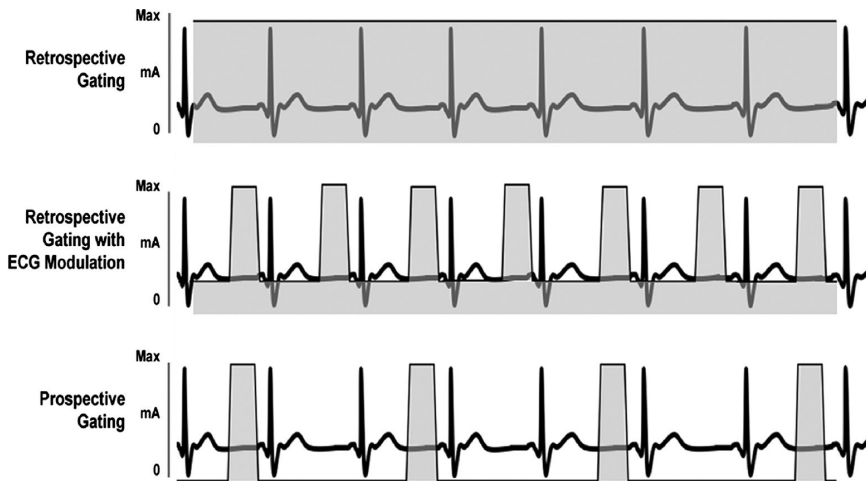

Figure 4.3: Overall schematic of retrospective and prospective triggering techniques (from [247] © Reprint with Permission).

4.4.2 Respiratory gating

Respiratory gating is synchronized acquisition of the image data based on respiratory phases. In practice, respiratory gating follows the same theory as cardiac gating but instead of cardiac movement a breathing trace is segmented and the input list mode stream is sorted accordingly for the image reconstruction. The breathing cycle is divided into distinct time-stamps (for example, peak exhale, mid inhale, peak inhale, mid exhale). Afterwards, list mode data are arranged into bins which are generated according to the phase or displacement of the respiration [238]. This technique is needed to remove motion artifacts that

cause poor attenuation correction and image blurring. In order to obtain synchronized emission acquisition based on the respiratory states of the subject, proper estimation of lungs motion is necessary [239]. There are two major respiratory gating techniques to estimate intrafraction variations, namely amplitude-based and phase-based (or time-based) respiratory gating. The amplitude-based gating relies on vertical segmentation of respiratory cycle — with either variable or equal gate width — with reference to the inspiration-expiration amplitude changes. The time-based/phase-based respiratory gating methods divide the breathing signal in horizontally with respect to timing information of events in each breathing cycle [250]. In PET imaging, respiratory gating events are aligned with the list-mode event during image reconstruction. Figure 4.4 illustrates amplitude- and phase-based gating and corresponding effects of respiration phases in cardiac PET Imaging.
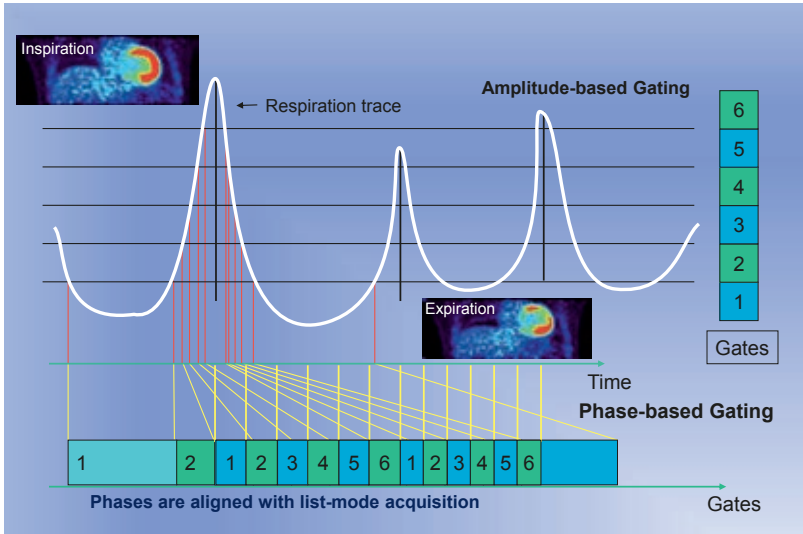

Figure 4.4: Principle of amplitude-based and phase-based respiratory gating schemes (sketched from [250, 251] with permission).

4.4.3   Dual gating

Dual gating is a novel technique that removes motion-related inaccuracies caused by respiratory and cardiac motions simultaneously. Dual gating improves spatial accuracy for the accurate imaging of small targets like vulnerable coronary plaques. This technique utilizes both cardiac and respiration traces that are sent periodically as independent triggers into PET (LM) data. By separating of dual gated LM data into sub-groups, each group includes certain physiological events from particular respiratory and cardiac phase [64].

4.4.4   MEMS Dual gating

MEMS dual gating is a novel gating approach solely based on joint miniaturized tri-axial MEMS accelerometer and gyroscope sensors. Multidimensional MEMS motion detectors offer comprehensive information related to the movement of the heart and lungs. Accordingly, SCG enables measuring translational chest motion changes — including low frequency displacements caused by lungs and high frequency accelerations due to the precordial vibrations. GCG, on the other hand, allows tracking rotational changes that originate from chest/upper body inclinations during breathing and precordial angular vibrations.

The main advantage of using MEMS dual method than other techniques is that joint SCG-GCG measurement offers simultaneous cardiac and respiration information originating from the mechanical operation of the internal organs. Although ECG is a perfect indicator of cardiac electrical activity, it does not give mechanical information regarding the mechanical status of the heart nor related to the internal organs motions. SCG and GCG together reveal supplementary information related to the mechanical functionality of the heart and lungs. Additionally, MEMS-based respiratory gating offers 6-axis chest motion traces to comprehensively delineate intrafraction movements, while impedance cardiography (e.g. ECG and bioimpedance measurements) and other currently available respiratory motion tracking technique yield only single position one-dimensional information on the movement of the chest/abdomen. Figure 4.5 shows the overall view of the dual gating for motion correction in PET imaging.
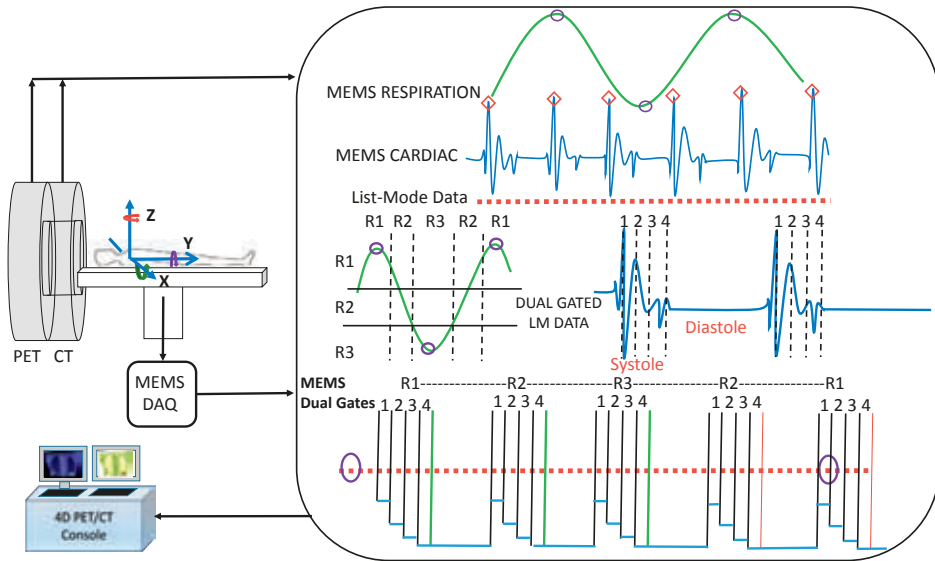

Figure 4.5: The principles of dual gating for PET/CT imaging (sketched from [64]).

Chapter 5

Aims of the Study

The original publications of this study had four specific aims:

I **Automatic delineation of multidimensional seismocardiography and gyrocardiography signals for heart monitoring applications**

To develop real-time and standalone heartbeat detection algorithms to delineate SCG and GCG signals by means of sensor fusion in three orthogonal axes, a Hilbert transform, adaptive thresholding and amplitude balancing, envelope detection and narrow-band filtering, and unsupervised learning. The main objective of algorithms development was to present an ECG-independent and fully-automatic approach that removes motion artefacts, selects the most high quality signal from rotational and translational axes, and subsequently proceeds in estimating true location of heartbeats (Study II and VII). The ultimate goal was ubiquitous cardiac monitoring by smartphone MCGs.

II **Characterization and analysis of gyrocardography signals, validating rotational cardiogenic waveforms, and annotating dominant GCG peaks and valleys using echocardiography**

To understand waveform characteristics of gyrocardiography signals from different rotational orientations and to analyze waveform stability with different gyroscope sensors. Several physiological parameters including heart rate, cardiac time intervals, moments of coinciding valvular events, and relative myocardial mechanical performance information were examined and validated using echocardiography studies (Study III). The main hypothesis is that rotational cardiogenic features obtained by GCG may lead to a reliable and robust home monitoring solution for early detection and prevention of cardiovascular diseases, specifically for heart arrhythmia and myocardial ischemia.

III **Improving PET imaging instrumentation by studying cardiorespiratory signals derived from MEMS motion detectors**

To explore the feasibility of a novel dual cardiac and respiratory gating approach, named MEMS dual gating, in PET imaging by validating acquired MEMS signals through echocardiographic observations, phantom radiopacity test, and subsequently real word cardiac PET study. The main hypothesis of this study is that multi-dimensional MEMS motion detectors could be used to estimate intrafraction organs movements and can enhance the quality of acquired PET/CT images (Study I and IV). Deterministic cardiac and respiratory motion segmentation algorithms were developed and tested (with respiration belt and optical tracking techniques) to delineate physiological status of internal organs such as the heart and lungs.

IV **Automated detection of cardiac abnormalities from smartphone seismo- and gyrocardiograms**
To improve the detection of cardiac abnormalities using state-of-art and automated classification algorithms consisting of various signal processing and machine learning techniques in two-class and multi-class settings. The ultimate goal was to explore the potential utility of a multinomial discrimination approach in detection of AFib, coronary artery diseases, and myocardial ischemia using only smartphone MCG recordings (Study V and VI).

Chapter 6

Materials and Methods

6.1 Data Acquisition and Clinical Protocols

6.1.1 Instrumentation of Electromechanical Monitoring

For the MCG measurements performed for this Ph.D. study, a preliminary custom-designed hand-held device was made for recording the electromechanical activity of the heart. This measurement system consisted of a multidimensional seismocardiography, gyrocardiography, and standard three lead electrocardiography. A miniaturized (3 mm $\times$ 3 mm $\times$ 1 mm), triple-axis, low-power, capacitive digital accelerometer (Freescale Semiconductor, MMA8451Q, Austin, TX, USA) and an (3 mm $\times$ 3 mm $\times$ 0.9 mm) ultra-accurate, low power, low noise, 3-axis angular rate sensor (Maxim Integrated, MAX21000, San Jose, CA, USA) were deployed for recovering precordial vibrations and respiratory motion signals. The inertial sensors assembled on printed circuit board were coated with a thin plastic cover to be attached to the skin of the chest anterior to the body of sternum bone using double-sided adhesive tape without hair removal in the chest area. The measured acceleration and angular velocity range of the accelerometer and gyroscope were set to $\pm 2g$ and ± 250dps, respectively. The accelerometer has an RMS noise of 99 μg/$\sqrt{Hz}$ and is tuned to have an output bandwidth of 400 Hz, while the gyroscope low noise density was 9 mdps/$\sqrt{Hz}$ and the output bandwidth was 400 Hz. The data acquisition also involved the measurement of a low power integrated analog front-end ECG (Texas Instruments ADS1293) using Freescale FRDM-KL25Z board to collect synchronized data on a memory card with a sampling frequency (Fs) of 800 Hz. The chosen rate of sampling is potentially beneficial in order to investigate higher frequency (up to 320 Hz) intracardiac events such as heart valvular activity and murmurs [252]. However, a lower sampling frequency would generally result in smaller power consumption and computational complexity. Standard ECG electrode positioning is followed by mounting two electrodes on the right and left upper chest area and two on the anterior lateral regions to the abdomen on the left and the right hypochondriac.

A multi-modal, wireless, battery-powered, wearable system architecture with the possibility to control with a smartphone was later designed to facilitate data acquisition in biomedical research. The new architecture consisted of a Bosch Sensortec BMI160 IMU including a 3-axis accelerometer and gyroscope in a single package with a sampling frequency of 200 Hz, an output bandwidth of 80 Hz and 74.6 Hz, and noise density of 180 μg/$\sqrt{Hz}$ (1.6 mg$_{rms}$) and 8 mdps/$\sqrt{Hz}$ (1.5 mdps$_{rms}$), respectively, Texas Instruments ADS1293 analog front-end ECG (Fs= 267 Hz), Nordic Semiconductor nRF51822 (32-bit ARM Cortex MO-based μC with Bluetooth (BLE) radio) microcontroller, and an external microSD memory card connected to microcontroller for data collection. Figure 6.1 shows the two versions of data acquisition systems developed for biomedical research specifically for wearable MCG [253].

For smartphone mechanocardiography, built-in IMU including micro-sized accelerometer and gyroscope sensors (both with three data axes) is used to obtain SCG and GCG recordings with a sampling frequency of 200 Hz. A dedicated Android application (app) was first developed to store the raw data
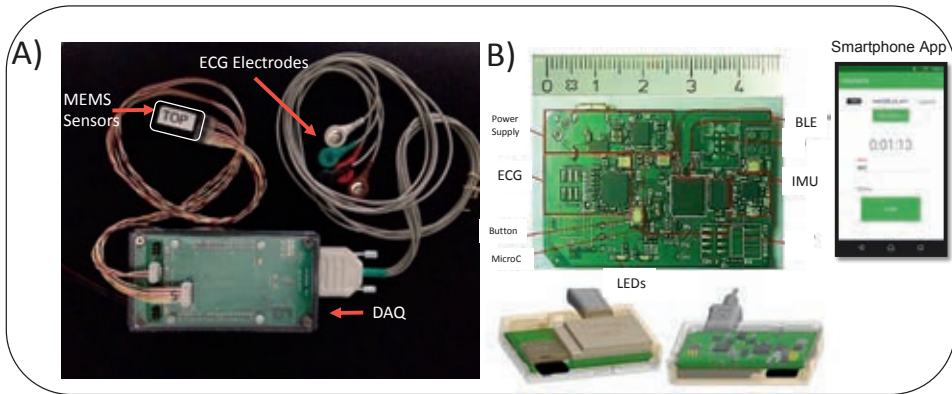
36

Figure 6.1: **Figure A** represents overall view of first generation data acquisition system designed for ECG and MEMS accelerometer and gyroscope measurements. **Figure B** shows the new architecture including IMU sensor, ECG, BLE antenna, and core CPU. An Android App was used as remote controller for this device [from [253] © IEEE reprint with permission].

(in a text format) on the internal memory of the phones. The app was later improved to perform on-board or remote computations for heart monitoring and arrhythmia classification. Data processing can be performed either onboard — by currently implemented algorithms in the app — or off-line — by transferring the data from the phone's memory card to a desktop computer or via a Cloud computing server for development purposes. All signal processing and data analyses tasks were made off-line in the Matlab (R2015a) programming environment.

6.1.2 Echocardiographic Setup and Examinations

The echocardiography examinations in this thesis were conducted by a Vivid E95 scanner with a 1.4-4.6 MHz transducer (GE Healthcare, Finland). A complete echocardiographic study was carried out using conventional apical views for 3 to 6 cardiac cycles. EchoPAC post-processing software (Version 113, GE Healthcare, Finland) was deployed for off-line echocardiographic analysis of TDI and 3D speckle tracking strain. Standard echocardiography, ECG, and 3-axis GCG and 3-axis SCG were performed concurrently. Figure 6.2 demonstrates the diagram of the data acquisition set up for cardiac MCG (A) and ultrasound examinations (B).

For measurement of cardiac time intervals, mitral valve and aortic valve flow velocities were recorded using pulsed-wave (PW) Doppler. For measurement of myocardial velocities, apical 4 chamber TDI images were obtained with an average rate of 106 frames per second. Speckle tracking, which is an automated functional imaging technique for multidimensional deformation or strain analysis, was performed. 3D volume covering the whole left ventricle myocardium was obtained from an apical view averaging 6 cardiac cycles with an average rate of 40 frames per second for 3D speckle tracking strain analysis. The results of 18 myocardial segments were averaged to obtain global strain in longitudinal, circumferential, area, and radial directions. In addition to curves, numerical strain and timing data from each frame were obtained.

6.1.3 PET/CT Imaging and Clinical Protocols

Clinical PET imaging investigations, after primary proof-of-concept studies [224, 226], were performed using 18F-fluorodeoxyglucose as a tracer. 120 minutes after [18F]-FDG (∼300 MBq) injection, dual-gated PET data acquisition was performed according to the protocol described in the following.
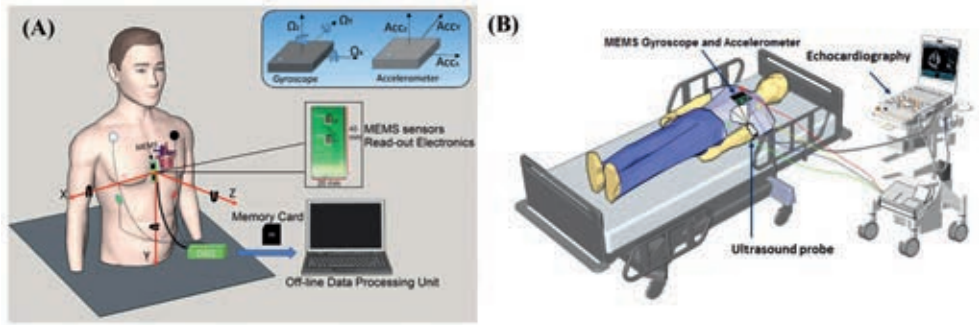
Figure 6.2: **Figure A** represents overall simultaneous data acquisition from ECG and MEMS accelerometer and gyroscope sensors. **Figure B** shows general schematics for MCG validation study including MEMS sensors, ECG, blood pressure, and echocardiography measurements [from [163] © Reprint with permission] .

Clinical patients with a history of heart disease underwent contrast-enhanced coronary CT angiography (CTA) using the standard prospective ECG gated low dose CTA protocol with 50-100 ml of contrast agent (3.5 ml/s) and concurrent acquisition of 64 parallel slices. Patients were asked to keep their arms raised above the head by a supporting foam cushion to avoid truncation artifacts. After termination of the CTA study, a 3D PET scan of the upper chest area including cardiac muscle was obtained in list-mode with ECG and respiratory gating (RPM from Varian Medical Systems, Palo Alto, USA) with an acquisition time of 24 minutes. The PET/CT scan is performed with Discovery D690 PET/CT scanner (GE Medical Systems, Milwaukee, WI, USA). The considered PET/CT system has an axial and transaxial FOV of 157 mm and 700 mm and contains a 64-slice CT. CTAC and CINE CT were obtained by using a low-dose CT with a tube voltage of 120 keV. Figure 6.3 illustrates cardiac imaging validation set up with concurrent RPM, ECG, and MEMS cardiac and respiration signals recorded along with the PET scan.
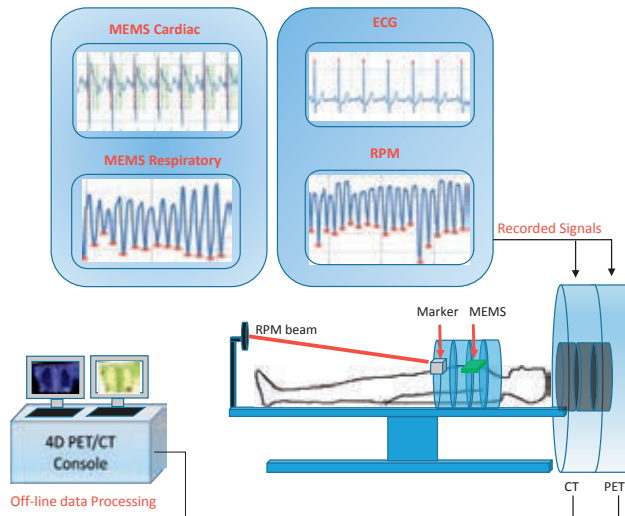

Figure 6.3: General schematic of PET/CT for clinical cardiac imaging including active RPM and ECG streaming, as well as simultaneous MEMS cardiac and respiration signal recording.

6.2 Biomedical Signal Processing

6.2.1 Signal Preprocessing and Filtering Techniques

Automated motion artifact removal

Motion artefact is a very common problem in analyzing of MCG signals. Several different methods have been suggested for removing motion related distortions in the MCG signals [17, 173–175, 196, 254, 255]. However, none of the suggested methods could ultimately overcome this challenge and it is still an open issue in processing of MCG signals. In this work, two automated motion artifact removal algorithms were developed to discard disturbing components perceptible in the MCG signals (i.e. body motion artifacts in each axis of the gyroscope and accelerometer) as follows:

Method I: To identify distorting elements from the original MCG signals, a power envelope of the signal (independently for each channel) was computed using the root mean square (RMS) operation. A sliding window with the length of 500 ms and a detection threshold of twice the median value of the power envelope are determined to search for the disturbing elements of the signals. With this approach, parts of the signal where the power envelope exceeds the determined threshold are automatically classified as motion artifacts and therefore are discarded.

Method II: The motion artefacts are removed from the selected signals by dividing the signal into 10 s epochs. A single sided FFT is computed for each epoch and the resulting spectra are smoothed with a moving average filter of ten samples. The amplitudes within the pass-band frequency range are integrated for each epoch spectra. Epochs with a value more than 125 % of the median value are removed. After each segment removal, the median value is updated yielding always comparable removal threshold independent on the original signal quality

Figure 6.4 briefly illustrates the process of the motion artifact detection on a typical noisy signal using both methods. Figure 6.4 (A) shows the envelope of the signal power, where the signal components exceeding the threshold (dashed line) are highlighted by red color. In Figure 6.4 (B), parts in which classified as motion artifact in the original MCG signal are detected (highlighted by red color), and can be discarded. With Method I, eleven motion-artifact free segments, marked with numbers and green color dashed vertical lines, are detected. Figure 6.4 (C) and (D) show motion artifact removal using the second method in both SCG and GCG signals.
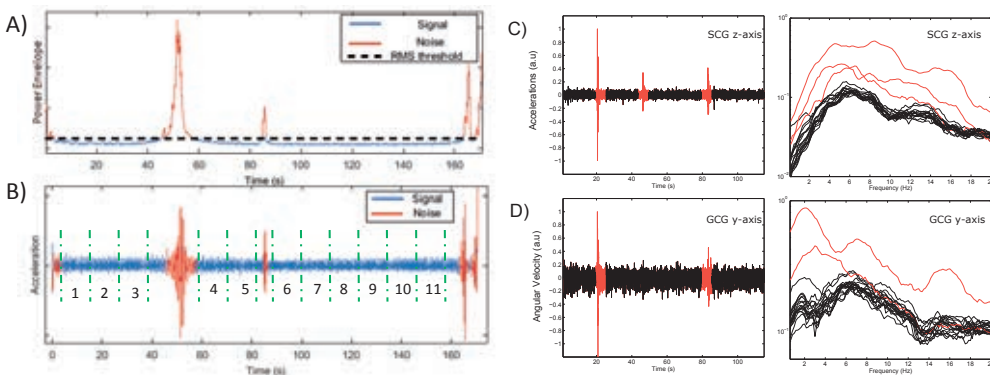

Figure 6.4: Detection of motion artifacts from MEMS motion signals. **Figure A** shows the first method where a filtered signal in which noisy components exceeding the RMS threshold are highlighted. **Figure B** demonstrates detected motion artifacts throughout the original signal. **Figure C and D** show motion artifact removal using spectral analysis in SCG and GCG.

Frequency analysis and bandpass filtering

Frequency contents of the recorded SCG and GCG signals are analysed using fast Fourier transform (FFT) approach. Figure 6.5 demonstrates the result of the FFT analysis by plotting power spectral density of the signals from all channels of accelerometer and gyroscope sensors. As it can be seen, most of the frequency components and signal energy are accumulated in the range of 0.1-50 Hz. However, the spectrum of GCG shows energy concentration in the frequency band 0.1-30 Hz while for the SCG a wider spectral band between 0.1 and 40 Hz is visible. On the basis of this rough frequency analysis, two band-pass filters, one based on FFT and one based on Butterworth IIR (infinite impulse response) are designed. Different cut-off frequencies are examined for GCG and SCG signals and after extensive studies on the time-frequency analysis of the signals, cut-off frequencies of 1-20 Hz and 4-40Hz are found to be a good compromise for the GCG and SCG, respectively, for maximal noise reduction while preserving the morphology of the signal close to the original. Thereby, biosignals recorded in the course of this study are pre-processed with either an FFT filter or a 3dB bandpass 4th order Butterworth IIR filter to eliminate baseline wandering and noise components. Electrical signals obtained via ECG recordings are also filtered with the cut-off frequencies of 1-49 Hz.

Single spectrum analysis filter

Conventional frequency domain filters generally require setting the pass-band frequency limits according to the characteristics of the frequency contents of the biosignals and may occasionally cause loss of vital information that can lead to morphological changes as well as amplitude attenuation [256]. In this work, another filtering approach is considered that is based on decomposing the signal into its favorable and unwanted components. Singular spectrum analysis (SSA) is an algorithm of time series analysis as it offers the capability of decomposing the signal into principal components (PCs) — by choosing a subset of eigenelements — in order to reduce noise, remove baseline wander, and identify oscillatory components [257]. SSA filter consists of two complementary stages: decomposition and reconstruction [258]. Decomposition stage includes two steps, i) embedding the original time series of length N into a sequence of lagged vectors of size L by forming $K = N - L + 1$ principal components, where L is the window length (1<L<N), and creating a trajectory matrix A (Hankel matrix), and ii) singular value decomposition (SVD) of the trajectory matrix A by setting $S = AA^T$ and delivering it as a sum of rank-one bi-orthogonal elementary matrices. Reconstruction stage consists of two steps as well: i) eigentriple grouping by splitting the elementary matrices A_i into m disjoint subsets $I_1, ..., I_m$ and summing the matrices within each group, and ii) diagonal averaging by transforming each matrix A_I of the grouped decomposition into a new series of length N.

In the context of smartphone MCG signal processing, for the SCG-GCGs with a sampling frequency of 200 Hz, it was empirically established that a windowing length L up to 10-15 ms is suitable for decomposing signal and the first three PCs are best noiseless components to be reconstructed. This reconstructed component, which is assumed to be noiseless while leaving out redundant and other irrelevant information, is therefore employed for further signal analysis tasks. Figure 6.6 shows that the morphological characteristics of mechanical activation complexes, heartbeats, differ from no-filtering status to SSA-filtering in all axes of MEMS signals in a selected noisy signal (an AFib case with present HF) for demonstration purposes.

6.2.2 Hilbert Adaptive Beat Identification Technique

The Hilbert transform is a popular operation for detecting the QRS complexes in ECG signals, and a considerable amount of literature has been published on this topic [259–262]. Being based on Hilbert transform, the detection of heartbeats is improved as the envelope of the signal coordinates proper detection of the dominant peaks — namely cardiac impulses — across the signal. In this thesis, the capability of the Hilbert transform for locating heartbeats in SCG and GCG (or generally MCG) signals is assessed through a new approach named Hilbert adaptive beat identification technique (HABIT) for
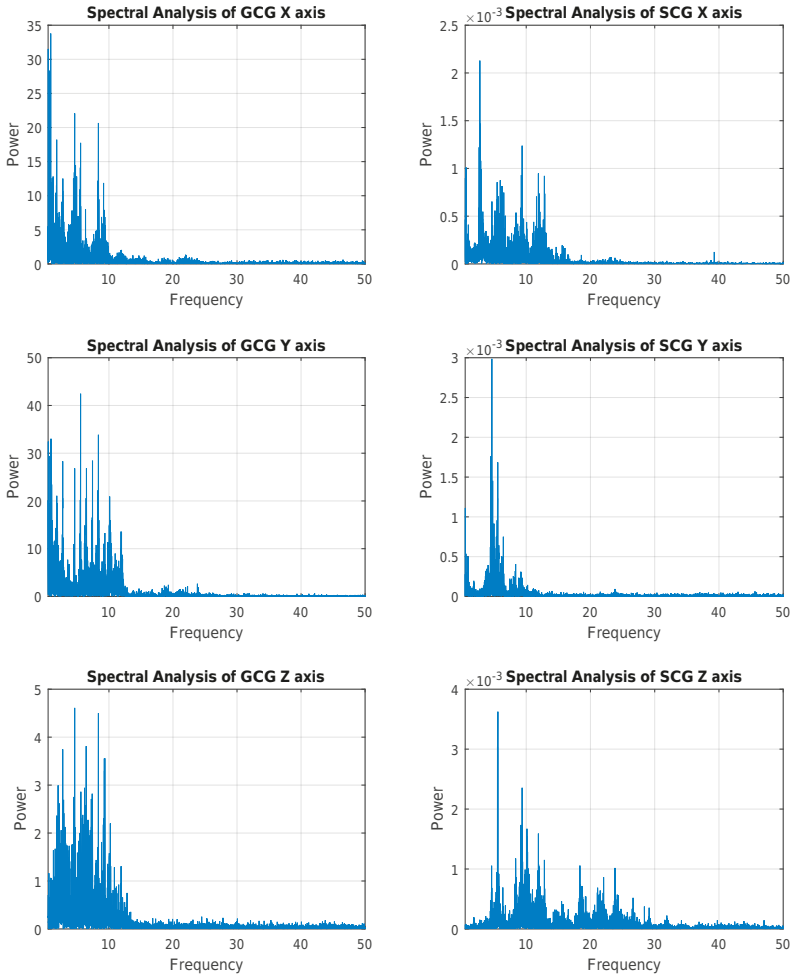
Figure 6.5: Spectral analysis of SCG and GCG signals

the accurate detection of aortic valve opening timings, interbeat time intervals, and HRV estimation in MCGs [163, 263].

The HABIT method includes a preprocessing step where a 4th order Butterworth IIR filter with band-pass frequencies of 1-20 Hz and 1-45 Hz is respectively applied on all gyroscopic and accelerometeric channels, allowing the removal of baseline wander and noise. Afterwards, the total acceleration and angular velocity magnitude signals denoted respectively by $s(t)$ and $g(t)$ are defined as :

$$s(t) = \sqrt{\text{AccX}(t)^2 + \text{AccY}(t)^2 + \text{AccZ}(t)^2} \tag{6.1}$$

$$g(t) = \sqrt{\text{GyroX}(t)^2 + \text{GyroY}(t)^2 + \text{GyroZ}(t)^2} \tag{6.2}$$

where AccX, AccY and AccZ are the axes of linear accelerations and GyroX, GyroY, and GyroZ are the axes of angular velocity. The axes of translational and rotational precordial vibrations in this dissertation are defined as follows: the x-axis points laterally from left to right (sinistero-dexter), the y-axis points from head to foot (superior inferior), and the z-axis points from back to front (dorso-ventral). These axes are illustrated previously in the Fig. 6.2 (A).
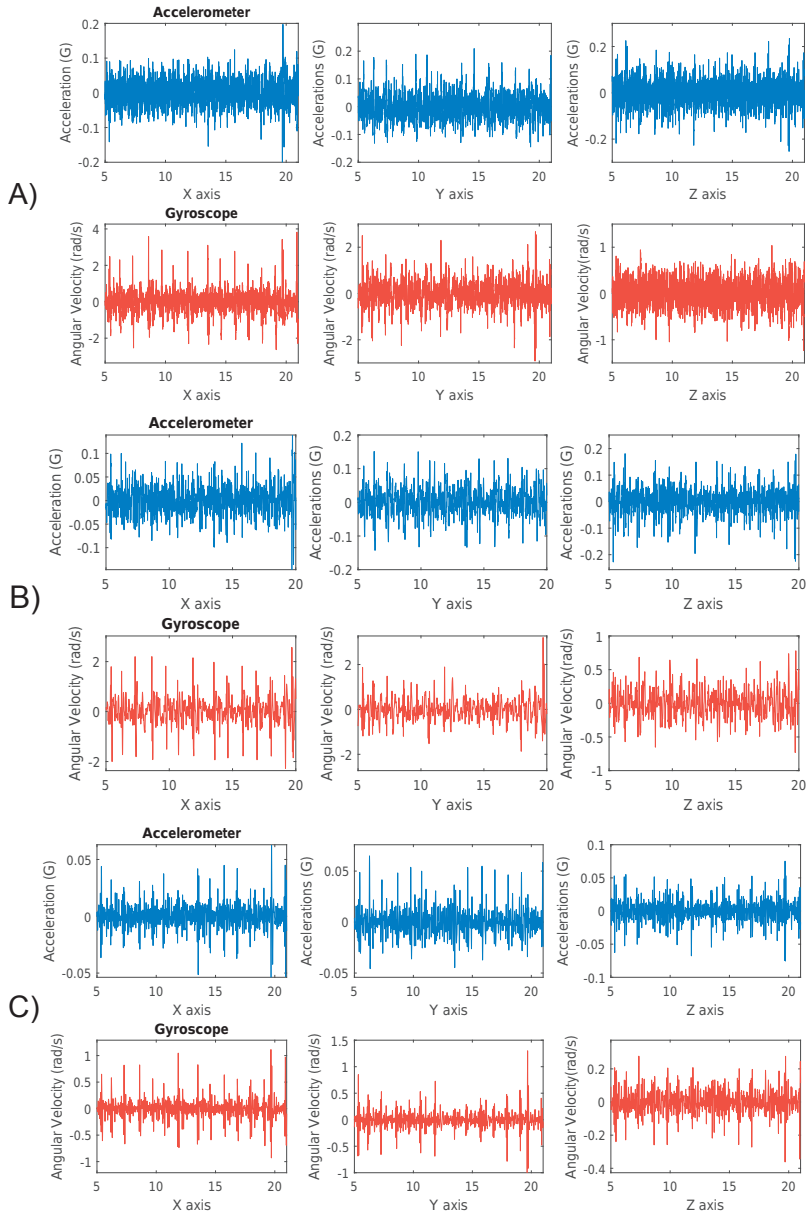
41

Figure 6.6: Typical AFib (with present HF) signal derived from smartphone MCG without filtering (**A**), with band-pass filter (**B**), and SSA filter (**C**).

The total magnitude of acceleration/rotation signals are then fed to the Hilbert transform in order to derive the envelope of the combined SCG and GCG signals. Hilbert transform of a real signal $f(t)$ can be defined as:

$$\hat{h}(t) = \frac{1}{\pi} \int_{-\infty}^{+\infty} \frac{f(\tau)}{t - \tau} d\tau \tag{6.3}$$

where $\hat{h}(t)$ is a Hilbert transform of $f(t)$ signal returning a complex helical sequence named analytic

signal. The analytic signal for a series of real-valued finite energy signal has a one-sided Fourier transform meaning that negative frequencies are vanished. Hilbert calculates the FFT of the input sequence, replaces those FFT coefficients that correspond to negative frequencies with zeros, and calculates the inverse FFT of the result [264]. Afterwards, the envelope of SCG-GCG signals is extracted as the amplitude of the analytic signal:

$$A(n) = |h_a(n)| = \sqrt{h^2(n) + \hat{h}^2(n)} \tag{6.4}$$

where $h_a(n)$ is an analytic signal. The envelope signals — which are here denoted by $A(n)$ and $\acute{A}(n)$ for SCG and GCG signals, respectively — are filtered by a previously described brick-wall band-pass FFT filter with cut-off frequencies of 0.5-3 Hz (corresponding to 30 and 180 beats per minute) to extract cardiac pulsatile waveforms over SCG/GCG signals. Subsequently, the $SCG_a(n)$ and $GCG_a(n)$ signals, representing filtered envelopes of SCG and GCG signals, respectively, are linearly summed to achieve a very low-frequency approximation of the heart motion signal, $P(n)$, which is called the *principal signal* in this work.

$$P(n) = SCG_a(n) + GCG_a(n). \tag{6.5}$$

After converting multiaxial cardiac motion signals into a single axis signal, a successive mean quantization transform (SMQT) [265] is applied to dynamically balance the achieved *principal signal* or $P(n)$. One dimensional SMQT allows improving the signal quality dynamically by removing the gain and bias of the signal. Finally, a refinement process — based on adaptive thresholding suggested by Pan-Tompkins method [266] — is deployed for accurate estimation of heartbeat location on SCG/GCG signals. With the refinement process we localize the exact position of heart pulses in the original filtered SCG-GCG signals (typically z-axis of SCG and y-axis of GCG) through estimating of fiducial markers (local maxima) in the *principal signal*. Figure 6.7 shows the overall process of adaptive heartbeat detection using HABIT method in SCG/GCG signals.
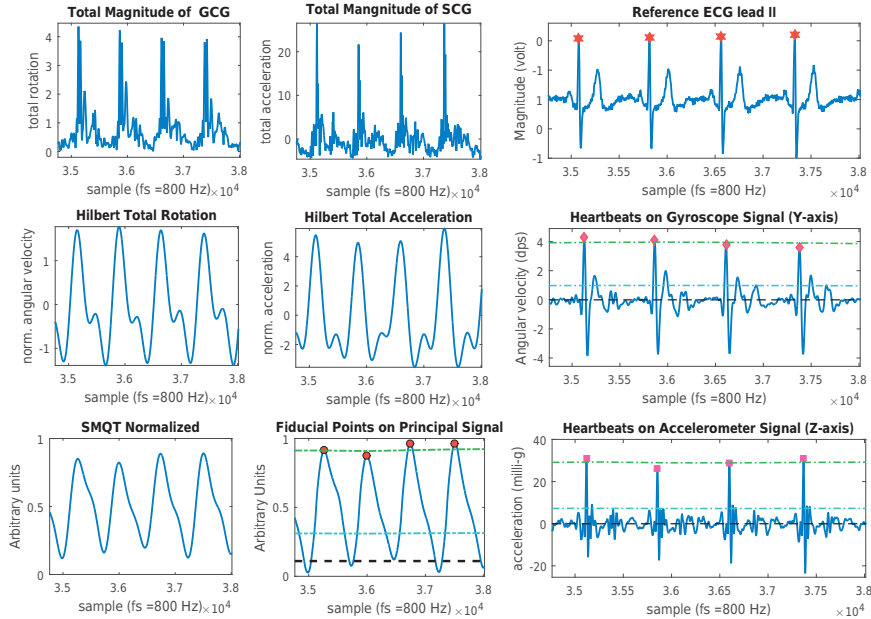

Figure 6.7: Adaptive heartbeat detection on SCG-GCG signals using HABIT method. Green color dashed line shows the signal level, blue color dashed line refers to adaptive threshold, and black color dashed line reflects noise level in the SCG-GCG signals (from [263] © Reprint with permission).

6.2.3 Automated Unsupervised Heartbeat Detection

One limitation of HABIT and similar methods is the manual selection of the sensor channels where the heartbeat detection is taken place. Another standalone heartbeat detection algorithm with the capability to autonomously select the best/high quality cardiac sensing channel from IMU sensors was therefore developed to tackle this limitation. This new approach automatically selects the best performing SCG/GCG channel by finding the vibrating axis that has the highest peak-to-peak amplitude (S) divided with absolute median deviation. The selection process is based on rough signal-to-noise ratio estimation as

$$SNR_{axis} = \max_{ax \in \{x,y,z\}} \{S/N\}_n \tag{6.6}$$

where S is the median absolute difference of local maximums and minimums that are separated at minimum 1 sec, N is considered to be noise defined as frequency components over 50 Hz (obtained by filtering the signal with a third order Butterworth high pass filter with 50 Hz cut-off frequency), ax is the selected axis/channel in IMU sensor. This gives the signal-to-noise ratio and the highest ratio is considered to select the best axis (SNR_{axis}) for further processing. This selection is performed independently to both tri-axial SCG and GCG. After selecting the best SCG and GCG axes, a pre-processing step including bandpass filtering (for noise and baseline wandering elimination) and motion artifact removal was applied on all three channels of MEMS sensors (in total 6 channels) — using an iterative frequency spectrum analysis over the signals and removing high energy parts of the signal as described in Section 6.2.1.

The heartbeat detection part consists of two peak detection sub-algorithms, namely wavelet enhancement and clustering, for both accelerometer and gyroscope signals. In general, four peak candidate streams, each having their own independent candidates (two SCG and two GCG candidates), are combined to estimate the exact location of heart beats. Figure 6.8 shows the main framework of the algorithm.
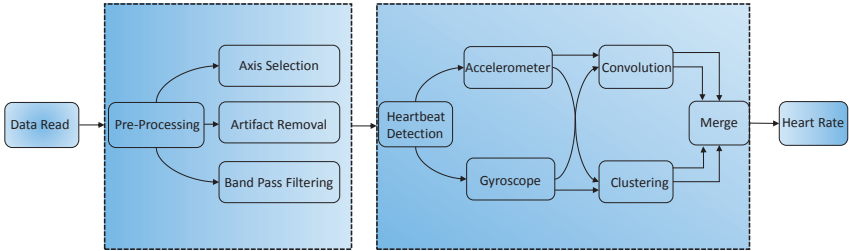

Figure 6.8: A block diagram of the unsupervised multidimensional beat detection approach based on data fusion and clustering.

The wavelet enhancement method utilizes a narrow band filtering as described in [185]. This process is based on two steps: i) sample-wise squaring to enhance peak amplitudes, and ii) convolving the signal with Gaussian shaped template window of 800 ms. From the resulting filtered signal the candidate peaks are detected using an automatic multiscale peak detection (AMPD) [267].

An unsupervised k-means clustering is also considered as a complementary beat detection method. Therefore, all local maxima and minima points in SCG/GCG are detected from the pre-processed signal. The considered features for the k-means clustering are the amplitudes of successive maxima and minima points on SCG/GCG signals, determined as f_a and f_g for accelerometer and gyroscope signals respectively,

$$\mathbf{f}_a = (max_i, min_i, max_{i+1}, min_{i+1}), \tag{6.7}$$

$$\mathbf{f}_g = (max_i, min_i, max_{i+1}). \tag{6.8}$$

where i is the position of the ith local maxima/minima.

The selected distance measure is the euclidean norm. The correct cluster is recognized by finding the cluster with highest average peak amplitude. These four candidates (two accelerometric and gyroscopic heartbeat positions detected by two different methods) are merged into one stream in order to estimate the heartbeat locations [173]. Briefly, the detected peak candidates in each stream will pair/assign to no more than one other candidate in each of the three other streams. Each candidate will assign to the closest one to its own location and if no suitable pairing candidate is found within 330 ms window no pairing occurs. The final location is determined by the average location of identified pairs. Figure 6.9 shows the overall performance of the presented framework for heartbeat detection in SCG-GCG signals.
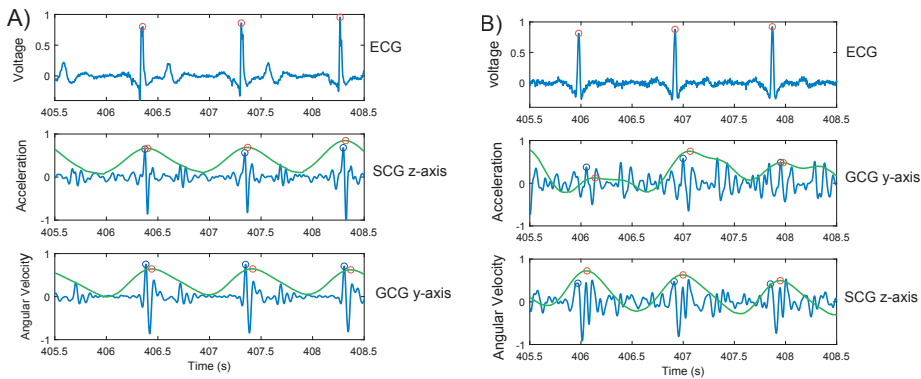

Figure 6.9: An example of heartbeat detection using wavelet-clustering method for a healthy subject **(A)** and CAD disease patient **(B)**. Heartbeats in both SCG z-axis and GCG y-axis are found through clustering (blue circles in the original blue color signal trace) and wavelet filtered signals (red circles in the green color trace).

6.2.4   Methods for Cardiac Quiescence Phase Prediction

Cardiac cycle segmentation includes identifying fiducial points and subsequently estimation of the cardiac time intervals, that is systolic and diastolic periods. In the first study, a deterministic approach mainly based on identifying cardiac activity markers in ECG and SCG signals as well as distinct windowing roles are reported. The method was originally proposed for mechanical cardiac gating (dividing SCG signals into a certain number of bins) purposes. Cardiac segmentation in MCG signals is a challenging task due to inter- and intrapersonal variations. Several different studies have reported state-of-art algorithms for automated cardiac cycle segmentation in SCGs [159–162]. Echocardiogrphyic observations in Study IV showed that signals derived from MEMS sensors can indicate dominant phases of cardiac cycles specifically the cardiac relaxation phase (diastasis) where myocardial motion is in its minimum level. Accurate detection of this cardiac quiescent phase within the cardiac cycles in MCG signal is advantageous for cardiac gating purposes.

One major motivation of this doctoral study was to employ suitable solutions including novel sensor fusions as well as signal processing techniques for cardiac and respiratory cycle segmentation. The segmentation process in MCG signals aims at accurate separation of the two fiducial points from the joint GCG and SCG signals. The systolic contraction complex (AVO point) and the diastolic ∧- wave peaks (AVC/MVO point) are well-defined locations that are constantly visible in the GCG and SCG signals (as shown in Figure 3.5). These timing points, as validated by echocardiography inspections, coincide with the opening and closure moments of the heart valves [143, 163]. Accordingly, by estimating ventricular systolic and diastolic cardiac events it is feasible to accurately estimate cardiac mechanical activation and relaxation episodes.

Deterministic segmentation process in this study includes a search window W1 defined from the onset of AO-peak in MCG signals to the onset of the following heartbeat. Within this search window, a local maxima is searched which typically appears in the early diastolic phase. With dividing cardiac cycle into two parts, that is P1 and P2, systolic and diastolic cardiac time intervals are roughly estimated. P1 begins from the point of AO peak to the mid diastolic ∧- wave and P2 is defined from ending moments of P1 to the onset of the following heartbeat.

For prospective cardiac gating applications, each sub-segment can be divided into a certain number of bins depending on the purpose of imaging examination. For instance, a 3 bin cardiac gating scheme will include two systolic bins within P1, where a short cardiac semi-quiescence is expected, and one large diastolic bin P2, where full cardiac relaxation/quiescence takes place. Figure 6.10 shows the cardiac cycle segmentation process in GCG and SCG using the above described windowing technique. Moreover, this figure shows multi-dimensional views (ensemble averaged) of the cardiac cycles with corresponding segmented systolic-diastolic phases.
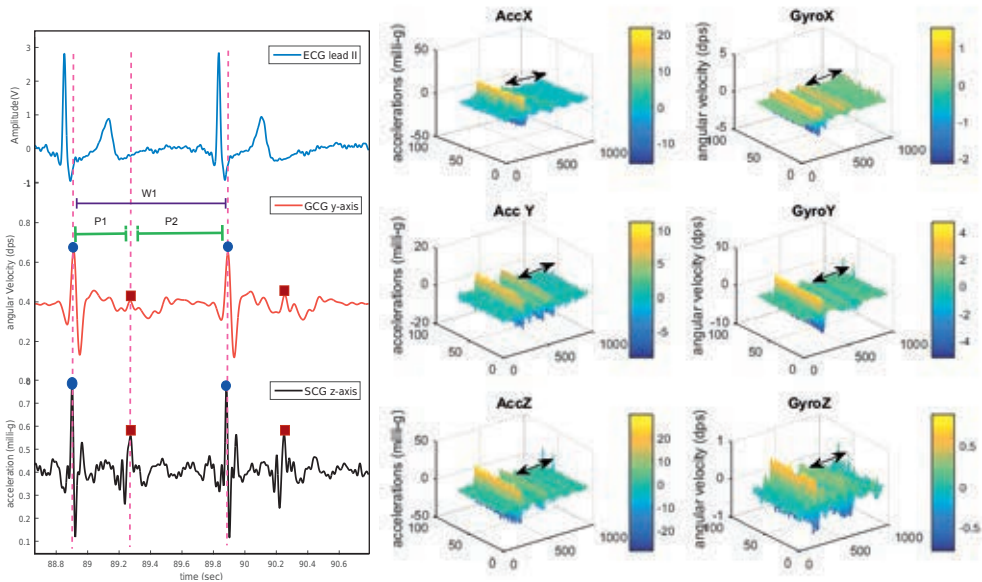

Figure 6.10: Cardiac segmentation process in SCG and GCG signals (left) and six-axis view of the cardiac signals with corresponding roughly estimated mechanical relaxation phases (right).

6.2.5 Chest Motion Decomposition with MEMS

Chest motion signals derived from inertial sensors consist of low frequency and high frequency components. The high frequency components generally fall between 2-45 Hz and reflect the precordial micro-vibrations, while signals within the frequency bands less than 2 Hz reflect chest's longitudinal motion [178]. These low frequency chest motion components are induced by breathing action and can be separated from precordial high frequency movements using a respiration signal extractor (RSE) algorithm. Tri-axial motion sensing using joint inertial sensors allows comprehensive chest movement analysis in different orientations (6DoF) as angular and translational movements can be tracked. For the purpose of respiratory gating in PET imaging, this multidimensional motion sensing may help in better estimation of intrafraction organ movements, e.g. heart-lungs coupled motions. To this end, this study introduces algorithms yielding accelerometric- and gyroscopic-derived respiration signals — denoted by ADR and GDR — and segmentation processes to estimate quiescent respiratory periods suitable for amplitude- or phased-based respiratory gating.

The RSE algorithm developed in the context of this Ph.D. work decomposes low frequency components from the raw accelerometer and gyroscope signals. With the gyroscopic signals, an integration process (resulting in a type of low-pass filtering) is considered in order to derive chest inclinations or the angle of rotation (tilt). This process is similarly performed with accelerometers in order to calculate angles of rotation, for example, pitch around x-axis and roll around y-axis, as shown in Figure 6.11. Unlike gyroscopes, accelerometer sensors are not able to measure yaw which is rotation around z-axis.
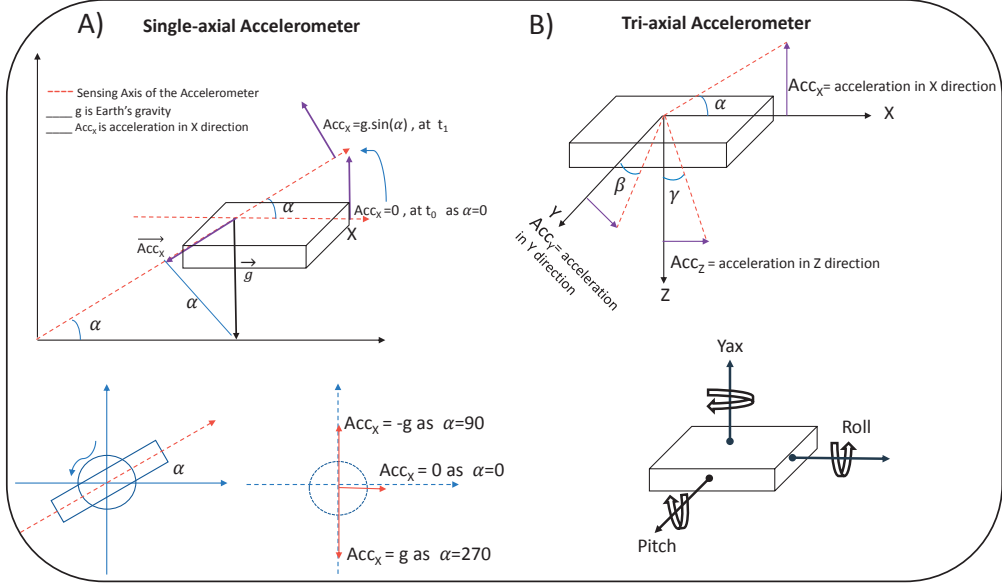

Figure 6.11: Angle measurement using single (A) and multidimensional (B) accelerometer sensor for tracking respiratory induced chest inclination.

As shown in Figure 6.11 (A), a single axis accelerometer sensor can sense angular displacement around x-axis, α, as acceleration Acc_x in this direction depends on gravity change along with angular displacement. Therefore

$$\alpha = \arcsin(\frac{AccX}{g}). \tag{6.9}$$

With a multidimensional sensor inclination around x-axis (pitch) is dependent on the total magnitude of gravity with z- and y-axes while the the angular position of the sensor alters with α.

$$Pitch = \arctan(\frac{AccX}{\sqrt{AccZ^2 + AccY^2}}). \tag{6.10}$$

Similarly, rotation around Y axis (roll) depends on total magnitude of gravity with z and x-axes while accelerometer tilts with an angle of β

$$Roll = \arctan(\frac{AccY}{\sqrt{AccZ^2 + AccX^2}}). \tag{6.11}$$

In continuation to angle calculation, a brick-wall band-pass filter with the frequency bands of 0.1-2 Hz is applied on the SCG-GCG signals in order to discard high frequency components of the signals. Finally, their amplitude is balanced dynamically using SMQT approach [265]. Figure 6.12 shows respiration signals extracted MEMS signals and alignment between the respiration signals and end-expiration peaks identified in RPM, ADR, and GDR.
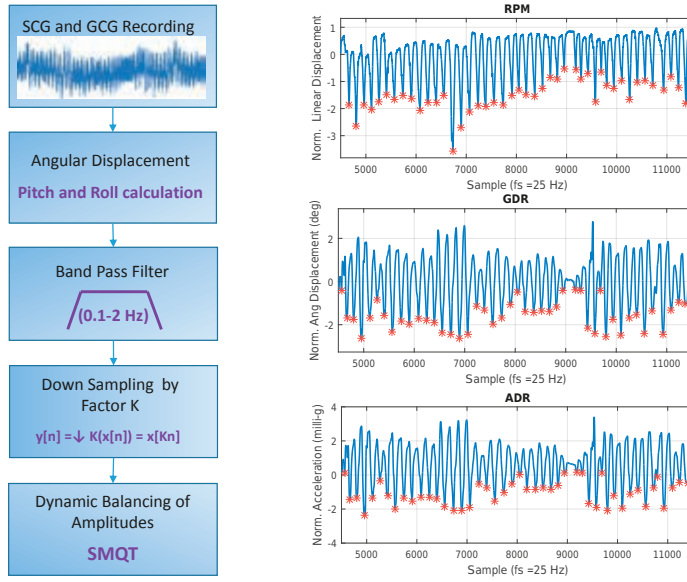
Figure 6.12: Flowchart of respiration signal extractor algorithm (left) and resulting MEMS GDR and ADR signals follow reference RPM with high correlation (right).

Unlike z-axis, the x- and y-axes of accelerometer sensor are able to show respiratory inclinations as their coordination position on the chest is changed by the chest micro-scale rotation/inclination. In contrast, accelerations measured in the z-axis pose stronger precordial vibrations than the other axes. Even though it is possible to measure breathing signals with for example gyroscopes, the main motivation to use accelerometers for wearable/implantable devices is lower power consumption. Low power consumption is crucial when considering wearable/implantable wireless devices. The total power density of an electrical in vivo device should not exceed $800\mu W/mm^2$ [268]. Current ultralow power MEMS accelerometers can easily meet this power density requirement, and it is expected that gyroscopes will achieve this limit within a couple of years. Currently typical power density values for MEMS gyroscopes are in the order of $1mW/mm^2$ and application specific optimization of the gyroscope can further decrease the power density. Moreover, the use of gyroscope, jointly with accelerometers, may effectively contribute on better estimation of intrafraction motion due to internal organ movements. Therefore, the utilizing of the multi-axial MEMS sensors is advantageous for the simultaneous extraction of the cardiovascular and respiration signals.

6.3 Automated Detection of Heart Arrhythmia and Ischaemia

6.3.1 Knowledge-Based Learning for AFib Detection

Timely diagnosis of AFib is crucial to prevent cardioembolic strokes. Automated real-time detection of heart arrhythmia such as AFib has been widely accomplished by searching abnormalities in the ECG signal as described in Section 2.2.3. The automated detection of AFib using cardiac mechanical motion has not been addressed in many research papers. However, one such example is [127], where a bed-mounted sensor was used to detect cardiac arrhythmia using BCG unobtrusively. New interest in this study is based on chest-mounted wearable/mobile MCGs where typical behaviour for AFib in the SCG-GCG signals are characterized and analysed using knowledge-based and machine learning solutions.

Knowledge-based AFib detection algorithms for MCG signal processing relies on irregularities on

both the timing and strength of heartbeats during arrhythmia. For example, Figure 6.13 (A) shows that cardiac mechanical activity during normal sinus rhythm is characterized by relatively constant timing and amplitude variations, while during AFib an abnormal and fully random behaviour is visible in MCG signals indicating irregular variations on timing of heartbeats, as well as random variation on the strength of the LV mechanical action (cardiac impulses). Primary investigations on the behaviour of MCG signals during cardiac normal and arrhythmic operations revealed that via studying the autocorrelation of the timing and/or instantaneous amplitudes of heartbeats measured using mechanical sensors it is feasible to detect cardiac abnormalities such as AFib [269]. Autocorrelation is a useful tool to measure the periodicity of a physical phenomena. With autocorrelation it is possible to investigate the periodic characteristics of a biosignal. For example, Figure 6.13 (B) shows a sinus rhythm MCG signal, with a relatively stationary condition, and correspondingly a periodic behaviour can be seen in its autocorrelation plot, but AFib is a random phenomenon and therefore no clear sign of regularity can be seen in the autocorrelation measurements.
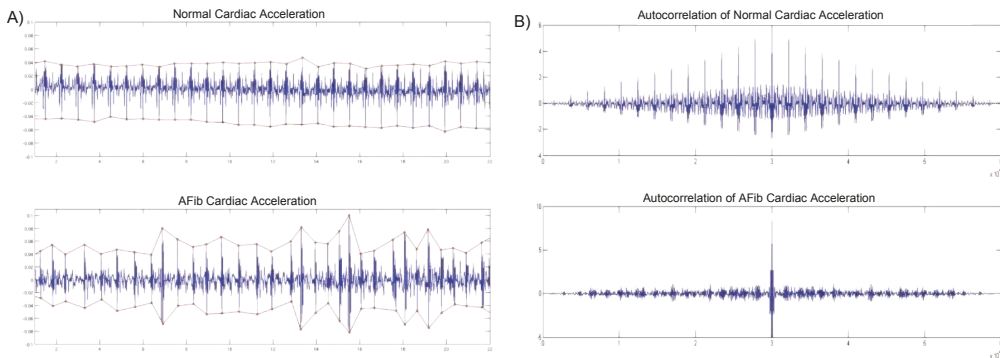

Figure 6.13: **Figure A** shows timing variation and amplitude behaviour during sinus rhythm and AFib mode. **Figure B** presents the autocorrelation of the SCG measurements in the corresponding modes.

In addition to autocorrelation characteristics of arrhythmic signals in MCGs, the randomness behaviour of the AFib can be measured by other parameters such as entropy and HRV. Spectral entropy (SpEnt) describes the complexity and randomness of cardiac mechanical behaviour and aims at interpreting the degree of disorder or randomness from spectral density analyses. HRV, or variation of successive cardiac cycles in MCG, represents the timing irregularities as abnormal deviation of heart rate is a remarkable sign of arrhythmia. SpEnt together with HRV analysis can effectively contribute as potential predictors of the AFib using MCG derived signals. Previous work on knowledge-based learning of AFib has been introduced by Hurnanen et al (2016) [270] in which an automated detection framework using a linear least-squares classifier with spectral entropy and heart rate variability measure as input parameters on a small group of subjects. The proposed method tolerates well interpersonal variations in the signal morphology as well as noise, because it does not require direct heartbeat detection from the SCG signal. The method relies on autocorrelation for cardiac cycle estimation in short episodes of SCG signals and considers power spectral density changes in sinus and fibrillatory rhythms. An extended version of this method was later developed for smartphone AFib detection in a blinded clinical trial (NCT03274583) with 300 cardiac disease patients (AFib positive=150) [128]. The method revealed an average accuracy of 96%.

6.3.2 Machine Learning for AFib Detection

An effective detection of previously undiagnosed AFib patients constitutes one of the most current challenges in the medical sector. To meet the challenge, cheap, simple, reliable, and convenient methods are

needed to detect asymptomatic AFib so that the benefit for those who are detected earlier as a result of screening can be maximized. Efficient and low-cost approaches to screen AFib are yet to be introduced. There is a great clinical demand for precise detection and classification of AFib with much faster and smarter algorithms.

Machine learning or artificial intelligence based arrhythmia detection is a recently widely used approach to discriminate cardiac abnormalities with the help of multidisciplinary features as well as advanced and complex classification models. Machine learning focuses on the computational challenges of building statistical models from a massive amount of data and seeks to learn relationships from data. A considerable amount of theory exists for learning algorithms and complex modeling techniques that aim at exploring effective solutions for problems in medicine, specifically in cardiology. The ultimate goal of MCG research as described in this work is to develop a cheap, ubiquitous, and noninvasive method (which requires neither electrical contact to skin nor additional equipment) suitable for screening hidden AFib from large masses.

To this end, and in addition to knowledge-based approach for AFib detection in SCGs, Lahdenoja et al. (2017) [113] presented a novel combination of smartphone SCG and GCG signals for automated detection of AFib using machine learning. The study revealed improved detection of AFib when joint smartphone SCG and GCG signals are fully exploited. The use of gyroscope together with accelerometer allows a comprehensive study of the heart activity as there are specific changes during AFib in both time domain and magnitudes of beats that are not always visible in SCG signal. These findings create a foundation for the development of smartphone MCG-based AFib detection algorithms. Figure 6.14 shows 6-axis motion sensing and corresponding ECG recording during AFib and sinus rhythm. As can be seen, Figure 6.14 (A) shows dominant characteristic changes in the mechanical signals as compared to Figure 6.14 (B). Additionally, Figure 6.14 (A) shows that GCG signals remain recognizable and ventricular or systolic complexes in each heartbeat are explicitly irregular. In contrast, SCG signals although appear irregular during AFib, in their texture the cardiac operation is barely visible. This implies further benefits of using multidimensional MCG for AFib detection as GCG and SCG offer different characteristics of signal complexity and randomness during a specific arrhythmia.
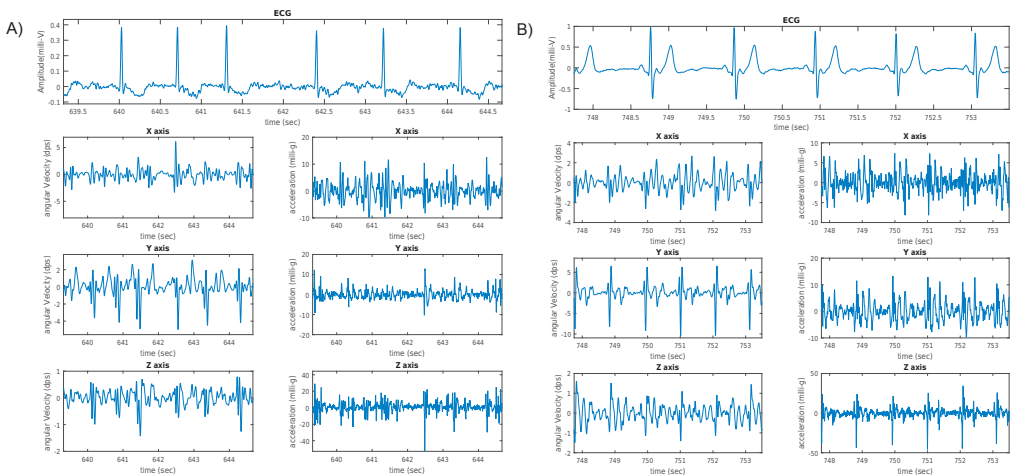

Figure 6.14: **Figure A** shows timing variation and amplitude behaviour during AFib. **Figure B** presents the autocorrelation of the SCG measurements during normal sinus rhythm.

In continuation of the previously developed methods in MCG processing [113, 270], the focus of Study V is to use a supervised learning for classifying AFib patients. In this study, a large dataset (n=435 subjects including 340 cardiac patients and 95 healthy volunteers) is considered, and various feature engineering and machine learning techniques are used to evaluate the diagnostic performance of the

smartphone MCG in detecting and quantifying AFib.

A fully automated AFib detection framework consisting of various signal processing and data analysis steps is designed to detect the existence of AFib in individual patients. The purpose of this work was to extend previous works towards efficient operation among the full adult population range, and to present a novel algorithm and additional machine learning features for smartphone based AFib detection. Figure 6.15 shows the overall view of the machine learning pipeline including pre-processing, feature engineering, feature matrix, and classification methods.

6.3.3 Feature Extraction from MCGs

Feature extraction starts from a similar framework as described in [113]. A preliminary signal pre-processing (including SSA filtering and wavelet-based envelope extraction) is performed by first segmenting the signals from each of the six axes *(AccX, AccY, ..., GyroZ)* into certain lengths, subsequently various features are extracted — incorporated into three feature matrices as 6-axis SCG-GCG, 3-axis SCG, and 3-axis GCG — and finally different classification techniques are used to distinguish AFib. A full list of features with their characteristic details is presented in Table 6.1.
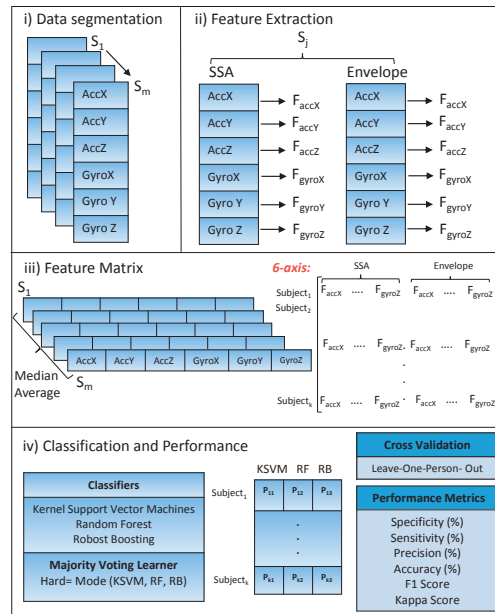

Figure 6.15: General schematic of machine learning pipeline.

6.3.4 Cardiac Ischemia Detection with MCGs

Early detection of coronary artery disease is extremely important in order to guide the patients into medical treatment. The detection of CAD is also a key requirement towards improved treatment, reduction in mortality and morbidity, and to the reduce the healthcare costs which are rapidly increasing. Detection of indications of CAD and acute myocardial infarction (AMI) using precordial accelerations has been previously investigated [145, 147, 149, 151]. AMI is a serious heart condition as part of the heart muscle tissue is damaged (irreversible injury) due to insufficient oxygen supply by coronary arteries. When a person feels obscure acute chest pain, it may be caused due to for example a heartburn or it may

Table 6.1: Description of contributing features in AFib Detection from MCG recordings

No	Feature	Description
1	Zero Crossing Rate	Rate of sign changes in a time series
2	Energy and Its Entropy	Measure of irregularity of the signal energy
3	Spectral Centroid	Center of mass of the signal spectrum
4	Spectral Spread	Mean variation of the rate-map around its centroid
5	Spectral Flux	Measure of how fast the power spectrum changes in a signal
6	Spectral Roll-off	Measure of the amount right-skewness of the power spectrum
7	Fundamental Frequency	The lowest frequency of a periodic waveform
9	Heart Rate	Median of the absolute values of cardiac interbeat intervals
10	Harmonic-to-Noise ratio	Measure of the overall periodicity of the signal
11	Spectral Peaks	Position and amplitude of six largest peaks in the density spectrum of the signal
12	Spectral Power	Total spectral power of the signal frame in 5 different frequency bands as [0.5-1.5] Hz, [1.5-5] Hz, [5-10] Hz, [10-15] Hz, and [15-20] Hz
13	Median Amplitude Spectrum	Median spectral density by normalizing spectrum of small bins over the total amplitude of spectrum
14	Covariance	Height of main peak, as well as position, and amplitude of the first side peak in autocorrelation
15	Approximate Entropy	Self-similarity test that quantifies the unpredictability of fluctuations in a time series
16	Spectral Entropy	Measure of complexity or randomness of a time series
17	Shannon Entropy	Discrete probability distribution of energy measuring average random samples from that distribution
18	Turning Point Ratios	Non-parametric detection of the randomness of the signal
19	Heart Rate Variability	Changes in the beat-to-beat heart rate obtained by autocorrelation
20	RMSSD	Root mean square of the successive difference of cardiac cycle intervals
21	HRV Power	Spectral density of the the beat-to-beat variations
22	Higuchi Fractal Dimension	Measure of signal complexity for analysing non-periodic or irregular time series
23	Hjorth Parameters	Measuring activity, mobility, and complexity
24	Kurtosis and Skewness	Measure of symmetry or lack of symmetry, as well as measure of the tailedness of the probability distribution
25	Mean and RMS Level	Mean value and root-mean-square of the signal

be a symptom of AMI (angina pectoris). A coronary angioplasty operation can be used to remove the blockage from coronary arteries to reduce the damages caused by the loss of oxygen into the heart.

Another aspect of heart motion analysis using MCGs is to enhance detection accuracy for AMI and related diseases. The aim of this part of research was to develop a solution which could either be integrated into a medical app for the use of telemedicine/smartphone cardiography by a trained medical personnel or as a standalone solution to wearable users in order to help recognizing this life-threatening condition earlier. The developed solution similarly extracts the heart vibration signals of a patient using the accelerometer and gyroscope sensors that are embedded into a smartphone. The main hypothesis for AMI/CAD studies comes from the fact that ischemia is a disease dealing with the mechanical functionality of the heart muscle and therefore MEMS motion signals should be potentially able to reveal corresponding mechanical failure due to ischemic changes. Figure 6.16 shows mechanical signals obtained during AMI (STEMI) and normal conditions.
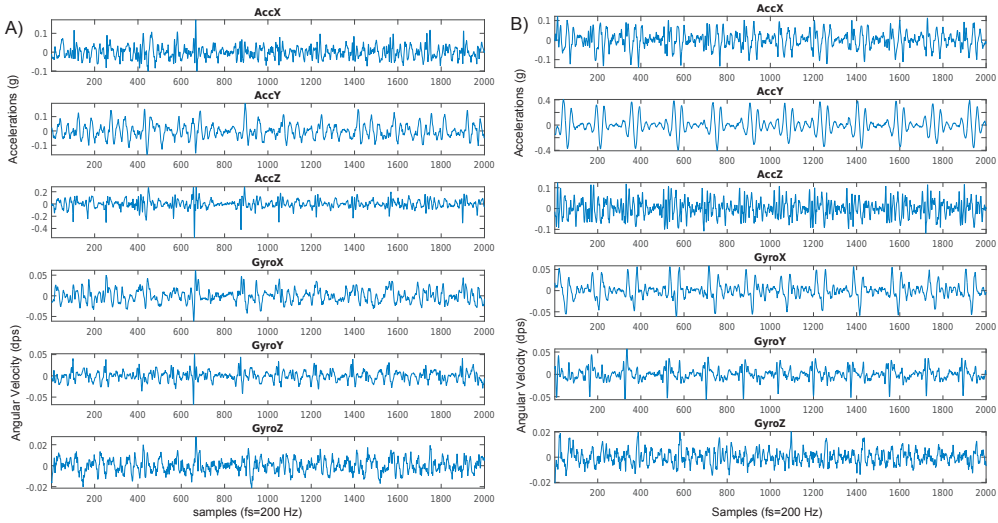

Figure 6.16: **Figure A** shows cardiac vibration signals during AMI. **Figure B** demonstrates joint SCG-GCG signals during normal conditions [from [166] with permission © IEEE].

In order to detect AMI or more precisely STEMI, 1D local binary pattern (LBP) [271] technique was considered to explore waveform changes in the multidimensional MCG signals and compare these pathological changes with normal conditions. Figure 6.17 illustrates the overall process of feature extraction and classification framework for MI detection in MCG recordings. The origin of LBP methodology lies in texture mining in image processing (2D-LBP), but it has been tried for various other image analysis tasks, such as face recognition, biometrics, and beyond (see [272] [273]). LBP is invariant to signal bias, which is believed to make it suitable for the analysis of the actual shape of the underlying signal and its small scale micro-structure. The idea behind 2D-LBP is based on evaluating the neighbourhood pixels — in terms of intensity differences — found at certain angles when we rotate from 0-360 degrees in anti-clockwise direction. The neighbourhood pixel coordinates around a point g_c are found by $(-R \times sin(2\pi p/P), R \times cos(2\pi p/P))$

$$\text{LBP}_{\text{P,R}} = \sum_{p=0}^{P-1} \text{s}(g_p - g_c)2^p, \tag{6.12}$$

where g_c and g_P are respectively values of the central point c, and the surrounding point P in the circle
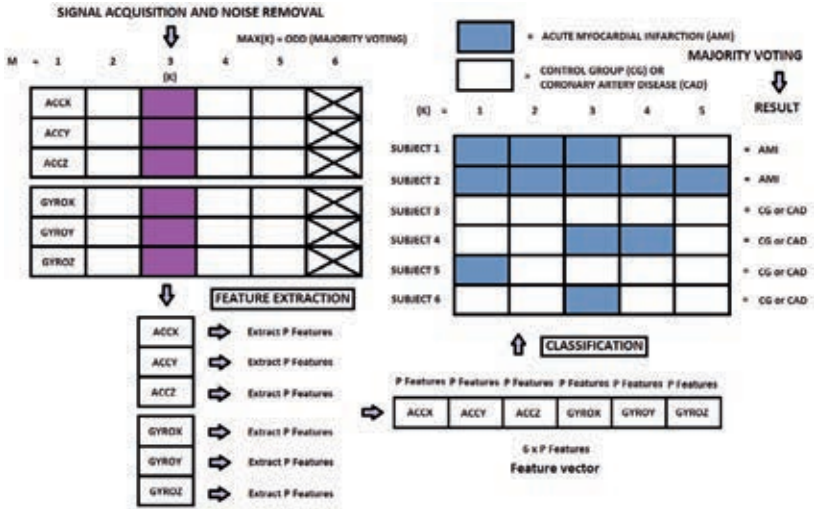
Figure 6.17: Overall diagram of the machine learning part of the STEMI detection (two-class case). Signal acquisition is made with a smartphone and subsequently data pre-processed (including motion artifact removal and filtering). A feature vector includes one LBP histogram with fine spacing (r=3) of the original signal segment and one LBP histogram for an integrated version of the same signal (chest's angular displacement) with fine spacing. Additionally, the same procedure is applied to signal with a coarse spacing (r=21). In total there are four LBP histograms of length 59 bins corresponding to single segment and axis (P=4*59). The length of the overall histogram for six axes is 6*P features. Feature matrix is fed into the classifier and subsequently using a LOOCV and majority voting scheme STEMI condition is discriminated from other conditions [from [166] with permission © IEEE].

neighbourhood with a radius R, and function $s(x)$ is defined as:

$$s(x) = \begin{cases} 1, x \geq 0 \\ 0, x < 0 \end{cases} \tag{6.13}$$

Those coordinates which do not exist are assigned a value using interpolation. Apart from being faster to calculate, rotation invariance is another well known property of the LBPs [272]. An efficient variant of 2D-LBP called uniform 2D-LBP which includes only those binary patterns which change only once, either from 0-1 or from 1-0. Uniform patterns have minimum transitions and as such act as pattern templates for interesting features in an image. These uniform LBPs are thought to cover the fundamental properties of most textures observed in a neighbourhood around a center point [272].

For the purpose of AMI detection via MCG, we used 1D-LBPs variant as it is suitable for input vector data types. For any time index in the input vector the neighbourhood we consider is, d pixels (samples) before and after the index position being analyzed. An additional parameter called spacing is also used to speed up the computation and to extend the used local neighborhood.

6.3.5 Multiclass Learning for Cardiovascular Condition Assessment

In addition to independent detection of AFib and AMI, Study VI presents a multi-class classification learning approach to assess various heart conditions (Normal, AFib, CAD, STEMI) using a smartphone-only solution. The motivation behind this approach is that abnormal morphological changes in cardiogenic vibrations – possibly due to hypoxic myocardium tissue – are recognizable and therefore can

improve detection of heart arrhythmia and ischemic heart diseases. A potential impact of this approach is efficient prevention and follow-up of patients with various heart conditions, enabled by mobile technology.
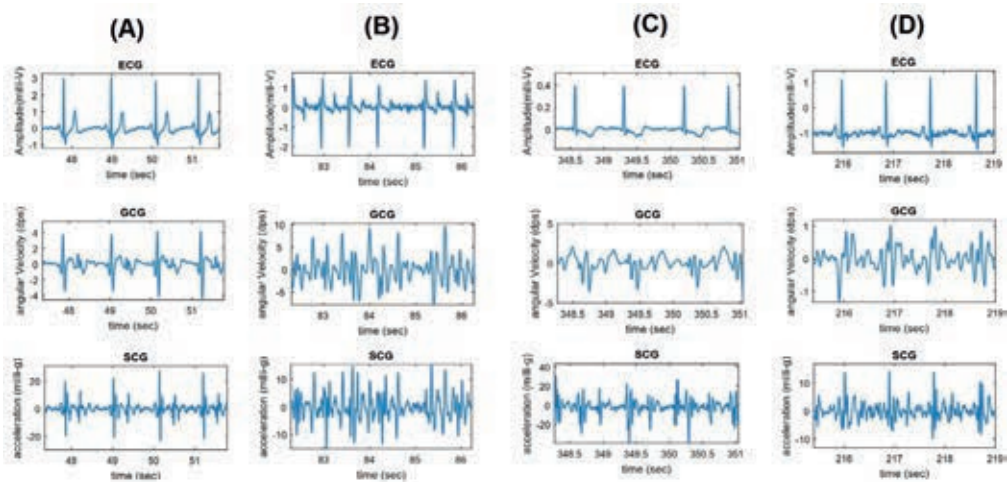

Figure 6.18: **Figure A** shows overall waveform characteristics of normal heart functioning, **Figure B** shows irregular and random LV contraction due to atrial fibrillation, and **Figure C and D** show CAD condition with ischemic changes: T-wave inversion (C) and ST segment depression (D) in ECG (lead I), GCG, and SCG signals.

As described in the previous sections and Figure 6.18 shows, during the normal condition both electrical and mechanical signals follow a regular rhythm and monomorphic repeating patterns while in AFib condition ventricular contractions appear irregular in terms of rhythm and morphology. More precisely, due to the atria failure in mechanical function, the left and right ventricles may response with abnormal systolic-diastolic functioning. In CAD condition, although regular rhythm is visible in SCG-GCG, cardiac motion pattern has undergone considerable changes such as poor contractility (amplitude reduction), larger diastolic activity, and widened systolic complex (as shown in D multiple wide wavelets are visible in the onset of systole), potentially due to the artery blockage.

This multi-class learning approach benefits from features generated in [113, 166]. In total, 18 AFib features, 11 spectral energy features, and 4 uniform local binary patterns (LBP) histograms of length 59 are considered for multiclass learning in MCG recordings. The LBP histograms are formed by applying different spacing between the bits (of 3, 21) and using the same two spacing with an integrated version of the input signal. Table 6.2 represents different categories of features selected for the multiclass classification task.

As described in [166] the classification results are made with majority voting, which means that all segments in a particular measurement (person) are used to vote for the final class. In the multiclass framework, this simply means that the class which is the most common among the evaluated segments is chosen to be the final result. In the two-class case, the class which is more common is also chosen as the detection result.

6.3.6 Classification and Cross Validation

Kernel support vector machines (KSVM) and random forest (RF) were the main classifiers used in this work for discriminating cardiac conditions (Study V and VI). These learning algorithms were used based on their mathematical characteristics in differentiating cardiovascular disorders using the previously explained features for AFib, AMI, and multi-disease detection. A majority voting learner (MV) was also

Table 6.2: Four major groups of features based on heart rate variability (HRV), signal energy, spectral entropy (SpEn), approximation entropy (ApEn), turning-point ratios (TPR), and local binary patterns (LBP) for multiclass learning.

Feat.	Abbr.	Description	Dim.
1	SPEN	Entropy of the signal frequency spectrum	1
2	HRV	Heart rate variability from short-term autocorrelation	3
3	HR	Heart rate (from short-term autocorrelation)	1
4	TPR	Turning-point ratios (extracted with different filters and without filter)	11
5	RRI-TPR	Turning-point ratio of beat-to-beat intervals	1
6	APEN	Approximate entropy	1
7	ENE_FEATS	Energy of signal segment with different bandpass filters	11
8	1D-LBP	1D-Uniform LBP histogram (ULBP) with spacing 3	59
9	1D-LBP	1D-ULBP with spacing 21	59
10	1D-LBP	1D-ULBP of integrated signal (Matlab's cumtrapz) with spacing 3	59
11	1D-LBP	1D-ULBP histogram of integrated signal (Matlab's cumtrapz) with spacing 21	59
All		(single vector)	265

defined in Study V which practically combined predication probabilities made by multiple classifiers including RF, KSVM, and Robust Boosting (RB) which is an ensemble of classification trees. The RB algorithm is an effective classification approach by which results from many weak learners, for instance, decision trees, are melded into one high-quality ensemble predictor.

Cross-validation study, which is a process to test how the trained model or classifier performs with respect to the given training set, was considered subsequently. In practice, cross validation is used to assess the performance of the model by predicting the error rate of a learning technique. With cross validation, the given data set is generally split into two partitions named as *train* and *test* and thereby the classification error is calculated by training the learned model with the *train* subset and testing it with the unseen *test* subset. There are several standard ways to perform cross validation such as k-fold (k≪ number of samples) where the data is divided into fixed number of folds/partitions, and leave-one-out cross validation (LOOCV) which is n-fold cross validation, where n is the number of observations/samples in the dataset. With LOOCV, the model is fitted with $n - 1$ samples to predict the probability of the outcome with the one sample which has been excluded. This process is repeated, excluding a different sample until all of the samples in the given data set had a predicted probability obtained from a model trained to all of the others.

In this Ph.D. work, a leave-one-person-out cross validation is adapted to evaluate the generalization performance (the sensitivity and specificity) of classification algorithms. Accordingly, cross validation process relies on excluding one subject from the total number of subjects and the learning model is trained with the remaining subjects' data. It is worth noting that choosing the right approach for cross validation scheme is of high importance, as for example in the case of AFib detection, it is very crucial to detect an individual diseased subject at a time. Quantitative evaluation of the classification performance using LOOCV is expected to be slightly affected resulting in more pessimistic predictions, but this approach — apart from obtaining learning error rates with lower bias — prevents over-fitting problems. This is important to consider specifically when we deal with a small set of training data. LOOCV is, however, computationally expensive and tends to have a high variance [274].

Chapter 7

Results

7.1 Validation of Accelerometer-Based Cardiac and Respiratory Gating Signals

Study I presents an accelerometer-based system was presented as a potential solution for dual gating in nuclear medicine imaging and validated with a reference ECG and a respiration belt. Deterministic cardiac time interval estimation algorithms were used to estimate systolic and diastolic phases of the mechanical cardiac cycles (SCGs). Additionally, ADR signals were compared to a reference respiration belt during three different breathing patterns, namely normal, slow, and fast pacing. The correlation coefficients (r) between ADR and respiration belt measurements were 0.9945, 0.9981, and 0.9941 for normal breathing, slow-paced breathing, and fast-paced breathing, respectively. Figure 7.1 shows that ADR signals follow the reference respiration belt traces during different breathing patterns with a high agreement.
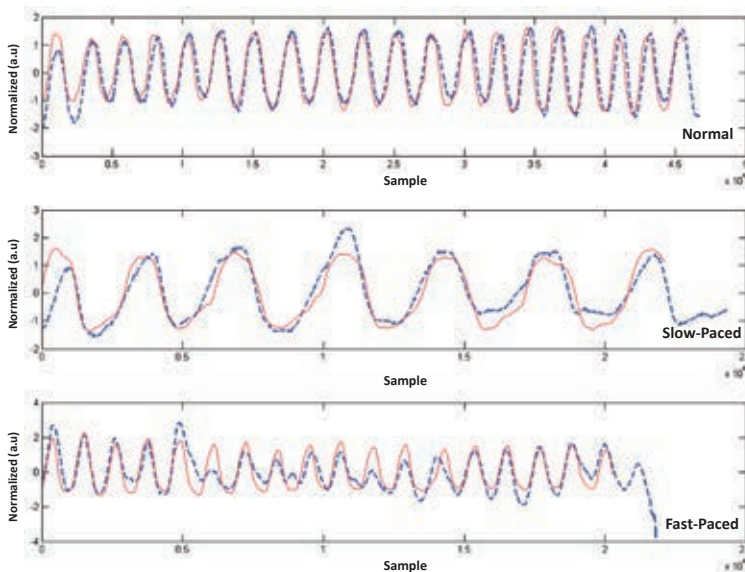

Figure 7.1: Respiratory cycles obtained from ADR (dashed blue line) and reference respiration belt (red solid line) in three different patterns, normal breathing, slow-paced breathing, and fast-paced breathing [from [224] reprint under ©(i)].

7.2 Stand-alone Heartbeat Detection in SCG and GCG

Study II presents HABIT approach adapted for the detection of heartbeat timings and interbeat time intervals in SCG is tested on 29 healthy volunteers in three different positions, namely supine, left and right recumbent [263]. The average true positive rate (TPR), positive prediction rate (PPR) and detection error rate (DER) for different positions are as follows (TPR, PPR, and DER): supine (95.8%, 96.0% and $\simeq 0.6\%$), left (99.3%, 98.8% and $\simeq 0.001\%$) and right (99.53%, 99.3%, and $\simeq 0.01\%$). High correlation and agreement is observed between SCG and ECG interbeat intervals (r>0.99) for all positions which highlights the capability of the algorithm for SCG heart monitoring from different positions. HABIT algorithm was later tested on gyroscopic signals obtained from the same dataset in [263] to delineate cardiac mechanical waveforms in GCG. The average TPR, PPR and DER for different positions were as follows (TPR, PPR, and DER): supine (99.4%, 99.5% and $\simeq 0.038\%$), left (99.66%, 99.7% and $\simeq 0.034\%$) and right (98.9%, 96.6%, and $\simeq 0.049\%$).

In continuation of the HABIT algorithm, Study VII presents a standalone heart beat detection [275] in which the above-mentioned study group (Dataset I, n=29) and a group of CAD patients (Dataset II, n=12) were tested. For Dataset I the TPR and PPV rates were 99.9 % and 99.6 %, respectively with improved performance compared to the earlier contribution [263]. The same metrics for Dataset II were 92.0 % and 92.2 %, respectively.

Apart from heart rate monitoring, joint SCG-GCG monitoring allowed measuring an electromechanical delay (EMD) which is defined as the time interval between the onset of the ECG QRS-complex and the onset of the systolic wave in MCG [276]. Figure 7.2 shows the statistics of the mean EMD and the standard deviation of the beat-to-beat EMD from Dataset I. In comparison to SCG, the GCG derived EMDs had smaller bias and variability, which means a better approximation for relative PEP can be obtained by GCG.
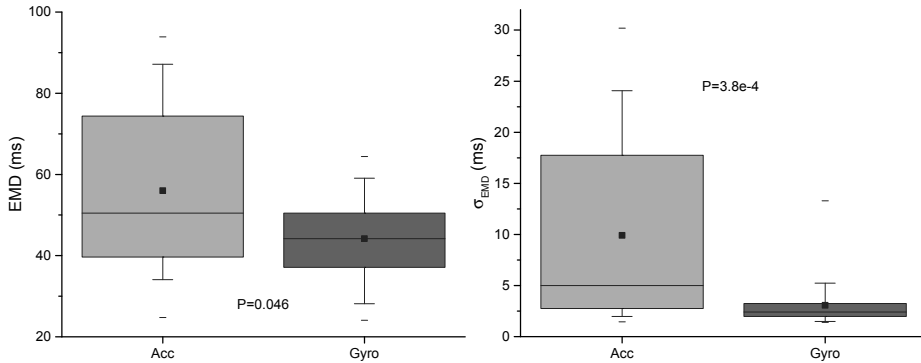

Figure 7.2: EMD between ECG R-peaks and MCG's mechanical activation points.

7.3 Characterization and Analysis of Gyrocardiography and Waveforms Annotation

Study III presents simultaneous recordings of ECG, GCG, and echocardiography in order to annotate underlying fiducial points in GCG in a group of subjects consisting of nine healthy volunteer men. Accordingly, these concurrent measurements together with complementary quantitative and qualitative inspections revealed the following outcomes.

Around the ECG R-wave and during the systole, a fast downward notch in the GCG y-axis wave pattern is visible that is denoted by $gyro_I$ (g_I). Subsequently, another major maximum peak in the GCG y-axis is denoted by $gyro_J$ (g_J); this peak occurs slightly after the ECG R-wave and is considered to

be the mechanical activation of LV contraction. Further in the middle of the cardiac cycle and roughly after the ECG T-wave (around the second heart sound (S2)), a lower magnitude up-down wave (almost $\wedge$ shape) is visible which consists of two reproducible and repeating notches just before and after the $\wedge$ wave peak. This waveform is mostly visible in the signal obtained from the x-axis of the GCG, and are therefore nominated the by $gyro_K$ (g_K), and $gyro_L$ (g_L), respectively. With distinguishing of GCG g_I, g_J, g_K, and g_L points in every cardiac cycle, the IVCT and the IVRT are estimated. Additionally, other significant systolic time intervals and indexes of cardiac contractility such as QS2, LVET, and PEP are estimated. It was shown that GCG can estimate pre-ejection period, left ventricular ejection time, isovolumetric contraction and relaxation times, and systolic-diastolic peak velocity points. GCG signal was also compared to tissue velocity (TV) and strain curves obtained by TDI and speckle tracking analyses, and it was shown that the timing of the maximal strain is correlated with certain waveforms in the GCG signal. Figure 7.3 illustrates the annotated GCG waveforms and the corresponding cardiac time intervals. Table 7.1 shows estimated cardiac time intervals, error rates (RMS), and correlations measured by reference echocardiography, ECG, and GCG based annotated cardiac events.
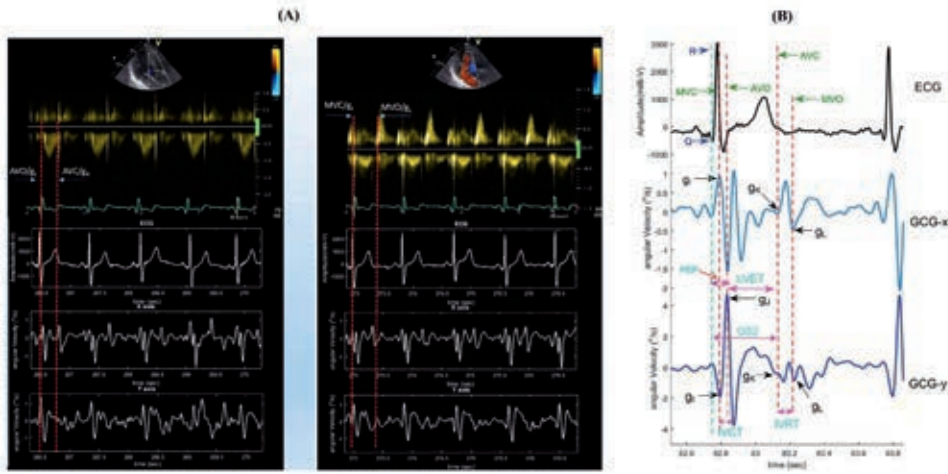

Figure 7.3: Waveform annotation and cardiac time interval estimation in GCG signal. **Figure A** shows aortic (left) and mitral (right) valve opening and closure moments as measured by PW Doppler and in GCG signal. **Figure B** specifies waveform annotation in GCG and corresponding time intervals with respect to ECG peaks [from [163] reprint under ⓒ①].

Echocardiography	Mean $\pm$ SD	GCG	Mean $\pm$ SD	r^2	RMSE
HR (bpm)	59 ± 12	HR	58 ± 11	0.99	0.95
R-MVC (ms)	20 ± 6	R-g_I	18 ± 5	0.66	3.5
R-AVO (ms)	49 ± 10	R-g_J	47 ± 10	0.96	2.2
R-AVC (ms)	359 ± 32	R-g_K	358 ± 36	0.95	7.5
R-MVO (ms)	427 ± 44	R-g_L	432 ± 41	0.97	7.6
IVCT (ms)	29 ± 12	IVCT	30 ± 10	0.85	4.5
IVRT (ms)	68 ± 14	IVRT	74 ± 9	0.59	9.4
QS2 (ms)	393 ± 34	QS2	394 ± 38	0.78	19
LVET (ms)	310 ± 26	LVET	310 ± 32	0.93	7.7
PEP (ms)	82 ± 10	PEP	83 ± 8	0.84	4.5
Q-Sa (ms)	134 ± 20	Q-SPV	132 ± 26	0.89	7.6
Q-Ea (ms)	467 ± 44	Q-DPV	460 ± 49	0.87	16
Q-Max Strain (ms)	367 ± 32	Q-Max Ang Disp	371 ± 31	0.91	10

Table 7.1: US and GCG derived information for underlying cardiac time intervals.

7.4   MEMS Dual Gating for Cardiac PET

Study IV presents the applicability of MEMS dual gating for cardiac PET imaging with two atherosclerosis patients. Dual gated PET images are successfully reconstructed using only MEMS signals. With MEMS cardiac gating approach, SCG-GCG signals are divided into 3 bins, two small systolic and one larger diastolic bin, while ADR and GDR signals are segmented into 5 bins of equal height. For MEMS-based respiratory gating, amplitude-based approach is used as it allows accurate derivation of gating intervals for patients with irregular respirations [277]. Figure 7.4 shows cardiac dual-gated PET images with non-gated, ECG-RPM, and MEMS dual gating. The myocardium appears less blurred in both RPM and MEMS gated images as compared to non-gated images indicating a reduced partial volume effect due to gating. Notably, the MEMS gated image shows less noise as compared to the ECG-RPM gated image due to improved separation of the quiescent periods of cardiac and respiratory cycles.
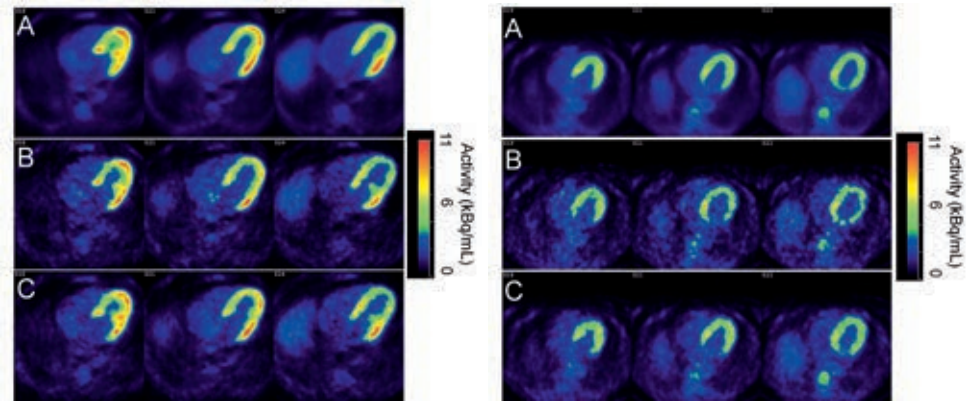

Figure 7.4: Transaxial view of non-gated (A), ECG-RPM (B), and MEMS (C) dual gated cardiac PET images obtained via ECG-RPM and MEMS gating for Patient 1 (left) and Patient 2 (right). Notable blurring in the myocardium is visible in non-gated images which is reduced by dual gating.

Results in Table 7.2 show that MEMS-gating preserves more data in cardiac PET imaging than conventional dual-gating using ECG and RPM. It also improves the signal-to-noise ratio (SNR) and yields similar target-to-background ratio (TBR) than the ECG-RPM method as shown in Table 7.3.

Table 7.2: Gating statistics indicating the percentage of data saved compared to non-gated PET.

Subject	RPM	ECG	ECG-RPM	MEMS Respiration	MEMS Cardiac	MEMS Dual
Patient 1 (male)	14.1 %	31.8 %	3.9 %	17.4 %	60.0 %	10.4 %
Patient 2 (female)	21.3 %	45.8 %	10.4 %	26.0 %	59.4 %	15.4 %

Table 7.3: Quantitative analysis of PET images.

Subject		No Gating	ECG-RPM	MEMS
Patient 1 (male)	SNR	24.91	7.85	12.93
	TBR	1.57	1.78	1.75
Patient 2 (female)	SNR	23.72	11.57	12.43
	TBR	1.75	2.43	2.33

7.5   Cardiovascular Condition Assessment

7.5.1   AFib Detection with Machine Learning

Study V aims at assessing the diagnostic performance of a joint SCG-GCG method by considering 435 subjects including 190 AFib and 245 sinus rhythm cases. A fully automated AFib detection algorithm consisting of multidisciplinary features and machine learning steps is developed and evaluated through a leave-one-out-cross-validation study with a large set of patients (n=300, 150 AFib). The trained models including KSVM, RF, and RB are further tested on an unseen test set of size 135 (40 AFib). The experimental results revealed that the method could discriminate AFib and SR with accuracy, sensitivity, and specificity of approximately 97%, 99%, and 95% for the cross-validation study and 95%, 93%, and 97% for the cross-database test experiment, respectively. A positive predictive value of approximately 95% and 92% was obtained respectively for the LOOCV and test set suggesting high reproducibility and repeatability for mobile AFib detection. Additionally, the F_1 scores were respectively 97% and 96% for the cross-validation and test studies, and the Cohen's kappa scores were 0.94 and 0.88 indicating a near-perfect agreement in rhythm classification between the smartphone algorithm and visual interpretation of telemetry ECG recordings.

Table 7.4 and 7.5 present the achieved results respectively for the cross-validation and cross-database studies where three sets of classification quality metrics are reported, each correspond to a feature group. Figure 7.5 shows the overall performance of the AFib detection method using receiver operating curves (ROC) in combined SCG-GCG, only SCG, and only GCG features obtained with 10 second segmentation. As shown, the area under the curve (AUC) obtained by RF is superior (0.987-0.991) as compared to KSVM (0.972-0.983), and RB (0.968-0.976) in all cases. As can be seen from the tables and ROC plots, the six-axis feature combination derived from 10 sec segments represents a slightly higher discriminative performance than the two other feature groups, namely SCG/GCG derived features.
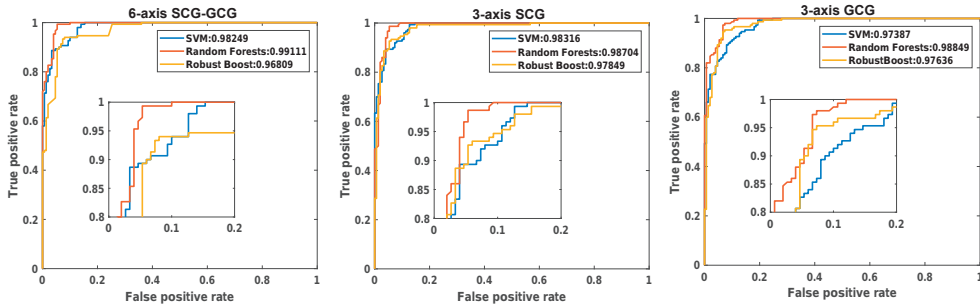

Figure 7.5: ROCs and AUC values obtained with RF, KSVM and RB classifiers with 10 second episodes.

Table 7.4: Classification performance results for the cross validation study with different segmentation and feature groups.

Feature matrix	6-axis SCG-GCG							3-axis SCG							3-axis GCG						
Segmentation (best classifier per group)	SE	SP	PR	kappa	F_1	ACC	AUC	SE	SP	PR	kappa	F_1	ACC	AUC	SE	SP	PR	kappa	F_1	ACC	AUC
10 sec (RF/RF/MV)	**98.6**	**95**	**95**	**0.94**	**97**	**97**	**0.99**	97.3	94.7	94.8	0.92	94	96	0.99	97.3	93	93	0.9	94.5	95	0.99
20 sec (MV/MV/MV)	98.6	93	93	0.92	96	96	0.96	98	94	94.2	0.92	96	96	0.96	96	93	93	0.87	94	94	0.93
30 sec (MV/MV/MV)	97.3	92.7	93	0.90	95	95	0.95	97.3	94.7	94.8	0.92	95.6	96	0.96	96.7	92	92.4	0.88	94	94.3	0.94
40 sec (MV/MV/MV)	98	93	93	0.90	94.5	95	0.95	98	92	92	0.9	95.8	95	0.95	97.3	93.3	93.5	0.91	95	95.3	0.96
50 sec (RF/RF/RF)	97	92	92.4	0.89	94.5	95	0.99	96	93.3	93.5	0.89	93	94.7	0.99	97.3	92.7	93	0.9	94.5	95	0.99
60 sec (RF/MV/RF)	97.3	92.7	93	0.90	95	95	0.99	98	93.3	93.6	0.91	95.5	96	0.96	96	93.3	93.5	0.89	94.6	95	0.99

The best performing features — derived from 10s episodes of cross-validation study — which yielded to the highest discriminative performance were selected using a simple filter approach described

Table 7.5: Classification performance results for the Cross-database test study with different segmentation and feature groups

Feature matrix	6-axis SCG-GCG							3-axis SCG							3-axis GCG						
Segmentation (best classifier per group)	SE	SP	PR	kappa	F_1	ACC	AUC	SE	SP	PR	kappa	F_1	ACC	AUC	SE	SP	PR	kappa	F_1	ACC	AUC
10 sec (MV/RF/MV)	**90**	**96.8**	**92.3**	**0.88**	**96**	**94.8**	**0.94**	90	96.8	92.3	0.88	95.6	94.8	0.93	88	97.9	94.6	0.87	96.3	94.8	0.93
20 sec (MV/RF/RF)	92.5	95.8	90.2	0.88	95	94.8	0.92	92.5	88.4	77.5	0.77	91	0.93	90	90	92.6	83.7	0.8	94	91.9	0.93
30 sec (MV/MV/MV)	85	94.7	87.2	0.79	94	91.85	0.93	87.5	92.6	83.3	0.79	92.5	91.1	0.93	82.5	97.9	94.3	0.82	95.4	92.6	0.93
40 sec (MV/MV/MV)	85	93.70	85	0.79	93.7	91.1	0.90	82.5	92.6	82.5	0.75	92.6	89.6	0.87	82.5	91.6	80.5	0.73	92.6	89.0	0.90
50 sec (MV/MV/MV)	92.5	92.6	84.1	0.82	95	92.6	0.92	85	90.5	79	0.7	92	88.9	0.91	90	93.7	85.7	0.82	92	92.6	0.92
60 sec (RF/RF/RF)	90	89.3	78.2	0.75	91.5	89.5	0.92	90	88	77	0.75	89	89	0.91	90	88	77	0.74	92	89	0.92

by [278]. Accordingly, an accuracy of 97% was obtainable with only 39 joint SCG-GCG features. Figure 7.6 shows how frequently these features are selected among the total 39 best features as the candidate features may obtain from different measurement orientations. As shown, among these attributes, the RMSSD (26%), HNR (15%), F_0 (18%), and spectral flux (15%) had the greatest contribution in AFib classification.
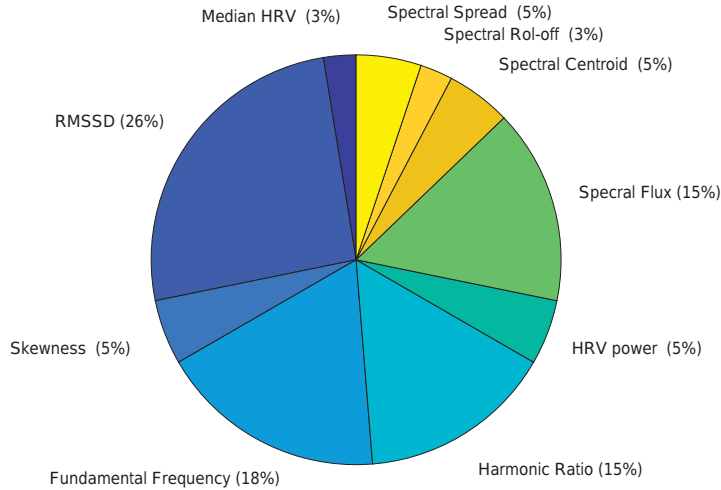
Figure 7.6: Contribution of best SCG-GCG features in AFib detection.

7.5.2 Arrhythmia and Ischemia Detection with Multiclass Learning

Study VII suggests that smartphone mechanocardiography could be used to separate cardiovascular conditions such as normal sinus rhythm, AFib, CAD, and possibly ST-segment elevated myocardial infarction (STEMI) in a multiclass setting. This study considers two class (AFib versus sinus rhythm, CAD versus healthy sinus rhythm, and CAD versus STEMI), three-class (Normal, STEMI, CAD), and four class (Normal-AFib-STEMI-CAD) using KSVM and RF classifiers. With the binary classification tasks, an accuracy of 98% was obtained for AFib detection, 86% accuracy in discriminating CAD patients from healthy subjects, and 72% accuracy for classifying AMI from CAD. Figure 7.7 shows classification accuracy for the binary discrimination of different cardiovascular conditions. The accuracy of the 3-class classifier was 73% without majority voting and 78.46% with majority voting. The accuracy of the 4-class classifier was 71.17% without majority voting and 75.24% with majority voting.
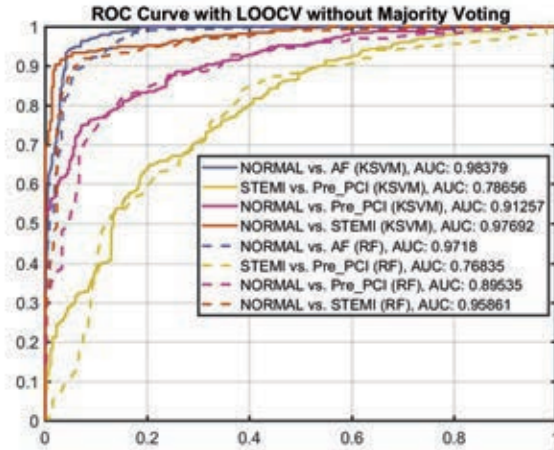
Figure 7.7: ROCs for multiple cardiac condition classifications [from [279] reprint under ⓒⓘ].

In addition to the accuracy calculation, another metric so-called F_1 score was calculated which is an average F_1 value from the classification types. Accordingly, Tables. 7.6 and 7.7 represent F_1 scores calculated for 3- and 4-class setting with and without majority voting, respectively. As such, for the 3-class setting the best F_1 score achieved by KSVM without majority voting (78%), while for the 4-class setting the best score was given by RF classifier (74%) again without majority voting.

F score	Without Majority Voting		With Majority Voting	
	RF	KSVM	RF	KSVM
F1n	0.88	0.91	0.84	0.86
F1m	0.74	0.75	0.75	0.72
F1p	0.56	0.67	0.57	0.56
F1	0.72	**0.78**	0.72	0.72

Table 7.6: Classification F1 scores for 3-class

F score	Without Majority Voting		With Majority Voting	
	RF	KSVM	RF	KSVM
F1n	0.82	0.89	0.80	0.85
F1a	0.77	0.81	0.75	0.77
F1m	0.65	0.62	0.56	0.57
F1p	0.70	0.60	0.60	0.59
F1	**0.74**	0.73	0.68	0.70

Table 7.7: Classification F1 scores for 4-class

Chapter 8

Discussion

The findings of this study suggest that wearable/mobile mechanocardiography based heart monitoring has impressive clinical implications. With multidimensional MCGs, analysis of heart motion becomes achievable to a new dimension, a dimension which is based on solely precordial vibrations originated from myocardial wall motion. The overall findings of this Ph.D. work, while preliminary, suggests that measuring the mechanical movement of the heart muscle offers an entirely new and innovative method to evaluate cardiovascular status as MCG-based cardiac monitoring can reliably detect cardiac abnormalities without any additional hardware and provides a new easy-to-use and accessible concept for screening purposes.

Due to the potential advantages of personalized health monitoring systems, a growing number of mobile/wearable devices would benefit from reliable monitoring of the heart. A personal smart monitoring platform can assess the health risks by early detection of cardiovascular disorders. For instance, MEMS gyroscopes and accelerometers can be either embedded into a monitoring patch or implantable device for long term usage or be employed from smart devices. These sensors are not subjected to intervention from electrical monitoring or implantable stimulating signals generated by ECG, pacemakers, and cardioverter defibrillators and therefore may be used for wearable continuous cardiac function monitoring in the future.

Smartphones are fast becoming ubiquitous, even among the elderly people, and the number of smartphone users is also increasing at a rapid rate in developing countries, where low-cost healthcare solutions are particularly crucial. The readily available smartphones provide a unique opportunity for cost-effective screening of cardiovascular disease, if they can be harnessed to reliably detect the symptoms. The performance of our smartphone MCG-based algorithms compares favourably to the various ECG (single-lead) algorithms in detection of cardiovascular disorders such as AFib and AMI.

For STEMI diagnosis, the clinical issue with ECG-based methods is the high frequency of false positive ECG findings such as early repolarization as well as ECG findings hindering ischemia detection such as the left bundle branch block, pacemaker rhythm or significant left ventricular hypertrophy. Current computer-aided algorithms for STEMI diagnosis possess a limited sensitivity (of 30-70%) and specificity (of 70-100%) [280]. Although the presented measuring approach revealed inband sensitivity and specificity values, its diagnostic performance for STEMI detection must be analysed not only with ECG data, but when taking clinical symptoms and coronary angiography findings into account. Such a holistic contextual analysis is routine for diagnosing mechanical wall motion abnormalities found in STEMI patients and heart failure patients with reduced ejection fraction (HFrEF).

Heart rate monitoring using MCG helps to assess the functionality and condition of the cardiovascular system. Current heart rate monitors are widely used for monitoring heart rhythm, heart rate variability analysis, fitness and stress test, sleep tracking, and many other healthcare applications [281]. For example, measuring physiological parameters such as the heart rate and blood pressure is recently conducted using smart devices (e.g. smart watches and smartphones), Google glass, wristband, weighing-scale, and cheststrap [169, 170, 179, 282–285]. Such cheap, noninvasive (and possibly disposable) vital sign monitors capable of long-term and frequent monitoring of the cardiac activity in an unnoticeable manner are an

attractive choice for massive screening purposes as they provide immediate feedback on cardiovascular function for example during fitness activities and stress tests. This study introduced robust and standalone algorithms for heartbeat detection in SCG and GCG signals for potential health and well-being applications. The presented algorithms combine linear and rotational cardiogenic signals derived from MEMS sensors and benefit from three main features that can significantly improve heart rate monitoring with MCGs as: 1) automatic axis selection, 2) motion artefact removal, and 3) standalone delineation of heartbeat in SCG-GCG signals.

Disturbing artifacts or noise in cardiac signals can be originated from various sources, such as body movement or environmental disturbances. Usually, there is a need to perform advanced pre-processing in order to separate the noisy signal segments (such as motion artifacts) from multi-dimensional MCG signals. Apart from noise, with joint accelerometers and gyroscopes, both intra and inter-subject variability between persons is large (in comparison with ECG). We presented a novel machine learning approach for ranking of cardiac signals according to their quality [286]. The method selects the best performing axis and sensor in terms of noise and waveform as the quality of the signal is defined how well the heart beats can be identified. A pairwise learning to rank approach base on ranking support vector machines algorithm was used to solve this issue. Learning to rank is used to SCG and GCG channels based on their relative importance with respect to each other as shown in Figure 8.1.
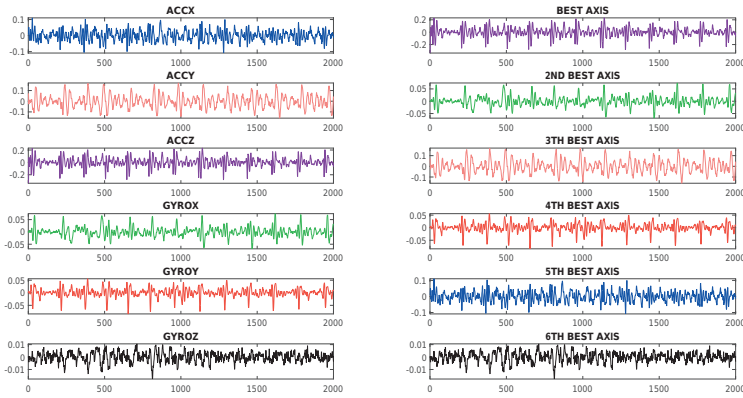
Figure 8.1: An example of ordering six IMU (3-accelerometer and 3-gyroscope) axes with respect to their relevance/quality. Derived cardiac signals from each channel on the left and right are highlighted with the same color. The length of each segment is 10 seconds at 200 Hz sampling rate of the smartphone. © Reprint with permission

Complementary to the clinical applications of the MCG, intensive considerations on gyrocardiography technique revealed that the gyroscopic signals are able to give reliable information on cardiac time interval measurements such as systolic and diastolic time intervals. STIs including left ventricular ejection time and pre-ejection period can be measured by detecting particular indicative mechanical cardiac events, for example, instants of MVC, AVO, MVO, and AVC in GCG signal. Moreover, newly-identified GCG points, namely systolic peak velocity and diastolic peak velocity, are indicative of cardiac mechanical performance (as research showed good temporal correlations between GCG and echocardiography velocity measurements) and can potentially provide functional information related to systolic and diastolic activities. Furthermore, it is shown that the time from ECG onset Q to the maximal TDI strain is correlated to the time interval from ECG onset Q to maximal point of GCG angular displacement. This electromechanical delay may bring new insights into the assessment of myocardial function as its variation, known as myocardial mechanical dispersion, can potentially help in detection of arrhythmias and myocardial infarction [79]. Therefore, wearable/mobile GCG as a promising mechanical cardiac

monitoring tool can be used in quantification of beat-by-beat dynamics of cardiac time intervals and can potentially represent information related to the hemodynamic variables and myocardial contractility.

In addition to heartbeat detection and cardiac time interval estimation by MEMS sensors, this work introduced a novel dual gating technique, for example, MEMS gating, for simultaneous acquisition of cardiac and respiratory signals using only mechanical sensors. Primary investigations showed a promising approach for motion correction using only gyroscope- and accelerometer-derived respiratory and cardiac signals for dual gated cardiac PET studies. Results indicated that MEMS-based dual gating improves image quality and reduces quantification errors. Figure 8.2 shows the line profiles drawn along the myocardium from RPM and MEMS gated PET images in both patients. The improvement of the contrast is seen by MEMS gating in patient 1, while the profile of the MEMS gated image is very similar with the profile of RPM gated in patient 2. Both MEMS gated images show better signal-to-noise ratio and smoother profile curves due to less noise [287].
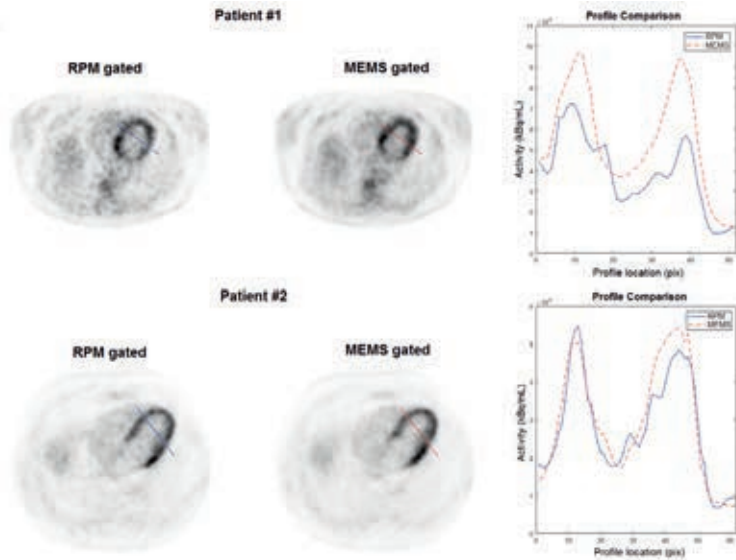
Figure 8.2: Count profiles along myocardium achieved by dual RPM-ECG (left) and MEMS gating (right) reconstructions (© Reprint with permission)

The advantage of using multi-axis MEMS motion detectors is two fold. Multidimensional mechanical sensing allows selection of the best axis in terms of signal quality and waveform stability for both cardiac and respiratory gating. Compared to the methods which rely on only ECG, the 6-axis motion sensing offers more freedom to derive gating information. Depending on the type of imaging, CT or PET, the x- and y-axis of gyroscope offer fairly robust rotational precordial vibrations and respiration curves, simultaneously. With the accelerometer, the z-axis provides high quality translational cardiomechanical vibrations, while the x- and y-axis comprise mainly respiration signals.

A major limitation for MCG based monitoring is its susceptibility to aggravated situations with high degree of the appearance of movement artefacts in the recorded signals, as the performance of the algorithms, that rely on waveform characteristics of heartbeats, in very low quality or noisy signals is affected considerably. The use of gyroscope can to some extent mitigate the influence of motion artifacts as it is less prone to the linear acceleration in the recorded signal [165]. In practice, the gyroscopes have higher tolerance to noise [164] and the obtained waveforms remain more monomorphic and stationary compared to accelerometer signals. Another limitation of this study is the noise level of the accelerometer sensors used in this Ph.D. work. The MMA8451Q and Bosch Sensortec BMI160 accelerometers — with an RMS noise of respectively 99 and 180 $\mu g/\sqrt{Hz}$ — tend to have a higher noise floor as compared to

the currently available sensors. Considering various technical aspects which fall beyond the scope of this study, MMA8451Q sensor appeared to be a suitable counterpart with Max21000 gyroscope at the time when the first generation of the SCG-GCG data recorder was designed, while the BMI160 was found a very low-power sensor (990μA with accelerometer and gyroscope in full operation mode) suitable for long-term recording.

This study indicated that it is feasible to implement advanced classification frameworks possibly aiding in the diagnosis of multiple heart conditions. However, smartphones or in general wearable MEMS motion detectors have not been systematically targeted toward the heart measurements, and therefore further validation and risk assessment must be conducted in order to evaluate real end-use of final products based on mechanical motion sensing solutions. For example, in the form of smartphone application developments, medical approvals from authorized organizations such as US Food and Drug Administration (FDA) are required to consider various clinical aspects of mobilephone cardiography. Currently only AliveCor has US FDA approval.

Due to the global availability of smartphones, it could be possible to develop a professional diagnosis system as a part of an efficient global prevention and detection of strategy to deal with heart diseases. However, there is an evident need for further studies such as controlled blinded investigation as well as further clinical considerations for the usage of the envisioned system in limited distribution in the full supervision of trained medical staff, before any such system could be made available.

Another possible area for further clinical investigations is the reliability of the multidimensional MEMS motion detectors as a tool for observing cardiac motion in the context of dual cardiac and respiratory gating in nuclear medicine imaging for a larger subject population. Based on the primary results of this work, MEMS motion sensors are able to give accurate information concerning cardiac and respiratory quiescence phases that are advantageous for cardiac PET imaging. First clinical results with a small patient group revealed images with less image blurring and significantly reduced motion-related inaccuracies. The qualitative and quantitative improvements show promise for the new gating solution and warrant further investigations for oncological and radiotherapy applications.

The three most crucial items to be addressed in the future works are i) increasing the number of subjects considered in clinical trials for MCG-based detection of cardiovascular diseases specifically for data hungry approaches, for example, deep neural networks, that their performance is dependent on the amount of available training data, ii) expanding the potential applications of MCG monitoring for other cardiovascular abnormalities such as various types of arrhythmia, heart failure, cardiac resynchronization therapy, and other diseases, as well as detecting the simultaneous presence of multiple heart diseases in cardiac disease subjects using multilabel learning techniques, and iii) automation of MEMS dual gating system for robust organ's intrafraction variation detection and prediction and quantifying the potential improvements in diagnostic quality resulting from such system with a larger group of patients.

Having a new recording modality which requires as minimum professional knowledge and special equipment as possible is favourable for two major reasons. First, such a recording can be quickly accomplished in every clinic by experts yielding a more accurate diagnosis and treatment plan. Second, this method can further be adapted for self-monitoring outside clinical environment. Self-screening method which could be used directly by the patients themselves outside the hospital environment would be highly beneficial for early interventions. Therefore, a clinically proven and applicable heart monitoring method may facilitate in time diagnosis of cardiac abnormalities resulting in less medical complications, decrease the hospital readmissions and unnecessary emergency department visits, and reduce morbidity and healthcare costs.

The research conducted in the field of mechanocardiography is still characterized by critical standardization issues with health and wellness mobile/wearable devices used in the home and clinical environments. For instance, smartphone applications or equivalent wearables — despite of possible precautions and instructions — require appropriate testing and verification guidance for proper diagnostic quality assurance as well as data storage, processing, safety, and protection plans. Moving forward, it will be demanding to obtain patient safety while supporting innovation in the development and use of mobile medical applications [288].

Chapter 9

Conclusion

In conclusion, this Ph.D. work addressed the globally important issues of detecting cardiovascular disorders, mainly arrhythmia and ischemic heart diseases, with multidimensional MEMS motion sensors embedded into either a small wearable system or a smartphone. Cardiovascular diseases are major causes of death and other comorbidities such as stroke. The outcomes of this study together with related previous investigations in the field acknowledge the capabilities of the miniaturized inertial sensors to reliably identify indications of multiple cardiovascular conditions, without any external complementary equipment such as ECG. Furthermore, primary considerations for motion correction in PET imaging using MEMS dual cardiac and respiratory gating revealed promising outcomes that warrant further investigations in nuclear medicine imaging.

This thesis concentrated closely on four specific tasks as follows:

  I Validating the feasibility and reliability of the non-invasive MEMS motion detectors in MCG and medical imaging applications.

  II New knowledge on exploitation of combined sensory data to establish a theoretical basis for mechanical cardiac monitoring based on linear and rotational aspects of the precordial vibrations.

  III Strengthening sensory data analytics via biomedical signal processing and machine learning techniques to trace heart and lungs intrafraction motions.

  IV New knowledge on clinical applications such as heart disease detection and cardiac PET imaging by adopting related experimental and computational methods for joint SCG-GCG data processing.

Accordingly, the main conclusions of this study are summarized as follows:

- Primary proof of concept experiments demonstrated that MEMS accelerometers and gyroscopes offer reliable and unobtrusive cardiac and respiratory monitoring by automatically tracking the axis of interest and removing data invalidated by subjects' movement.

- A robust signal processing framework can provide reliable and accurate delineation of cardiac mechanics using SCGs and GCGs. Automated and standalone detection of heartbeats from seismocardiograms and gyrocardiograms is feasible by fusion of chest-accelerations and angular velocities in three different orientations, a Hilbert transform, and a complementary adaptive thresholding technique. Furthermore, sensor fusion and unsupervised learning can effectively improve heart rate estimations with wearable/smartphone MCGs.

- Gyrocardiography, a new heart monitoring modality, can indicate rotational characteristics of precordial vibrations induced by myocardial wall movements and left ventricular function. Echocardiography interrogations in Study III revealed that GCG may potentially indicate the timing of opening and closure of heart valves during the systolic and diastolic phases. GCG systolic and diastolic waveform annotations may help in better approximations for the cardiac time intervals.

- Chest-derived translational and angular rates due to cardiac and respiratory motion, measurable by gyroscopes and accelerometers, correlate closely to the heart and lungs movements. Findings of Study IV acknowledge potential benefits of MEMS inertial sensors for cardiac and respiratory gating in PET. MEMS cardiac and respiratory derived signals can provide better mechanical information concerning intrafraction movement changes that cause quantitative inaccuracy in cardiac PET imaging. Clinical experiments with cardiac patients showed a very promising performance for MEMS gating in eliminating image artifacts and preserving PET data statistics for image reconstruction.

- Multidimensional MEMS sensors embedded in smartphones/wearables can be used for detecting indications of cardiovascular diseases. MCG monitoring reliably detects AFib and provides an easy-to-use and accessible concept for AFib screening. Knowledge-based learning as well as machine learning tools detect AFib episodes with high accuracy. Moreover, MCG can aid in the diagnosis of ischemic heart diseases such as cardiomyopathy and coronary artery disease. With advanced machine learning algorithms, it is possible to detect multiple chronic heart diseases when using a smartphone mechanocardiogram.

Acknowledgements

Bibliography

[1] World Health Organiztion. Who/europe. health topics-noncommunicable diseases-cardiovascular diseases-data and statistics.

[2] Dariush Mozaffarian, Emelia J. Benjamin, Alan S. Go, Donna K. Arnett, Michael J. Blaha, Mary Cushman, Sandeep R. Das, Sarah de Ferranti, Jean-Pierre Després, Heather J. Fullerton, Virginia J. Howard, Mark D. Huffman, Carmen R. Isasi, Monik C. Jiménez, Suzanne E. Judd, Brett M. Kissela, Judith H. Lichtman, Lynda D. Lisabeth, Simin Liu, Rachel H. Mackey, David J. Magid, Darren K. McGuire, Emile R. Mohler, Claudia S. Moy, Paul Muntner, Michael E. Mussolino, Khurram Nasir, Robert W. Neumar, Graham Nichol, Latha Palaniappan, Dilip K. Pandey, Mathew J. Reeves, Carlos J. Rodriguez, Wayne Rosamond, Paul D. Sorlie, Joel Stein, Amytis Towfighi, Tanya N. Turan, Salim S. Virani, Daniel Woo, Robert W. Yeh, and Melanie B. Turner. Heart disease and stroke statistics—2016 update. *Circulation*, 133(4):e38–e360, 2016.

[3] Omer T Inan. Wearable sensing of left ventricular function. In *Mobile Health*, pages 265–287. Springer, 2017.

[4] Ya-Li Zheng, Xiao-Rong Ding, Carmen Chung Yan Poon, Benny Ping Lai Lo, Heye Zhang, Xiao-Lin Zhou, Guang-Zhong Yang, Ni Zhao, and Yuan-Ting Zhang. Unobtrusive sensing and wearable devices for health informatics. *IEEE Transactions on Biomedical Engineering*, 61(5):1538–1554, 2014.

[5] Wearable technology: Smart fashion - healthcare community. http://www.cdwcommunit.com/perspectives/expert-perspectives/wearable-technology-smart-fashion. (Accessed on 04/27/2018).

[6] The numbers don't lie: Wearables are the future of healthcare. https://emedcert.com/blog/wearables-statistics-future-of-healthcare. (Accessed on 04/27/2018).

[7] Gustav C Voigt and GOTrLIEB C Friesinger. The use of apexcardiography in the assessment of left ventricular diastolic pressure. *Circulation*, 41(6):1015–1024, 1970.

[8] Michael Fonseca, Mark Allen, David Stern, Jason White, and Jason Kroh. Implantable wireless sensor for pressure measurement within the heart, February 15 2005. US Patent 6,855,115.

[9] U. Meriheinä, M. Juppo, T. Koivisto, M. Pänkäälä, K. Sairanen, and M. Grönholm. Heart monitoring system, March 19 2015. WO Patent App. PCT/IB2014/064,377.

[10] Paul S Auerbach, Jennifer G Baine, Megan L Schott, Amy Greenhaw, Monika G Acharya, and Wade S Smith. Detection of concussion using cranial accelerometry. *Clinical Journal of Sport Medicine*, 25(2):126–132, 2015.

[11] AS Sezen, S Sivaramakrishnan, S Hur, R Rajamani, W Robbins, and Bradley J Nelson. Passive wireless MEMS microphones for biomedical applications. *Journal of Biomechanical Engineering*, 127(6):1030–1034, 2005.

[12] Mallika Bariya, Hnin Yin Yin Nyein, and Ali Javey. Wearable sweat sensors. *Nature Electronics*, 1(3):160, 2018.

[13] Shirley Jones. ECG success: Exercises in ECG interpretation. 2007.

[14] Melanie Nichols, Nick Townsend, Peter Scarborough, Mike Rayner, Jose Leal, Ramon Luengo-Fernandez, et al. European cardiovascular disease statistics, 2012.

[15] Craig T. January, L. Samuel Wann, Joseph S. Alpert, Hugh Calkins, Joaquin E. Cigarroa, Joseph C. Cleveland, Jamie B. Conti, Patrick T. Ellinor, Michael D. Ezekowitz, Michael E. Field, Katherine T. Murray, Ralph L. Sacco, William G. Stevenson, Patrick J. Tchou, Cynthia M. Tracy, and Clyde W. Yancy. 2014 AHA/ACC/HRS Guideline for the Management of Patients With Atrial Fibrillation. *Circulation*, 130(23):e199–e267, 2014.

[16] Joseph A Walsh, Eric J Topol, and Steven R Steinhubl. Novel wireless devices for cardiac monitoring. *Circulation*, 130(7):573–581, 2014.

[17] O.T. Inan, P.-F. Migeotte, Kwang-Suk Park, M. Etemadi, K. Tavakolian, R. Casanella, J. Zanetti, J. Tank, I. Funtova, G.K. Prisk, and M. Di Rienzo. Ballistocardiography and seismocardiography: A review of recent advances. *IEEE Journal of Biomedical and Health Informatics,*, 19(4):1414–1427, July 2015.

[18] Paul A. Iaizzo, editor. *Handbook of Cardiac Anatomy, Physiology, and Devices*. Humana Press Inc, Totowa, NJ, 2005. Springer.

[19] Kenneth P. Roos. 6 - mechanics and force production. In Glenn A. Langer, editor, *The Myocardium (Second Edition)*, pages 235 – 323. Academic Press, San Diego, second edition edition, 1997.

[20] L K Waldman, Y C Fung, and J W Covell. Transmural myocardial deformation in the canine left ventricle. Normal in vivo three-dimensional finite strains. *Circulation Research*, 57(1):152–63, 1985.

[21] F E Rademakers, M B Buchalter, W J Rogers, E A Zerhouni, M L Weisfeldt, J L Weiss, and E P Shapiro. Dissociation between left ventricular untwisting and filling. Accentuation by catecholamines. *Circulation*, 85(4):1572–81, 1992.

[22] W. Croone and P.G.J. Maquet. *On the reason of the movement of the muscles*. Transactions of the American Philosophical Society. American Philosophical Society, 2000.

[23] Partho P. Sengupta, A. Jamil Tajik, Krishnaswamy Chandrasekaran, and Bijoy K. Khandheria. Twist mechanics of the left ventricle: Principles and application. *JACC: Cardiovascular Imaging*, 1(3):366 – 376, 2008.

[24] Theo Arts, Meerbaum Samuel, Robert S Reneman, and Eliot Cordat. Torsion of the left ventricle during the ejection phase in the intact dog. *Cardiovascular Research*, 18(3):183–193, 1984.

[25] Larry A. Taber, Ming Yang, and W.William Podszus. Mechanics of ventricular torsion. *Journal of Biomechanics*, 29(6):745 – 752, 1996.

[26] N B Ingels, G T Daughters, E B Stinson, and E L Alderman. Measurement of midwall myocardial dynamics in intact man by radiography of surgically implanted markers. *Circulation*, 52(5):859–67, 1975.

[27] R. Beyar, C. A. G. Kroeker, H. E. D. J. ter Keurs, M. L. Knudtson, and J. V. Tyberg. An optical device to measure the dynamics of apex rotation of the left ventricle. In *Engineering in Medicine and Biology Society, 1992 14th Annual International Conference of the IEEE*, volume 2, pages 436–438, Oct 1992.

[28] C. A. Gibbons Kroeker, H. E. Ter Keurs, M. L. Knudtson, J. V. Tyberg, and R. Beyar. An optical device to measure the dynamics of apex rotation of the left ventricle. *American Journal of Physiology - Heart and Circulatory Physiology*, 265(4):H1444–H1449, 1993.

[29] Christopher C. Moore, Carlos H. Lugo-Olivieri, Elliot R. McVeigh, and Elias A. Zerhouni. Three-dimensional Systolic Strain Patterns in the Normal Human Left Ventricle: Characterization with Tagged MR Imaging. *Radiology*, 214(2):453–466, 2000. PMID: 10671594.

[30] Karl Isaaz, Aubrey Thompson, Gerard Ethevenot, Jean L. Cloez, Beatrice Brembilla, and Claude Pernot. Doppler echocardiographic measurement of low velocity motion of the left ventricular posterior wall. *The American Journal of Cardiology*, 64(1):66 – 75, 1989.

[31] Yuichi Notomi, Randolph M. Setser, Takahiro Shiota, Maureen G. Martin-Miklovic, Joan A. Weaver, Zoran B. Popović, Hirotsugu Yamada, Neil L. Greenberg, Richard D. White, and James D. Thomas. Assessment of left ventricular torsional deformation by doppler tissue imaging: Validation study with tagged magnetic resonance imaging. *Circulation*, 111(9):1141–1147, 2005.

[32] Brage H. Amundsen, Thomas Helle-Valle, Thor Edvardsen, Hans Torp, Jonas Crosby, Erik Lyseggen, Asbjørn Støylen, Halfdan Ihlen, João A.C. Lima, Otto A. Smiseth, and Stig A. Slørdahl. Noninvasive myocardial strain measurement by speckle tracking echocardiography: Validation against sonomicrometry and tagged magnetic resonance imaging. *Journal of the American College of Cardiology*, 47(4):789 – 793, 2006.

[33] Theodore P. Abraham, Veronica L. Dimaano, and Hsin-Yueh Liang. Role of tissue doppler and strain echocardiography in current clinical practice. *Circulation*, 116(22):2597–2609, 2007.

[34] Emanuela Marcelli, Gianni Plicchi, Laura Cercenelli, and Filippo Bortolami. First experimental evaluation of cardiac apex rotation with an epicardial coriolis force sensor. *American Society for Artificial Internal Organs*, 51(6):696–701, 2005.

[35] E. Marcelli, L. Cercenelli, M. Musaico, P. Bagnoli, M. L. Costantino, R. Fumero, and G. Plicchi. Assessment of cardiac rotation by means of gyroscopic sensors. In *Computers in Cardiology, 2008*, pages 389–392, Sept 2008.

[36] Emanuela Marcelli, Laura Cercenelli, Mario Parlapiano, Roberto Fumero, Paola Bagnoli, Maria Laura Costantino, and Gianni Plicchi. Effect of right ventricular pacing on cardiac apex rotation assessed by a gyroscopic sensor. *American Society for Artificial Internal Organs*, 53(3):304–309, 2007.

[37] Ole-Johannes H.N. Grymyr, Espen W. Remme, Andreas Espinoza, Helge Skulstad, Ole J. Elle, Erik Fosse, and Per S. Halvorsen. Assessment of 3D motion increases the applicability of accelerometers for monitoring left ventricular function. *Interactive CardioVascular and Thoracic Surgery*, 2014.

[38] Katherine C Wu and João AC Lima. Noninvasive imaging of myocardial viability: current techniques and future developments. *Circulation Research*, 93(12):1146–1158, 2003.

[39] John Gorcsan and Hidekazu Tanaka. Echocardiographic assessment of myocardial strain. *Journal of the American College of Cardiology*, 58(14):1401–1413, 2011.

[40] Luigi Brancato, Tristan Weydts, Wouter Oosterlinck, Paul Herijgers, and Robert Puers. Packaging of implantable accelerometers to monitor epicardial and endocardial wall motion. *Biomedical microdevices*, 19(3):52, 2017.

[41] File:wiggers diagram.svg - wikimedia commons. `https://commons.wikimedia.org/wiki/File:Wiggers_Diagram.svg`. (Accessed on 07/06/2018).

[42] Clifford L. Garrard, Arnold M. Weissler, and Harold T. Dodge. The relationship of alterations in systolic time intervals to ejection fraction in patients with cardiac disease. *Circulation*, 42(3):455–462, 1970.

[43] Arnold M. Wiessler, Willard S. Harris, and Clyde D. Schoenfeld. Systolic time intervals in heart failure in man. *Circulation*, 37(2):149–159, 1968.

[44] R.S. Crow, P. Hannan, D. Jacobs, L. Hedquist, and D.M. Salerno. Relationship between seismocardiogram and echocardiogram for events in the cardiac cycle. *American Journal of Noninvasive Cardiology*, 8(1):39–46, 1994. cited By 49.

[45] *Global Atlas on cardiovascular disease prevention and control*. World Health Organization, World Heart Federation,World Stroke Organization, 2011.

[46] Göran K. Hansson. Inflammation, atherosclerosis, and coronary artery disease. *New England Journal of Medicine*, 352(16):1685–1695, 2005. PMID: 15843671.

[47] Allard C. van der Wal and Anton E. Becker. Atherosclerotic plaque rupture – pathologic basis of plaque stability and instability. *Cardiovascular Research*, 41(2):334–344, 1999.

[48] Jacob Fog Bentzon, Fumiyuki Otsuka, Renu Virmani, and Erling Falk. Mechanisms of plaque formation and rupture. *Circulation Research*, 114(12):1852–1866, 2014.

[49] J.H.F. Rudd, E.A. Warburton, T.D. Fryer, H.A. Jones, J.C. Clark, N. Antoun, P. Johnström, A.P. Davenport, P.J. Kirkpatrick, B.N. Arch, J.D. Pickard, and P.L. Weissberg. Imaging atherosclerotic plaque inflammation with [18f]-fluorodeoxyglucose positron emission tomography. *Circulation*, 105(23):2708–2711, 2002.

[50] Peter Leijdekkers and Valérie Gay. A self-test to detect a heart attack using a mobile phone and wearable sensors. In *Computer-Based Medical Systems, 2008. CBMS'08. 21st IEEE International Symposium on*, pages 93–98. IEEE, 2008.

[51] Ziad Sankari and Hojjat Adeli. Heartsaver: a mobile cardiac monitoring system for auto-detection of atrial fibrillation, myocardial infarction, and atrio-ventricular block. *Computers in biology and medicine*, 41(4):211–220, 2011.

[52] Francisco Rincón, Paolo Roberto Grassi, Nadia Khaled, David Atienza, and Donatella Sciuto. Automated real-time atrial fibrillation detection on a wearable wireless sensor platform. In *Engineering in Medicine and Biology Society (EMBC), 2012 Annual International Conference of the IEEE*, pages 2472–2475. IEEE, 2012.

[53] Mustapha M Makki, Georges A Saade, Albert G Altouma, Sami Al-Terkawi, Abdulla Baobeid, and Reza Tafreshi. Acquiring and analyzing electrocardiograms via smartphone to detect cardiovascular abnormalities. In *2014 IEEE-EMBS International Conference on Biomedical and Health Informatics (BHI)*, pages 277–280. IEEE, 2014.

[54] Mahshid Zomorodi Rad, Saeed Rahati Ghuchani, Kambiz Bahaadinbeigy, and Mohammad Mahdi Khalilzadeh. Real time recognition of heart attack in a smart phone. *Acta Informatica Medica*, 23(3):151, 2015.

[55] Priyanka Kakria, NK Tripathi, and Peerapong Kitipawang. A real-time health monitoring system for remote cardiac patients using smartphone and wearable sensors. *International Journal of Telemedicine and Applications*, 2015:8, 2015.

[56] Lis Neubeck, Nicole Lowres, Emelia J Benjamin, S Ben Freedman, Genevieve Coorey, and Julie Redfern. The mobile revolution–using smartphone apps to prevent cardiovascular disease. *Nature Reviews Cardiology*, 12(6):350–360, 2015.

[57] Arpan Pal. Data-driven healthcare using affordable sensing: Screening, diagnosis and therapy. In *Proceedings of the First Workshop on IoT-enabled Healthcare and Wellness Technologies and Systems*, pages 35–35. ACM, 2016.

[58] Mehran M. Sadeghi, David K. Glover, Gregory M. Lanza, Zahi A. Fayad, and Lynne L. Johnson. Imaging atherosclerosis and vulnerable plaque. *Journal of Nuclear Medicine*, 51(Supplement 1):51S–65S, 2010.

[59] Ahmed Tawakol, Raymond Q. Migrino, Gregory G. Bashian, Shahinaz Bedri, David Vermylen, Ricardo C. Cury, Denise Yates, Glenn M. LaMuraglia, Karen Furie, Stuart Houser, Henry Gewirtz, James E. Muller, Thomas J. Brady, and Alan J. Fischman. In vivo 18f-fluorodeoxyglucose positron emission tomography imaging provides a noninvasive measure of carotid plaque inflammation in patients. *Journal of the American College of Cardiology*, 48(9):1818–1824, 2006.

[60] Antti Saraste, Stephan G. Nekolla, and Markus Schwaiger. Cardiovascular molecular imaging: an overview. *Cardiovascular Research*, 83(4):643–652, 2009.

[61] Thomas H. Schindler, Heinrich R. Schelbert, Alessandra Quercioli, and Vasken Dilsizian. Cardiac PET imaging for the detection and monitoring of coronary artery disease and microvascular health. *JACC: Cardiovascular Imaging*, 3(6):623–640, 2010.

[62] W. Bai and M. Brady. Motion correction and attenuation correction for respiratory gated PET images. *IEEE Transactions on Medical Imaging*, 30(2):351–365, Feb 2011.

[63] G. J. Klein, B. W. Reutter, and R. H. Huesman. Non-rigid summing of gated PET via optical flow. *IEEE Transactions on Nuclear Science*, 44(4):1509–1512, Aug 1997.

[64] Tommi Kokki, Hannu T. Sipilä, Mika Teräs, Tommi Noponen, Nicolas Durand-Schaefer, Riku Klén, and Juhani Knuuti. Dual gated PET/CT imaging of small targets of the heart: Method description and testing with a dynamic heart phantom. *Journal of Nuclear Cardiology*, 17(1):71–84, 2009.

[65] Coronary heart disease | national heart, lung, and blood institute (nhlbi). `https://www.nhlbi.nih.gov/health-topics/coronary-heart-disease`. (Accessed on 07/06/2018).

[66] Coronary microvascular disease | national heart, lung, and blood institute (nhlbi). `https://www.nhlbi.nih.gov/health-topics/coronary-microvascular-disease`. (Accessed on 07/06/2018).

[67] Kristian Thygesen, Joseph S Alpert, Harvey D White, Allan S Jaffe, Fred S Apple, Marcello Galvani, Hugo A Katus, L Kristin Newby, Jan Ravkilde, Bernard Chaitman, et al. Universal definition of myocardial infarction: Kristian thygesen, joseph s. alpert and harvey d. white on behalf of the joint esc/accf/aha/whf task force for the redefinition of myocardial infarction. *European Heart Journal*, 28(20):2525–2538, 2007.

[68] Gilles Task Force Members, Montalescot, Udo Sechtem, Stephan Achenbach, Felicita Andreotti, Chris Arden, Andrzej Budaj, and et. al Bugiardini. 2013 esc guidelines on the management of stable coronary artery disease. *European Heart Journal*, 34(38):2949–3003, 2013.

[69] R Gianrossi, R Detrano, D Mulvihill, K Lehmann, P Dubach, A Colombo, D McArthur, and V Froelicher. Exercise-induced ST depression in the diagnosis of coronary artery disease. A meta-analysis. *Circulation*, 80(1):87–98, 1989.

[70] Nora Goldschlager and Jr. Sox, Harold C. The diagnostic and prognostic value of the treadmill exercise test in the evaluation of chest pain, in patients with recent myocardial infarction, and in asymptomatic individuals. *American Heart Journa*, 116(2):523–536, 1988.

[71] Richard A. Wilson, Virinderjit S. Bamrah, Joseph Lindsay, Markus Schwaiger, and Joel Morganroth. Diagnostic accuracy of seismocardiography compared with electrocardiography for the anatomic and physiologic diagnosis of coronary artery disease during exercise testing. *The American Journal of Cardiology*, 71(7):536 – 545, 1993.

[72] Amit Kumar and Christopher P. Cannon. Acute Coronary Syndromes: Diagnosis and Management, Part I. *Mayo Clin Proc*, 84(10):917–938, Oct 2009. 0840917[PII].

[73] Heart attack | national heart, lung, and blood institute (nhlbi). `https://www.nhlbi.nih.gov/health-topics/heart-attack`. (Accessed on 07/06/2018).

[74] Esther Pueyo. Coronary artery disease diagnosis by analysis of ECG depolarization. *Journal of Electrocardiology*, 46(1):27–28, 2013.

[75] Shimon Abboud, Richard J Cohen, Andrew Selwyn, Peter Ganz, Dror Sadeh, and Peter L Friedman. Detection of transient myocardial ischemia by computer analysis of standard and signal-averaged high-frequency electrocardiograms in patients undergoing percutaneous transluminal coronary angioplasty. *Circulation*, 76(3):585–596, 1987.

[76] Shimon Abboud. High-frequency electrocardiogram analysis of the entire QRS in the diagnosis and assessment of coronary artery disease. *Progress in Cardiovascular Diseases*, 35(5):311–328, 1993.

[77] Jonas Pettersson, Olle Pahlm, Elena Carro, Lars Edenbrandt, Michael Ringborn, Leif Sörnmo, Stafford G Warren, and Galen S Wagner. Changes in high-frequency QRS components are more sensitive than st-segment deviation for detecting acute coronary artery occlusion. *Journal of the American College of Cardiology*, 36(6):1827–1834, 2000.

[78] James M Glancy, Clifford J Garratt, DP de Bono, and KL Woods. QT dispersion and mortality after myocardial infarction. *The Lancet*, 345(8955):945–948, 1995.

[79] Kristina H. Haugaa, Marit Kristine Smedsrud, Torkel Steen, Erik Kongsgaard, Jan Pål Loennechen, Terje Skjaerpe, Jens-Uwe Voigt, Rik Willems, Gunnar Smith, Otto A. Smiseth, Jan P. Amlie, and Thor Edvardsen. Mechanical dispersion assessed by myocardial strain in patients after myocardial infarction for risk prediction of ventricular arrhythmia. *JACC: Cardiovascular Imaging*, 3(3):247 – 256, 2010.

[80] Jedrzej Kosiuk, Borislav Dinov, Andreas Bollmann, Emmanuel Koutalas, Andreas Mussigbrodt, Phillipp Sommer, Arash Arya, Sergio Richter, Gerhard Hindricks, and Ole A. Breithardt. Association between ventricular arrhythmias and myocardial mechanical dispersion assessed by strain analysis in patients with nonischemic cardiomyopathy. *Clinical Research in Cardiology*, 104(12):1072–1077, 2015.

[81] Kristina Hermann Haugaa, Thor Edvardsen, Trond P. Leren, Jon Michael Gran, Otto A. Smiseth, and Jan P. Amlie. Left ventricular mechanical dispersion by tissue doppler imaging: a novel approach for identifying high-risk individuals with long qt syndrome. *European Heart Journal*, 30(3):330, 2008.

[82] Swarnava Dey, Swagata Biswas, Arpan Pal, Arijit Mukherjee, Utpal Garain, and Kayapanda Mandana. CAD Patient Classification Using MIMIC-II. In *eHealth 360°*, pages 370–375. Springer, 2017.

[83] Valentin Fuster, Lars E Rydén, Richard W Asinger, David S Cannom, and et al. ACC/AHA/ESC guidelines for the management of patients with atrial fibrillation: executive summary: A report of the american college of cardiology/ american heart association task force on practice guidelines and the european society of cardiology committee for practice guidelines and policy conferences. *Journal of the American College of Cardiology*, 38(4):1231 – 1265, 2001.

[84] Jeff S. Healey, Stuart J. Connolly, Michael R. Gold, Carsten W. Israel, Isabelle C. Van Gelder, Alessandro Capucci, C.P. Lau, Eric Fain, Sean Yang, Christophe Bailleul, Carlos A. Morillo, Mark Carlson, Ellison Themeles, Elizabeth S. Kaufman, and Stefan H. Hohnloser. Subclinical atrial fibrillation and the risk of stroke. *New England Journal of Medicine*, 366(2):120–129, 2012. PMID: 22236222.

[85] Paulus Kirchhof, Stefano Benussi, Dipak Kotecha, Anders Ahlsson, Dan Atar, Barbara Casadei, Manuel Castella, Hans-Christoph Diener, Hein Heidbuchel, Jeroen Hendriks, Gerhard Hindricks, Antonis S Manolis, Jonas Oldgren, Bogdan Alexandru Popescu, Ulrich Schotten, Bart Van Putte, and Panagiotis and Vardas. 2016 ESC Guidelines for the management of atrial fibrillation developed in collaboration with EACTS. *European Heart Journal*, 37(38):2893–2962, 2016.

[86] Adam and Timmis, Nick Townsend, Chris Gale, Rick Grobbee, Nikos Maniadakis, Marcus Flather, Elizabeth Wilkins, Lucy Wright, Rimke Vos, Jeroen Bax, Maxim Blum, Fausto Pinto, and Panos Vardas. European society of cardiology: Cardiovascular disease statistics 2017. *European Heart Journal*, page ehx628, 2017.

[87] Bouwe P. Krijthe, Anton Kunst, Emelia J. Benjamin, Gregory Y.H. Lip, Oscar H. Franco, Albert Hofman, Jacqueline C.M. Witteman, Bruno H. Stricker, and Jan Heeringa. Projections on the number of individuals with atrial fibrillation in the european union, from 2000 to 2060. *European Heart Journal*, 34(35):2746–2751, 2013.

[88] Efstratios I. Charitos, Ulrich Stierle, Paul D. Ziegler, Malte Baldewig, Derek R. Robinson, Hans-Hinrich Sievers, and Thorsten Hanke. A comprehensive evaluation of rhythm monitoring strategies for the detection of atrial fibrillation recurrence: Insights from 647 continuously monitored patients and implications for monitoring after therapeutic interventions. *Circulation*, 2012.

[89] Tommaso Sanna, Hans-Christoph Diener, Rod S Passman, Vincenzo Di Lazzaro, Richard A Bernstein, Carlos A Morillo, Marilyn Mollman Rymer, Vincent Thijs, Tyson Rogers, Frank Beckers, et al. Cryptogenic stroke and underlying atrial fibrillation. *New England Journal of Medicine*, 370(26):2478–2486, 2014.

[90] Peter L Kolominsky-Rabas, Margarete Weber, Olaf Gefeller, Bernhard Neundoerfer, and Peter U Heuschmann. Epidemiology of ischemic stroke subtypes according to toast criteria: incidence, recurrence, and long-term survival in ischemic stroke subtypes: a population-based study. *Stroke*, 32(12):2735–2740, 2001.

[91] Atrial fibrillation - what are the signs and symptoms of atrial fibrillation? | national heart, lung, and blood institute (nhlbi). `https://www.nhlbi.nih.gov/node/3832`. (Accessed on 07/06/2018).

[92] A. John Camm, Paulus Kirchhof, Gregory Y.H. Lip, and et al Schotten. Guidelines for the management of atrial fibrillationThe Task Force for the Management of Atrial Fibrillation of the European Society of Cardiology (ESC). *European Heart Journal*, 31(19):2369–2429, 2010.

[93] S M Vaziri, M G Larson, E J Benjamin, and D Levy. Echocardiographic predictors of nonrheumatic atrial fibrillation. the framingham heart study. *Circulation*, 89(2):724–730, 1994.

[94] Jinseok Lee, Bersain A Reyes, David D McManus, Oscar Maitas, and Ki H Chon. Atrial fibrillation detection using an iphone 4s. *IEEE Transactions on Biomedical Engineering*, 60(1):203–206, 2013.

[95] Alexander Carpenter and Antonio Frontera. Smart-watches: a potential challenger to the implantable loop recorder? *Europace*, 18(6):791–793, 2016.

[96] OT Inan, M Etemadi, RM Wiard, L Giovangrandi, and GTA Kovacs. Robust ballistocardiogram acquisition for home monitoring. *Physiological Measurement*, 30(2):169, 2009.

[97] Jerrett K. Lau, Nicole Lowres, Lis Neubeck, David B. Brieger, Raymond W. Sy, Connor D. Galloway, David E. Albert, and Saul B. Freedman. iphone ECG application for community screening to detect silent atrial fibrillation: A novel technology to prevent stroke. *International Journal of Cardiology*, 165(1):193 – 194, 2013.

[98] Tijn Hendrikx, Mårten Rosenqvist, Per Wester, Herbert Sandström, and Rolf Hörnsten. Intermittent short ECG recording is more effective than 24-hour holter ECG in detection of arrhythmias. *BMC Cardiovascular Disorders*, 14(1):41, Apr 2014.

[99] RG Tieleman, Y Plantinga, D Rinkes, GL Bartels, JL Posma, R Cator, C Hofman, and RP Houben. Validation and clinical use of a novel diagnostic device for screening of atrial fibrillation. *Europace*, 16(9):1291–1295, 2014.

[100] Paddy M Barrett, Ravi Komatireddy, Sharon Haaser, Sarah Topol, Judith Sheard, Jackie Encinas, Angela J Fought, and Eric J Topol. Comparison of 24-hour holter monitoring with 14-day novel adhesive patch electrocardiographic monitoring. *The American Journal of Medicine*, 127(1):95–e11, 2014.

[101] Geoffrey H Tison, José M Sanchez, Brandon Ballinger, Avesh Singh, Jeffrey E Olgin, Mark J Pletcher, Eric Vittinghoff, Emily S Lee, Shannon M Fan, Rachel A Gladstone, et al. Passive detection of atrial fibrillation using a commercially available smartwatch. *JAMA cardiology*, 3(5):409–416, 2018.

[102] Shamim Nemati, Mohammad M Ghassemi, Vaidehi Ambai, Nino Isakadze, Oleksiy Levantsevych, Amit Shah, and Gari D Clifford. Monitoring and detecting atrial fibrillation using wearable technology. In *2016 IEEE 38th Annual International Conference of the Engineering in Medicine and Biology Society (EMBC)*, pages 3394–3397. IEEE, 2016.

[103] Pak-Hei Chan, Chun-Ka Wong, Yukkee C. Poh, Louise Pun, Wangie Wan-Chiu Leung, Yu-Fai Wong, Michelle Man-Ying Wong, Ming-Zher Poh, Daniel Wai-Sing Chu, and Chung-Wah Siu. Diagnostic performance of a smartphone-based photoplethysmographic application for atrial fibrillation screening in a primary care setting. *Journal of the American Heart Association*, 5(7), 2016.

[104] Lian Krivoshei, Stefan Weber, Thilo Burkard, Anna Maseli, Noe Brasier, Michael Kühne, David Conen, Thomas Huebner, Andrea Seeck, and Jens Eckstein. Smart detection of atrial fibrillation. *EP Europace*, 19(5):753–757, 2017.

[105] David D McManus, Jinseok Lee, Oscar Maitas, Nada Esa, Rahul Pidikiti, Alex Carlucci, Josephine Harrington, Eric Mick, and Ki H Chon. A novel application for the detection of an irregular pulse using an iphone 4s in patients with atrial fibrillation. *Heart Rhythm*, 10(3):315–319, 2013.

[106] Nath Zungsontiporn and Mark S Link. Newer technologies for detection of atrial fibrillation. *BMJ*, 363:k3946, 2018.

[107] Steven Ladavich and Behnaz Ghoraani. Rate-independent detection of atrial fibrillation by statistical modeling of atrial activity. *Biomedical Signal Processing and Control*, 18:274 – 281, 2015.

[108] Helmut Pürerfellner, Evgeny Pokushalov, Shantanu Sarkar, Jodi Koehler, Ren Zhou, Lubos Urban, and Gerhard Hindricks. P-wave evidence as a method for improving algorithm to detect atrial fibrillation in insertable cardiac monitors. *Heart Rhythm*, 11(9):1575 – 1583, 2014. Focus Issue: Atrial Fibrillation.

[109] Xiaochuan Du, Nini Rao, Mengyao Qian, Dingyu Liu, Jie Li, Wei Feng, Lixue Yin, and Xu Chen. A novel method for real-time atrial fibrillation detection in electrocardiograms using multiple parameters. *Annals of Noninvasive Electrocardiology*, 19(3):217–225, 2014.

[110] Marta Carrara, Luca Carozzi, Travis J Moss, Marco de Pasquale, Sergio Cerutti, Manuela Ferrario, Douglas E Lake, and J Randall Moorman. Heart rate dynamics distinguish among atrial fibrillation, normal sinus rhythm and sinus rhythm with frequent ectopy. *Physiological Measurement*, 36(9):1873, 2015.

[111] Jinho Park, Sangwook Lee, and Moongu Jeon. Atrial fibrillation detection by heart rate variability in poincare plot. *BioMedical Engineering OnLine*, 8(1):38, Dec 2009.

[112] S. Sarkar, D. Ritscher, and R. Mehra. A detector for a chronic implantable atrial tachyarrhythmia monitor. *IEEE Transactions on Biomedical Engineering*, 55(3):1219–1224, March 2008.

[113] Olli Lahdenoja, Tero Hurnanen, Zuhair Iftikhar, Sami Nieminen, Timo Knuutila, Antti Saraste, Tuomas Kiviniemi, Tuija Vasankari, Juhani Airaksinen, Mikko Pänkäälä, et al. Atrial fibrillation detection via accelerometer and gyroscope of a smartphone. *IEEE Journal of Biomedical and Health Informatics*, 2017.

[114] Phillip P. A. Staniczenko, Chiu Fan Lee, and Nick S. Jones. Rapidly detecting disorder in rhythmic biological signals: A spectral entropy measure to identify cardiac arrhythmias. *Phys. Rev. E*, 79:011915, Jan 2009.

[115] Raúl Alcaraz and José J. Rieta. Sample entropy of the main atrial wave predicts spontaneous termination of paroxysmal atrial fibrillation. *Medical Engineering & Physics*, 31(8):917 – 922, 2009.

[116] Xiaolin Zhou, Hongxia Ding, Benjamin Ung, Emma Pickwell-MacPherson, and Yuanting Zhang. Automatic online detection of atrial fibrillation based on symbolic dynamics and shannon entropy. *BioMedical Engineering OnLine*, 13(1):18, Feb 2014.

[117] Raúl Alcaraz, Daniel Abásolo, Roberto Hornero, and José J. Rieta. Optimal parameters study for sample entropy-based atrial fibrillation organization analysis. *Computer Methods and Programs in Biomedicine*, 99(1):124 – 132, 2010.

[118] Douglas E. Lake and J. Randall Moorman. Accurate estimation of entropy in very short physiological time series: the problem of atrial fibrillation detection in implanted ventricular devices. *American Journal of Physiology-Heart and Circulatory Physiology*, 300(1):H319–H325, 2011. PMID: 21037227.

[119] Morteza Zabihi, Ali Bahrami Rad, Aggelos K Katsaggelos, Serkan Kiranyaz, Susanna Narkilahti, and Moncef Gabbouj. Detection of atrial fibrillation in ecg hand-held devices using a random forest classifier. *Computing in Cardiology*, 44:1, 2017.

[120] Gari D Clifford, Chengyu Liu, Benjamin Moody, Li-wei H Lehman, Ikaro Silva, Qiao Li, AE Johnson, and Roger G Mark. Af classification from a short single lead ecg recording: The physionet computing in cardiology challenge 2017. *Proceedings of Computing in Cardiology*, 44:1, 2017.

[121] Pak-Hei Chan, Chun-Ka Wong, Yukkee C Poh, Louise Pun, Wangie Wan-Chiu Leung, Yu-Fai Wong, Michelle Man-Ying Wong, Ming-Zher Poh, Daniel Wai-Sing Chu, and Chung-Wah Siu. Diagnostic performance of a smartphone-based photoplethysmographic application for atrial fibrillation screening in a primary care setting. *Journal of the American Heart Association*, 5(7):e003428, 2016.

[122] Jerrett K. Lau, Nicole Lowres, Lis Neubeck, David B. Brieger, Raymond W. Sy, Connor D. Galloway, David E. Albert, and Saul B. Freedman. iphone ECG application for community screening to detect silent atrial fibrillation: A novel technology to prevent stroke. *International Journal of Cardiology*, 165(1):193 – 194, 2013.

[123] Nicole Lowres, Lis Neubeck, Glenn Salkeld, Ines Krass, Andrew J McLachlan, Julie Redfern, Alexandra A Bennett, Tom Briffa, Adrian Bauman, Carlos Martinez, et al. Feasibility and cost-effectiveness of stroke prevention through community screening for atrial fibrillation using iphone ecg in pharmacies. the search-af study. *Thromb Haemost*, 111(6):1167–76, 2014.

[124] Lien Desteghe, Zina Raymaekers, Mark Lutin, Johan Vijgen, Dagmara Dilling-Boer, Pieter Koopman, Joris Schurmans, Philippe Vanduynhoven, Paul Dendale, and Hein Heidbuchel. Performance of handheld electrocardiogram devices to detect atrial fibrillation in a cardiology and geriatric ward setting. *EP Europace*, 19(1):29–39, 2016.

[125] Emma Svennberg, Martin Stridh, Johan Engdahl, Faris Al-Khalili, Leif Friberg, Viveka Frykman, and MÃ ̆rten Rosenqvist. Safe automatic one-lead electrocardiogram analysis in screening for atrial fibrillation. *EP Europace*, 19(9):1449–1453, 2017.

[126] Pak-Hei Chan, Chun-Ka Wong, Louise Pun, Yu-Fai Wong, Michelle Man-Ying Wong, Daniel Wai-Sing Chu, and Chung-Wah Siu. Diagnostic performance of an automatic blood pressure measurement device, microlife watchbp home a, for atrial fibrillation screening in a real-world primary care setting. *BMJ open*, 7(6):e013685, 2017.

[127] Christoph Brüser, Jasper Diesel, Matthias DH Zink, Stefan Winter, Patrick Schauerte, and Steffen Leonhardt. Automatic detection of atrial fibrillation in cardiac vibration signals. *IEEE Journal of Biomedical and Health Informatics*, 17(1):162–171, 2013.

[128] Jussi Jaakkola, Samuli Jaakkola, Olli Lahdenoja, Tero Hurnanen, Tero Koivisto, Mikko Pänkäälä, Timo Knuutila, Tuomas O. Kiviniemi, Tuija Vasankari, and K.E. Juhani Airaksinen. Mobile phone detection of atrial fibrillation with mechanocardiography: The MODE-AF study (mobile phone detection of atrial fibrillation). *Circulation*, 2018.

[129] Mohamed Gad-el Hak. MEMS: design and fabrication. *Mechanical engineering series*, 2nd edition, 2006.

[130] Partho P Sengupta, A Jamil Tajik, Krishnaswamy Chandrasekaran, and Bijoy K Khandheria. Twist mechanics of the left ventricle: principles and application. *JACC: Cardiovascular Imaging*, 1(3):366–376, 2008.

[131] Satoshi Nakatani. Left ventricular rotation and twist: why should we learn? *Journal of Cardiovascular Ultrasound*, 19(1):1–6, 2011.

[132] Igor V. Minin and Oleg V. Minin. InTech, Croatia, 2011.

[133] Julian W Gardner, Vijay K Varadan, and Osama O Awadelkarim. *Microsensors, MEMS, and smart devices*, volume 1. Wiley Online Library, 2001.

[134] Amirtaha Taebi and Hansen A Mansy. Time-frequency distribution of seismocardiographic signals: A comparative study. *Bioengineering*, 4(2):32, 2017.

[135] Moises Rivera-Ruiz, Christian Cajavilca, and Joseph Varon. Einthoven's string galvanometer: the first electrocardiograph. *Texas Heart Institute Journal*, 35(2):174, 2008.

[136] J W Gordon. Certain molar movements of the human body produced by the circulation of the blood. *Journal of Anatomy and Physiology*, 11:533–536, 1877.

[137] Isaac Starr, A J Rawson, H A Schroeder, and N R Joseph. Studies on the estimation of cardiac output in man, and of abnormalities in cardiac function. *American Heart Journal*, 18(4):506 –, 1939.

[138] Edward Captain Rubenstein. A review of clinical ballistocardiography. *New England Journal of Medicine*, 247(5):166–173, 1952. PMID: 14941310.

[139] H Mandelbaum and R A Mandelbaum. Clinical findings with the dock ballistocardiograph. *New York Atate Journal of Medicine*, 51(14):1734–8, 1951. PMID: 14853147.

[140] Robert V Elliott, Robert Gay Packard, and Demos T Kyrazis. Acceleration ballistocardiography: design, construction, and application of a new instrument. *Circulation*, 9(2):281–291, 1954.

[141] Patrick Mounsey. Praecordial ballistocardiography. *British heart journal*, 19(2):259, 1957.

[142] B S Bozhenko. Seismocardiography– a new method in the study of functional conditions of the heart. *Terapevticheskii Arkhiv*, 33:55–64, 1961.

[143] J.M. Zanetti and D.M. Salerno. Seismocardiography: a technique for recording precordial acceleration. In *Computer-Based Medical Systems, 1991. Proceedings of the Fourth Annual IEEE Symposium*, pages 4–9, May 1991.

[144] David M. Salerno, John M. Zanetti, Lisa A. Green, Michael R. Mooney, James D. Madison, and Robert A. Van Tassel. Seismocardiographic changes associated with obstruction of coronary blood flow during balloon angioplasty. *The American Journal of Cardiology*, 68(2):201 – 207, 1991.

[145] D M Salerno and J Zanetti. Seismocardiography for monitoring changes in left ventricular function during ischemia. *Chest*, 100(4):991–993, 1991.

[146] J.M. Zanetti, M.O. Poliac, and R.S. Crow. Seismocardiography: waveform identification and noise analysis. In *Computers in Cardiology 1991, Proceedings.*, pages 49–52, Sep 1991.

[147] D M Salerno, J M Zanetti, L a Green, M R Mooney, J D Madison, and R a Van Tassel. Seismocardiographic changes associated with obstruction of coronary blood flow during balloon angioplasty. *The American Journal of Cardiology*, 68(2):201–7, July 1991.

[148] M. Di Rienzo, E. Vaini, P. Castiglioni, G. Merati, P. Meriggi, G. Parati, A. Faini, and F. Rizzo. Wearable seismocardiography: Towards a beat-by-beat assessment of cardiac mechanics in ambulant subjects. *Autonomic Neuroscience*, 178(1-2):50 – 59, 2013.

[149] M. Becker, A.B. Roehl, U. Siekmann, A. Koch, M. de la Fuente, R. Roissant, K. Radermacher, N. Marx, and M. Hein. Simplified detection of myocardial ischemia by seismocardiography. *Herz*, 39(5):586–592, 2014.

[150] F. Khosrow-khavar, K. Tavakolian, A.P. Blaber, J.M. Zanetti, R. Fazel-Rezai, and C. Menon. Automatic annotation of seismocardiogram with high-frequency precordial accelerations. *IEEE Journal of Biomedical and Health Informatics*, 19(4):1428–1434, July 2015.

[151] David M Salerno, John M Zanetti, Liviu C Poliac, Richard S Crow, Peter J Hannan, Kyuhyun Wang, Irvin F Goldenberg, and Robert A Van Tassel. Exercise seismocardiography for detection of coronary artery disease. *American Journal of Noninvasive Cardiology*, 6:321–330, 1992.

[152] M. Etemadi, S. Hersek, J. M. Tseng, N. Rabbani, J. A. Heller, S. Roy, L. Klein, and O. T. Inan. Tracking clinical status for heart failure patients using ballistocardiography and electrocardiography signal features. In *2014 36th Annual International Conference of the IEEE Engineering in Medicine and Biology Society*, pages 5188–5191, Aug 2014.

[153] Omer T Inan, Maziyar Baran Pouyan, Abdul Q Javaid, Sean Dowling, Mozziyar Etemadi, Alexis Dorier, J Alex Heller, A Ozan Bicen, Shuvo Roy, Teresa De Marco, et al. Novel wearable seismocardiography and machine learning algorithms can assess clinical status of heart failure patients. *Circulation: Heart Failure*, 11(1):e004313, 2018.

[154] K. Tavakolian, A.P. Blaber, B. Ngai, and B. Kaminska. Estimation of hemodynamic parameters from seismocardiogram. In *Computing in Cardiology, 2010*, pages 1055–1058, Sept 2010.

[155] A. Q. Javaid, H. Ashouri, S. Tridandapani, and O. T. Inan. Elucidating the hemodynamic origin of ballistocardiographic forces: Toward improved monitoring of cardiovascular health at home. *IEEE Journal of Translational Engineering in Health and Medicine*, 4:1–8, 2016.

[156] P. Castiglioni, P. Meriggi, F. Rizzo, E. Vaini, A. Faini, G. Parati, and M. Di Rienzo. Seismocardiography while sleeping at high altitude. In *2012 Annual International Conference of the IEEE Engineering in Medicine and Biology Society (EMBC)*, pages 3793–3796, Aug 2012.

[157] R. Mukkamala, J. O. Hahn, O. T. Inan, L. K. Mestha, C. S. Kim, H. Töreyin, and S. Kyal. Toward ubiquitous blood pressure monitoring via pulse transit time: Theory and practice. *IEEE Transactions on Biomedical Engineering*, 62(8):1879–1901, Aug 2015.

[158] B. Kajbafzadeh, M. Marzencki, N. Alavi, F. Khosrow-Khavar, K. Tavakolian, C. Menon, and B. Kaminska. Preferred patterns of diastolic timed vibrations for pre-hospitalization treatment of acute coronary ischemia. In *Engineering in Medicine and Biology Society, EMBC, 2011 Annual International Conference of the IEEE*, pages 2480–2483, Aug 2011.

[159] C.A. Wick, Jin-Jyh Su, J.H. McClellan, O. Brand, P.T. Bhatti, A.L. Buice, A.E. Stillman, Xiangyang Tang, and S. Tridandapani. A system for seismocardiography-based identification of quiescent heart phases: Implications for cardiac imaging. *IEEE Transactions on Information Technology in Biomedicine*, 16(5):869–877, Sept 2012.

[160] C. A. Wick, O. T. Inan, J. H. McClellan, and S. Tridandapani. Seismocardiography-based detection of cardiac quiescence. *IEEE Transactions on Biomedical Engineering*, 62(8):2025–2032, Aug 2015.

[161] C A Wick, W F Auffermann, A J Shah, O T Inan, P T Bhatti, and S Tridandapani. Echocardiography as an indication of continuous-time cardiac quiescence. *Physics in Medicine and Biology*, 61(14):5297, 2016.

[162] J. Yao, S. Tridandapani, C. A. Wick, and P. T. Bhatti. Seismocardiography-based cardiac computed tomography gating using patient-specific template identification and detection. *IEEE Journal of Translational Engineering in Health and Medicine*, 5:1–14, 2017.

[163] Mojtaba Jafari Tadi, Eero Lehtonen, Antti Saraste, Jarno Tuominen, Juho Koskinen, Mika Teräs, Juhani Airaksinen, Mikko Pänkäälä, and Tero Koivisto. Gyrocardiography: A new non-invasive monitoring method for the assessment of cardiac mechanics and the estimation of hemodynamic variables. *Scientific Reports*, 7(1):6823, 7 2017.

[164] C. Yang and N. Tavassolian. Combined seismo- and gyro-cardiography: A more comprehensive evaluation of heart-induced chest vibrations. *IEEE Journal of Biomedical and Health Informatics*, PP(99):1–1, 2017.

[165] B. Najafi, K. Aminian, F. Loew, Y. Blanc, and P. A. Robert. Measurement of stand-sit and sit-stand transitions using a miniature gyroscope and its application in fall risk evaluation in the elderly. *IEEE Transactions on Biomedical Engineering*, 49(8):843–851, Aug 2002.

[166] O. Lahdenoja, T. Koivisto, M. J. Tadi, Z. Iftikhar, T. Hurnanen, T. Vasankari, T. Kiviniemi, J. Airaksinen, and M. Pänkäälä. A smartphone-only solution for detecting indications of acute myocardial infarction. In *2017 IEEE EMBS International Conference on Biomedical Health Informatics (BHI)*, pages 197–200, Feb 2017.

[167] Pierre-François Migeotte, Vivana Mucci, Quentin Delière, Laurent Lejeune, and Philippe van de Borne. *Multi-dimensional Kineticardiography a New Approach for Wearable Cardiac Monitoring Through Body Acceleration Recordings*. Springer International Publishing, Cham, 2016.

[168] Sami Nurmi, Tarja Saaresranta, Tero Koivisto, Ulf Meriheinä, Lauri Palva, et al. Validation of an accelerometer based BCG method for sleep analysis. *Aalto University*, Master's Thesis, 2016.

[169] J. Hernandez, Yin Li, J.M. Rehg, and R.W. Picard. Bioglass: Physiological parameter estimation using a head-mounted wearable device. In *2014 EAI 4th International Conference on Wireless Mobile Communication and Healthcare (Mobihealth)*, pages 55–58, Nov 2014.

[170] J. Hernandez, D.J. McDuff, and R.W. Picard. Bioinsights: Extracting personal data from still wearable motion sensors. In *2015 IEEE 12th International Conference on Wearable and Implantable Body Sensor Networks (BSN)*, pages 1–6, June 2015.

[171] Wenyan Jia, Yuecheng Li, Yicheng Bai, Zhi-Hong Mao, Mingui Sun, and Qi Zhao. Estimation of heart rate from a chest-worn inertial measurement unit. In *Bioelectronics and Bioinformatics (ISBB), 2015 International Symposium on*, pages 148–151, Oct 2015.

[172] Stefan Hyler, Andreas Espinoza, Helge Skulstad, Erik Fosse, and Per Steinar Halvorsen. Left ventricular function can be continuously monitored with an epicardially attached accelerometer sensor. *European Journal of Cardio-Thoracic Surgery*, 46(2):313–320, 2014.

[173] C. Bräser, K. Stadlthanner, S. de Waele, and S. Leonhardt. Adaptive beat-to-beat heart rate estimation in ballistocardiograms. *IEEE Transactions on Information Technology in Biomedicine*, 15(5):778–786, Sept 2011.

[174] C Brüser, S Winter, and S Leonhardt. Robust inter-beat interval estimation in cardiac vibration signals. *Physiological Measurement*, 34(2):123, 2013.

[175] J. Paalasmaa, H. Toivonen, and M. Partinen. Adaptive heartbeat modelling for beat-to-beat heart rate measurement in ballistocardiograms. *Biomedical and Health Informatics, IEEE Journal of*, PP(99):1–1, 2014.

[176] M. A. García-González, A. Argelagós-Palau, M. Fernández-Chimeno, and J. Ramos-Castro. A comparison of heartbeat detectors for the seismocardiogram. In *Computing in Cardiology Conference (CinC), 2013*, pages 461–464, Sept 2013.

[177] Carlos Alvarado-Serrano, Pablo Samuel Luna-Lozano, and Ramon Pallàs-Areny. An algorithm for beat-to-beat heart rate detection from the BCG based on the continuous spline wavelet transform. *Biomedical Signal Processing and Control*, 27:96 – 102, 2016.

[178] Keya Pandia, Omer T Inan, Gregory T A Kovacs, and Laurent Giovangrandi. Extracting respiratory information from seismocardiogram signals acquired on the chest using a miniature accelerometer. *Physiological Measurement*, 33(10):1643, 2012.

[179] J. Ramos-Castro, J. Moreno, H. Miranda-Vidal, M.A. Garcia-Gonzalez, M. Fernandez-Chimeno, G. Rodas, and L. Capdevila. Heart rate variability analysis using a seismocardiogram signal. In *Engineering in Medicine and Biology Society (EMBC), 2012 Annual International Conference of the IEEE*, pages 5642–5645, Aug 2012.

[180] A. D. Wiens, M. Etemadi, S. Roy, L. Klein, and O. T. Inan. Toward continuous, noninvasive assessment of ventricular function and hemodynamics: Wearable ballistocardiography. *IEEE Journal of Biomedical and Health Informatics*, 19(4):1435–1442, July 2015.

[181] Abdul Q. Javaid, N.Forrest Fesmire, Mary A. Weitnauer, and Omer T. Inan. Towards robust estimation of systolic time intervals using head-to-foot and dorso-ventral components of sternal acceleration signals. In *2015 IEEE 12th International Conference on Wearable and Implantable Body Sensor Networks (BSN)*, pages 1–5, June 2015.

[182] Mojtaba JafariTadi, Tero Koivisto, Mikko Pänkäälä, Ari Paasio, Timo Knuutila, Mika Teräs, and Pekka Hänninen. A new algorithm for segmentation of cardiac quiescent phases and cardiac time intervals using seismocardiography. In *Proc. SPIE, Sixth International Conference on Graphic and Image Processing (ICGIP)*, volume 9443, pages 94432K–94432K–7, 2015.

[183] Farzad Khosrow-Khavar, Kouhyar Tavakolian, Andrew Blaber, and Carlo Menon. Automatic and robust delineation of the fiducial points of the seismocardiogram signal for noninvasive estimation of cardiac time intervals. *IEEE Transactions on Biomedical Engineering*, 64(8):1701–1710, 2017.

[184] Marco Di Rienzo, Emanuele Vaini, and Prospero Lombardi. An algorithm for the beat-to-beat assessment of cardiac mechanics during sleep on earth and in microgravity from the seismocardiogram. *Scientific Reports*, 7(1):15634, 2017.

[185] Tero Hurnanen, Matti Kaisti, Mojtaba Jafari Tadi, Matti Vähä-Heikkilä, Sami Nieminen, Zuhair Iftikhar, Mikko Paukkunen, Mikko Pänkäälä, and Tero Koivisto. Heartbeat detection using multidimensional cardiac motion signals and dynamic balancing. In *EMBEC & NBC 2017*, pages 896–899, Singapore, 2018. Springer Singapore.

[186] D. Friedrich, X.L. Aubert, H. Fuhr, and A. Brauers. Heart rate estimation on a beat-to-beat basis via ballistocardiography - a hybrid approach. In *2010 Annual International Conference of the IEEE Engineering in Medicine and Biology Society (EMBC)*, pages 4048–4051, Aug 2010.

[187] J. H. Shin, B. H. Choi, Y. G. Lim, D. U. Jeong, and K. S. Park. Automatic ballistocardiogram (BCG) beat detection using a template matching approach. In *30th Annual International Conference of the IEEE Engineering in Medicine and Biology Society,*, pages 1144–1146, Aug 2008.

[188] H. Ashouri, S. Hersek, and O. T. Inan. Universal pre-ejection period estimation using seismocardiography: Quantifying the effects of sensor placement and regression algorithms. *IEEE Sensors Journal*, 18(4):1665–1674, Feb 2018.

[189] Mario Malcangi, Hao Quan, Emanuele Vaini, Prospero Lombardi, and Marco Di Rienzo. *Applying the EFuNN Evolving Paradigm to the Recognition of Artefactual Beats in Continuous Seismocardiogram Recordings*, pages 256–264. Springer International Publishing, Cham, 2017.

[190] Chenghao Zhu and Feng Tian. An ECG detection algorithm using wavelet and autocorrelation transform. In *2013 International Conference on Wireless Communications Signal Processing (WCSP)*, pages 1–6, Oct 2013.

[191] M. Nakano, T. Konishi, S. Izumi, H. Kawaguchi, and M. Yoshimoto. Instantaneous heart rate detection using short-time autocorrelation for wearable healthcare systems. In *2012 Annual International Conference of the IEEE Engineering in Medicine and Biology Society (EMBC)*, pages 6703–6706, Aug 2012.

[192] Janusz Jezewski, Dawid Roj, Janusz Wrobel, and Krzysztof Horoba. A novel technique for fetal heart rate estimation from doppler ultrasound signal. *BioMedical Engineering OnLine*, 10(1):92, 2011.

[193] J. Wahlstrom, I. Skog, P. Handel, F. Khosrow-khavar, K. Tavakolian, P. K. Stein, and A. Nehorai. A Hidden Markov Model for Seismocardiography. *IEEE Transactions on Biomedical Engineering*, PP(99):1–1, 2017.

[194] W. Sandham, D. Hamilton, A. Fisher, Wei Xu, and M. Conway. Multiresolution wavelet decomposition of the seismocardiogram. *IEEE Transactions on Signal Processing*, 46(9):2541–2543, Sep 1998.

[195] C. H. Antink, C. Brüser, and S. Leonhardt. Multimodal sensor fusion of cardiac signals via blind deconvolution: A source-filter approach. In *Computing in Cardiology Conference (CinC), 2014*, pages 805–808, Sept 2014.

[196] C. Brüser, J. M. Kortelainen, S. Winter, M. Tenhunen, J. Pärkkä, and S. Leonhardt. Improvement of force-sensor-based heart rate estimation using multichannel data fusion. *IEEE Journal of Biomedical and Health Informatics*, 19(1):227–235, Jan 2015.

[197] Christoph Hoog Antink, Christoph Brüser, and Steffen Leonhardt. Detection of heart beats in multimodal data: a robust beat-to-beat interval estimation approach. *Physiological Measurement*, 36(8):1679, 2015.

[198] Y. Zhu, V. F. S. Fook, E. H. Jianzhong, J. Maniyeri, C. Guan, H. Zhang, E. P. Jiliang, and J. Biswas. Heart rate estimation from FBG sensors using cepstrum analysis and sensor fusion. In *2014 36th Annual International Conference of the IEEE Engineering in Medicine and Biology Society (EMBC)*, pages 5365–5368, Aug 2014.

[199] S. Šprager and D. Zazula. Optimization of heartbeat detection in fiber-optic unobtrusive measurements by using maximum a posteriori probability estimation. *IEEE Journal of Biomedical and Health Informatics*, 18(4):1161–1168, July 2014.

[200] Won Kyu Lee, Heenam Yoon, Chungmin Han, Kwang Min Joo, and Kwang Suk Park. Physiological signal monitoring bed for infants based on load-cell sensors. *Sensors*, 16(3):409, 2016.

[201] Matthias Daniel Zink, Christoph Brüser, Björn-Ole Stüben, Andreas Napp, Robert Stöhr, Steffen Leonhardt, Nikolaus Marx, Karl Mischke, Jörg B Schulz, and Johannes Schiefer. Unobtrusive nocturnal heartbeat monitoring by a ballistocardiographic sensor in patients with sleep disordered breathing. *Scientific Reports*, 7(1):13175, 2017.

[202] Tobias Wartzek, Christoph Bruser, Marian Walter, and Steffen Leonhardt. Robust sensor fusion of unobtrusively measured heart rate. *IEEE Journal of Biomedical and Health Informatics*, 18(2):654–660, 2014.

[203] Robert Dean Allison, EL Holmes, and J Nyboer. Volumetric dynamics of respiration as measured by electrical impedance plethysmography. *Journal of applied physiology*, 19(1):166–173, 1964.

[204] LH Hamilton, JD Beard, RE Carmean, and RC Kory. An electrical impedance ventilometer to quantitate tidal volume and ventilation. *Medical Research Engineering*, 6(1):11–16, 1967.

[205] S Hoffman, R Jedeikin, and D Atlas. Respiratory monitoring with a new impedance plethysmograph. *Anaesthesia*, 41(11):1139–1142, 1986.

[206] Kumar Ashutosh, ROBERT Gilbert, J HOWLAND Auchincloss, J Erlebacher, and DAVID Peppi. Impedance pneumograph and magnetometer methods for monitoring tidal volume. *Journal of Applied Physiology*, 37(6):964–966, 1974.

[207] Robert E. Barrow PhD and PhD Arthur J. Vorwald MD. Capacitance respirometry. *Archives of Environmental Health: An International Journal*, 19(4):579–585, 1969. PMID: 5823005.

[208] I Eriksson, L Berggren, and S Hallgren. CO2 production and breathing pattern during invasive and non-invasive respiratory monitoring. *Acta Anaesthesiologica Scandinavica*, 30(6):438–443, 1986.

[209] CI Franks, BH Brown, and DM Johnston. Contactless respiration monitoring of infants. *Medical and Biological Engineering*, 14(3):306–312, 1976.

[210] Anders Johansson and PÅ Öberg. Estimation of respiratory volumes from the photoplethysmographic signal. Part I: experimental results. *Medical & Biological Engineering & Computing*, 37(1):42–47, 1999.

[211] Achim Schweikard, Greg Glosser, Mohan Bodduluri, Martin J Murphy, and John R Adler. Robotic motion compensation for respiratory movement during radiosurgery. *Computer Aided Surgery*, 5(4):263–277, 2000.

[212] Andrew Bates, Martin J Ling, Janek Mann, and DK Arvind. Respiratory rate and flow waveform estimation from tri-axial accelerometer data. In *2010 International Conference on Body Sensor Networks (BSN)*, pages 144–150. IEEE, 2010.

[213] M. Folke, L. Cernerud, M. Ekström, and B. Hök. Critical review of non-invasive respiratory monitoring in medical care. *Medical and Biological Engineering and Computing*, 41(4):377–383, Jul 2003.

[214] James C Lin. Noninvasive microwave measurement of respiration. *Proceedings of the IEEE*, 63(10):1530–1530, 1975.

[215] Sadek A Nehmeh and Yusuf E Erdi. Respiratory motion in positron emission tomography/computed tomography: a review. In *Seminars in Nuclear Medicine*, volume 38, pages 167–176. Elsevier, 2008.

[216] T Koivumäki, M Vauhkonen, J Teuho, M Teräs, and M A Hakulinen. Bioimpedance-based respiratory gating method for oncologic positron emission tomography (PET) imaging with first clinical results. *Journal of Physics: Conference Series*, 434(1):012037, 2013.

[217] S. A. Nehmeh, Y. E. Erdi, T. Pan, E. Yorke, G. S. Mageras, K. E. Rosenzweig, H. Schoder, H. Mostafavi, O. Squire, A. Pevsner, S. M. Larson, and J. L. Humm. Quantitation of respiratory motion during 4D PET/CT acquisition. *Medical Physics*, 31(6):1333–1338, 2004.

[218] T Koivumäki, M Vauhkonen, J T Kuikka, and M A Hakulinen. Bioimpedance-based measurement method for simultaneous acquisition of respiratory and cardiac gating signals. *Physiological Measurement*, 33(8):1323, 2012.

[219] Piotr J. Slomka, Tinsu Pan, and Guido Germano. Recent advances and future progress in PET instrumentation. *Seminars in Nuclear Medicine*, 46(1):5 – 19, 2016. Recent Advances and Future Perspectives in Nuclear Medicine.

[220] Michael Riedel, N Navab, and A Moller. Respiratory motion estimation: tests and comparison of different sensors. *Interdisciplinary Project. Technische Universität München Fakultät für Informatik, Germany*, 2006.

[221] Tiezhi Zhang, Harry Keller, Matthew J O'brien, Thomas R Mackie, and Bhudatt Paliwal. Application of the spirometer in respiratory gated radiotherapy. *Medical physics*, 30(12):3165–3171, 2003.

[222] Audrey Pepin, Joel Daouk, Pascal Bailly, Sebastien Hapdey, and Marc-Etienne Meyer. Management of respiratory motion in PET/computed tomography: the state of the art. *Nuclear Medicine Communications*, 35(2):113, 2014.

[223] Gatingbrief. https://www.varian.com/sites/default/files/resource_attachments/RPMSystemProductBrief_RAD5614B_August2007.pdf. (Accessed on 05/09/2018).

[224] Mojtaba Jafari Tadi, Tero Koivisto, Mikko Pänkäälä, and Ari Paasio. Accelerometer-based method for extracting respiratory and cardiac gating information for dual gating during nuclear medicine imaging. *International Journal of Biomedical Imaging*, 2014(690124):1–11, 2014.

[225] Mojtaba Jafari Tadi, Jarmo Teuho, Eero Lehtonen, Antti Saraste, Mikko Pänkäälä, Mika Teräs, and Teroi Koivisto. MEMS Gating: A new dual gating technique for eliminating motion-related inaccuracies in PET imaging. In *2016 IEEE Nuclear Science Symposium and Medical Imaging Conference (NSS/MIC)*, pages 1–4, Nov 2016.

[226] Mojtaba Jafari Tadi, Eero Lehtonen, Jarmo Teuho, Antti Saraste, Mikko Pänkäälä, Mika Teräs, and Tero Koivisto. A miniaturized MEMS motion processing system for nuclear medicine imaging applications. In *Computing in Cardiology, 2016*, volume 43, pages 1–4, 2016.

[227] J. Martin Bland and DouglasG. Altman. Statistical methods for assessing agreement between two methods of clinical measurement. *The Lancet*, 327(8476):307 – 310, 1986. Originally published as Volume 1, Issue 8476.

[228] Petros Nihoyannopoulos and Joseph Kisslo. *Echocardiography*. Springer, 2009.

[229] Jerrold T Bushberg. *The Essential Physics of Medical Imaging*. Lippincott Williams & Wilkins, 2002.

[230] Holly Geyer, Giuseppe Caracciolo, Haruhiko Abe, Susan Wilansky, Scipione Carerj, Federico Gentile, Hans-Joachim Nesser, Bijoy Khandheria, Jagat Narula, and Partho P Sengupta. Assessment of myocardial mechanics using speckle tracking echocardiography: fundamentals and clinical applications. *Journal of the American Society of Echocardiography*, 23(4):351–369, 2010.

[231] Michael Dandel, Hans Lehmkuhl, Christoph Knosalla, Nino Suramelashvili, and Roland Hetzer. Strain and strain rate imaging by echocardiography - basic concepts and clinical applicability. *Current Cardiology Reviews*, 5(2):133–148, 2009.

[232] Adam A Ghotbi, Andreas Kjær, and Philip Hasbak. comparison of PET rubidium-82 with conventional SPECT myocardial perfusion imaging. *Clinical Physiology and Functional Imaging*, 34(3):163–170, 2014.

[233] Piotr J. Slomka, Tinsu Pan, and Guido Germano. Imaging moving heart structures with PET. *Journal of Nuclear Cardiology*, 23(3):486–490, 2016.

[234] Dale L Bailey, David W Townsend, Peter E Valk, and Michael N Maisey. *Positron Emission Tomography*. Springer, 2005.

[235] Advances in PET/CT technology | imaging technology news. https://www.itnonline.com/article/advances-petct-technology. (Accessed on 05/16/2018).

[236] Adam Alessio and Paul Kinahan. PET image reconstruction. *Nuclear Medicine*, 1:1–22, 2006.

[237] Andrew J Reader and Jeroen Verhaeghe. 4D image reconstruction for emission tomography. *Physics in Medicine & Biology*, 59(22):R371, 2014.

[238] SA Nehmeh, YE Erdi, T Pan, A Pevsner, KE Rosenzweig, E Yorke, GS Mageras, H Schoder, Phil Vernon, O Squire, et al. Four-dimensional (4D) PET/CT imaging of the thorax. *Medical Physics*, 31(12):3179–3186, 2004.

[239] Sadek A Nehmeh, Yusuf E Erdi, Kenneth E Rosenzweig, Heiko Schoder, Steve M Larson, Olivia D Squire, and John L Humm. Reduction of respiratory motion artifacts in PET imaging of lung cancer by respiratory correlated dynamic PET: methodology and comparison with respiratory gated PET. *Journal of Nuclear Medicine*, 44(10):1644–1648, 2003.

[240] Paul J Keall, Gig S Mageras, James M Balter, Richard S Emery, Kenneth M Forster, Steve B Jiang, Jeffrey M Kapatoes, Daniel A Low, Martin J Murphy, Brad R Murray, et al. The management of respiratory motion in radiation oncology report of AAPM task group 76. *Medical Physics*, 33(10):3874–3900, 2006.

[241] SA Nehmeh, YE Erdi, CC Ling, KE Rosenzweig, OD Squire, LE Braban, E Ford, K Sidhu, GS Mageras, SM Larson, et al. Effect of respiratory gating on reducing lung motion artifacts in PET imaging of lung cancer. *Medical Physics*, 29(3):366–371, 2002.

[242] Valentino Bettinardi, Maria Picchio, Nadia Di Muzio, Luigi Gianolli, Maria Carla Gilardi, and Cristina Messa. Detection and compensation of organ/lesion motion using 4d-PET/ct respiratory gated acquisition techniques. *Radiotherapy and Oncology*, 96(3):311–316, 2010.

[243] Inger Havsteen, Anders Ohlhues, Kristoffer H Madsen, Janus Damm Nybing, Hanne Christensen, and Anders Christensen. Are movement artifacts in magnetic resonance imaging a real problem? a narrative review. *Frontiers in Neurology*, 8:232, 2017.

[244] Benoit Desjardins and Ella A Kazerooni. ECG-gated cardiac CT. *American Journal of Roentgenology*, 182(4):993–1010, 2004.

[245] Asit K Paul and Hani A Nabi. Gated myocardial perfusion SPECT: basic principles, technical aspects, and clinical applications. *Journal of Nuclear Medicine Technology*, 32(4):179–187, 2004.

[246] William P Shuman, Kelley R Branch, Janet M May, Lee M Mitsumori, David W Lockhart, Theodore J Dubinsky, Bill H Warren, and James H Caldwell. Prospective versus retrospective ECG gating for 64-detector CT of the coronary arteries: comparison of image quality and patient radiation dose. *Radiology*, 248(2):431–437, 2008.

[247] James P Earls. How to use a prospective gated technique for cardiac CT. *Journal of Cardiovascular Computed Tomography*, 3(1):45–51, 2009.

[248] Jeffrey J Goldberger and Jason Ng. *Practical signal and image processing in clinical cardiology*. Springer, 2010.

[249] J Qin, LY Liu, Y Fang, JM Zhu, Z Wu, KS Zhu, JS Zhang, and H Shan. 320-detector CT coronary angiography with prospective and retrospective electrocardiogram gating in a single heartbeat: comparison of image quality and radiation dose. *The British Journal of Radiology*, 85(1015):945–951, 2012.

[250] Mohammad Dawood, Florian Büther, Norbert Lang, Otmar Schober, and Klaus P Schäfers. Respiratory gating in positron emission tomography: A quantitative comparison of different gating schemes. *Medical Physics*, 34(7):3067–3076, 2007.

[251] M Dawood, T Kösters, M Fieseler, F Büther, X Jiang, and KP Schäfers. Motion correction on dual ECG and respiratory gated 3D cardiac PET/CT data. https://slideplayer.com/slide/8946827/. (Accessed on 07/01/2018).

[252] Kouhyar Tavakolian. *Characterization and Analysis of seismocardiogram for estimation of hemodynamic parameters*. PhD thesis, Simon Fraser University, 2010.

[253] Jarno Tuominen, Eero Lehtonen, Mojtaba Jafari Tadi, Juho Koskinen, Mikko Pänkäälä, and Tero Koivisto. A miniaturized low power biomedical sensor node for clinical research and long term monitoring of cardiovascular signals. In *2017 IEEE International Symposium on Circuits and Systems (ISCAS)*, pages 1–4. IEEE, 2017.

[254] K.R. Pandia, S. Ravindran, and E.R. Cole. Motion/activity, heart-rate and respiration from a single chest-worn sensor, circuits, devices, processes and systems, March 17 2011. US Patent App. 12/861,882.

[255] C. Yang and N. Tavassolian. Motion noise cancellation in seismocardiographic monitoring of moving subjects. In *2015 IEEE Biomedical Circuits and Systems Conference (BioCAS)*, pages 1–4, Oct 2015.

[256] Bin Yang, Yonggui Dong, Chunyang Yu, and Zhongjie Hou. Singular spectrum analysis window length selection in processing capacitive captured biopotential signals. *IEEE Sensors Journal*, 16(19):7183–7193, 2016.

[257] Robert Vautard, Pascal Yiou, and Michael Ghil. Singular-spectrum analysis: A toolkit for short, noisy chaotic signals. *Physica D: Nonlinear Phenomena*, 58(1):95 – 126, 1992.

[258] Nina Golyandina and Anatoly Zhigljavsky. *Singular spectrum analysis for time series*. Springer Science & Business Media, 2013.

[259] Milan Stork. Hilbert-huang transform and its applications in engineering and biomedical signal analysis. In *Proceedings of the 16th WSEAS International Conference on Circuits, Recent Researches in Circuits and Systems*, pages 14–17, July 2012.

[260] D. Benitez, P.A. Gaydecki, A. Zaidi, and A.P. Fitzpatrick. The use of the Hilbert transform in ECG signal analysis . *Computers in Biology and Medicine*, 31(5):399 – 406, 2001.

[261] D S Benitez, P A Gaydecki, A Zaidi, and A P Fitzpatrick. A new QRS detection algorithm based on the Hilbert transform. In *Computers in Cardiology (Cinc), 2000*, pages 379–382, 2000.

[262] Hossein Rabbani, M Parsa Mahjoob, E Farahabadi, and A Farahabadi. R Peak Detection in Electrocardiogram Signal Based on an Optimal Combination of Wavelet Transform, Hilbert Transform, and Adaptive Thresholding. *Journal of Medical Signals and Sensors*, 1(2):91–98, 2011.

[263] Mojtaba Jafari Tadi, Eero Lehtonen, Tero Hurnanen, Juho Koskinen, Jonas Eriksson, Mikko Pänkäälä, Mika Teräs, and Tero Koivisto. A real-time approach for heart rate monitoring using a hilbert transform in seismocardiograms. *Physiological Measurement*, 37(11):1885, 2016.

[264] Lawrence Marple. Computing the discrete-time" analytic" signal via fft. *IEEE Transactions on Signal Processing*, 47(9):2600–2603, 1999.

[265] M. Nilsson, M. Dahl, and I. Claesson. The successive mean quantization transform. In *IEEE International Conference on Acoustics, Speech, and Signal Processing, 2005. Proceedings.*, volume 4, pages iv/429–iv/432 Vol. 4, March 2005.

[266] Jiapu Pan and Willis J. Tompkins. A Real-Time QRS Detection Algorithm. *IEEE Transactions on Biomedical Engineering*, BME-32(3):230–236, March 1985.

[267] Felix Scholkmann, Jens Boss, and Martin Wolf. An efficient algorithm for automatic peak detection in noisy periodic and quasi-periodic signals. *Algorithms*, 5(4):588–603, 2012.

[268] Timothy M Seese, Hiroaki Harasaki, Gerald M Saidel, and Charles R Davies. Characterization of tissue morphology, angiogenesis, and temperature in the adaptive response of muscle tissue to chronic heating. *Laboratory investigation; a journal of technical methods and pathology*, 78(12):1553–1562, 1998.

[269] Tero Koivisto, Mikko Pänkäälä, Tero Hurnanen, Tuija Vasankari, Tuomas Kiviniemi, Antti Saraste, and Juhani Airaksinen. Automatic detection of atrial fibrillation using MEMS accelerometer. In *Computing in Cardiology Conference (CinC), 2015*, pages 829–832. IEEE, 2015.

[270] Tero Hurnanen, Eero Lehtonen, Mojtaba Jafari Tadi, Tom Kuusela, Tuomas Kiviniemi, Antti Saraste, Tuija Vasankari, Juhani Airaksinen, Tero Koivisto, and Mikko Pankaala. Automated detection of atrial fibrillation based on time-frequency analysis of seismocardiograms. *IEEE journal of biomedical and health informatics*, 2017.

[271] Navin Chatlani and John J Soraghan. Local binary patterns for 1-D signal processing. In *Signal Processing Conference, 2010 18th European*, pages 95–99. IEEE, 2010.

[272] Timo Ojala, Matti Pietikainen, and Topi Maenpaa. Multiresolution gray-scale and rotation invariant texture classification with local binary patterns. *IEEE Transactions on Pattern Analysis and Machine Intelligence*, 24(7):971–987, 2002.

[273] Timo Ahonen, Abdenour Hadid, and Matti Pietikainen. Face description with local binary patterns: Application to face recognition. *IEEE Transactions on Pattern Analysis and Machine Intelligence*, 28(12):2037–2041, 2006.

[274] Gordon CS Smith, Shaun R Seaman, Angela M Wood, Patrick Royston, and Ian R White. Correcting for optimistic prediction in small data sets. *American journal of epidemiology*, 180(3):318–324, 2014.

[275] M. Kaisti, M. J. Tadi, O. Lahdenoja, T. Hurnanen, A. Saraste, M. Pänkäälä, and T. Koivisto. Stand-alone heartbeat detection in multidimensional mechanocardiograms. *IEEE Sensors Journal*, pages 1–1, 2018.

[276] Hugues Bader, Stephane Garrigue, Stephane Lafitte, Sylvain Reuter, Pierre Jaïs, Michel Haïssaguerre, Jacques Bonnet, Jacques Clementy, and Raymond Roudaut. Intra-left ventricular electromechanical asynchrony: a new independent predictor of severe cardiac events in heart failure patients. *Journal of the American College of Cardiology*, 43(2):248–256, 2004.

[277] Yuji Tsutsui, Daisuke Kidera, Takafumi Taniguchi, Go Akamatsu, Isao Komiya, Yoshiyuki Umezu, Yoshiyuki Kitamura, Shingo Baba, and Masayuki Sasaki. Accuracy of amplitude-based respiratory gating for PET/CT in irregular respirations. *Annals of Nuclear Medicine*, 28(8):770–779, 2014.

[278] Ron Kohavi and George H John. Wrappers for feature subset selection. *Artificial Intelligence*, 97(1-2):273–324, 1997.

[279] Zuhair Iftikhar, Olli Lahdenoja, Mojtaba Jafari Tadi, Tero Hurnanen, Tuija Vasankari, Tuomas Kiviniemi, Juhani Airaksinen, Tero Koivisto, and Mikko Pänkäälä. Multiclass classifier based cardiovascular condition detection using smartphone mechanocardiography. *Scientific Reports*, 8(1):9344, 2018.

[280] J. Lee Garvey, Jessica Zegre-Hemsey, Richard Gregg, and Jonathan R. Studnek. Electrocardiographic diagnosis of st segment elevation myocardial infarction: An evaluation of three automated interpretation algorithms. *Journal of Electrocardiology*, 49(5):728 – 732, 2016.

[281] Juul Achten and Asker E Jeukendrup. Heart rate monitoring. *Sports Medicine*, 33(7):517–538, 2003.

[282] James A.J. Heathers. Smartphone-enabled pulse rate variability: An alternative methodology for the collection of heart rate variability in psychophysiological research. *International Journal of Psychophysiology*, 89(3):297 – 304, November 2013. Psychophysiology in Australasia conference.

[283] Ramakrishna Mukkamala, Jin-Oh Hahn, Omer T Inan, Lalit K Mestha, Chang-Sei Kim, Hakan Töreyin, and Survi Kyal. Toward ubiquitous blood pressure monitoring via pulse transit time: theory and practice. *IEEE Transactions on Biomedical Engineering*, 62(8):1879–1901, 2015.

[284] Hakan Töreyin, Abdul Q Javaid, Hazar Ashouri, Oludotun Ode, and Omer T Inan. Towards ubiquitous blood pressure monitoring in an armband using pulse transit time. In *2015 IEEE Biomedical Circuits and Systems Conference (BioCAS)*, pages 1–4. IEEE, 2015.

[285] Edward Jay Wang, Junyi Zhu, Mohit Jain, Tien-Jui Lee, Elliot Saba, Lama Nachman, and Shwetak N Patel. Seismo: Blood pressure monitoring using built-in smartphone accelerometer and camera. In *Proceedings of the 2018 CHI Conference on Human Factors in Computing Systems*, page 425. ACM, 2018.

[286] Olli Lahdenoja, Mojtaba Jafari Tadi, Matti Kaisti, Timo Knuutila, Mikko Pänkäälä, and Tero Koivisto. Biomedical signal quality assessment via learning to rank with an application to mechanical heart signals. *Computing in Cardiology Conference (CinC)*, 44:1, 2017.

[287] Mojtaba Jafari Tadi, Jarmo Teuho, Eero Lehtonen, Antti Saraste, Mikko Pänkäälä, Tero Koivisto, and Mika Teräs. A novel dual gating approach using joint inertial sensors: implications for cardiac PET imaging. *Physics in Medicine & Biology*, 62(20):8080, 2017.

[288] Amy J Barton. The regulation of mobile health applications. *BMC Medicine*, 10(1):46, 2012.

Annales Universitatis Turkuensis

Turun yliopisto
University of Turku